THESIS

ELECTRIC FIELD BREAKDOWN PROPERTIES OF ION THRUSTER OPTICS

Submitted by

Rafael Anthony Martinez

Department of Mechanical Engineering

In partial fulfillment of the requirements

for the Degree of Master of Science

Colorado State University

Fort Collins, Colorado

Fall 2007

COLORADO STATE UNIVERSITY

October 30, 2007

WE HEREBY RECOMMEND THAT THE THESIS PREPARED UNDER OUR SUPERVISION BY RAFAEL A. MARTINEZ ENTITLED **ELECTRIC FIELD BREAKDOWN PROPERTIES OF ION THRUSTER OPTICS** BE ACCEPTED AS FULFILLING IN PART REQUIREMENTS FOR THE DEGREE OF MASTER OF SCIENCE

Committee on Graduate Work

John D. Williams - Advisor

Paul J. Wilbur

Raymond S. Robinson

Allan T. Kirkpatrick – Department Head

ABSTRACT

Measurements are presented of the electric field at breakdown for perforated flat plates fabricated from carbon-carbon (CC) composite, Poco graphite, pyrolytic graphite (PG), and molybdenum. The perforated flat plates represent electrodes used in ion sources and ion thrusters and measurements are made with and without ion beamlet extraction through the perforations. A ranking of the materials is presented of their suitability in ion source applications in terms of their electrical breakdown characteristics. For effective use in space missions, materials for ion optics systems must be capable of withstanding moderate electric field stress for long periods of time. In this regard, a simple analysis is presented where thrust density is shown to vary with the square of the electric field. This result suggests that a 50% increase in tolerable electric field will result in 125% higher thrust density and a thruster area reduction factor of 0.44 for a given power level. The reduction in thruster area would enable a commensurate decrease in thruster and gimbal specific mass. Experimental data are presented on field emission onset, electric field enhancement factor, and electrical breakdown properties of the materials listed above as a function of conditioning state, grid spacing, and charge transfer level per arc. Tests results are presented for both new electrodes and for electrodes that have been heavily sputtered to simulate wear expected during use.

Rafael A. Martinez
Dept. Mechanical Engineering
Colorado State University
Fort Collins, CO 80523
Fall 2007

ACKNOWLEDGEMENTS

My experience at CSU has been very rewarding and has helped me grow as an individual over the last two years. Coming to CSU for my master's degree was one of the best decisions I have ever made.

I offer a heartfelt thanks to my advisor, Dr. John Williams. I will always be appreciative of John for letting me join his research team and for his hands-on teaching style that as benefited me tremendously. John's willingness to share his enthusiasm and intellect has provided me with a great example of what a technical expert can be. I would also like to thank the other members of my committee for their guidance in preparing this thesis: Prof. Paul J. Wilbur and Prof. Raymond S. Robinson.

Special thanks to Dr. Dan Goebel from the NASA Jet Propulsion Laboratory who has assisted in guiding my research path. Mr. Dave Byers and Dr. Steve Snyder of NASA have also provided valuable feedback concerning my research. Thanks to Mr. Mark S. Buttweiler for assisting in the experimental setups described in this paper and Mr. Geoffrey N. Drummond from Colorado Power Electronics for loan of the arc suppression switch and for the high voltage power supply used for part of this study. I also want to acknowledge Casey Farnell, Cody Farnell, Russell Martin, Vijay Surla, Daisy Williams, and Kirk Zoerb who have made the time spent working at CSU a pleasure.

Finally, I thank my mom. She left this world long ago but her inspiring life has always pushed me to work hard and never give up when things get tough. Her love and belief in me has been a source of strength throughout my life.

Funding from the Jet Propulsion Laboratory, California Institute of Technology under a contract with the National Aeronautics and Space Administration is appreciated.

TABLE OF CONTENTS

LIST OF FIGURES

LIST OF TABLES

NOMENCLATURE

A_e = Effective emitting area

β_{FE} = Electric field enhancement factor

β_w = Weibull slope parameter

C = Capacitance

E = Applied Electric Field

E_m = Microscopic electric field acting at protrusion tip

f = Thrust Density

F = Thrust

g = Acceleration due to gravity

I_{sp} = Specific impulse

J = Ion current density

J_{FE} = Field emission current

ℓ_g = Grid gap spacing

m_dot = Propellant flow rate

m_+ = Mass of a propellant ion

η = Characteristic life

η_u = Propellant utilization efficiency

q = Elementary charge

Q = Total charge transferred in an arc

R = Net-to-total accelerating voltage

t = Time between arc events

U_e = Ion thruster beam ion velocity

V_N = Net accelerating voltage

V_T = Total accelerating voltage

Φ = Work function

1. INTRODUCTION

1.1 Electric Propulsion Overview

The focus of this work is on characterization of ion optics assemblies used in ion thrusters to uncover the limitations on thrust density, applied electric field, and other operational parameters. Ion thrusters belong to a larger family of propulsion technology that is collectively known as electric propulsion. Professor Robert Jahn defined electric propulsion in *Physics of Electric Propulsion*[1] as "the acceleration of gases for propulsion by electric heating and/or by electric and magnetic body forces." The promise of electric propulsion (EP) was first recognized by U.S. rocket pioneer Robert H. Goddard in 1906 who subsequently suggested several concepts to achieve this promise. His Russian counterpart, Konstantin Tsiolkovsky, proposed similar concepts in 1911, as did the German Hermann Oberth in his classic book on spacecraft in 1929. But the first systematic and tutorial assessment of EP systems is attributed to Ernst Stuhlinger, whose book *Ion Propulsion for Space Flight* summarizes his seminal studies of the 1950s[2].

Whereas combustion is limited by the energy stored within the chemical bonds of the propellant, electric propulsion is limited only by the on-board power available to the thruster. This is the main advantage of electric over chemical propulsion, since the amount of energy that can be externally applied is limited only by available technology. In a chemical rocket, the dependence on internal chemical energy limits the maximum specific impulse to below 450 s, whereas in electric rockets, specific impulses of over 17,000 s have been obtained in the laboratory[3,4]. Because of its higher specific impulse, an electric propulsion system with adequate on-board power can perform the same equivalent orbital maneuver as a chemical system while using less propellant. This ability

can make an electric propulsion system very attractive for orbital insertion and orbit maintenance of reconnaissance and communications satellites for a number of reasons with the proviso that the on-board power system, the thruster, and propellant handling systems required for the electric propulsion capability are not a significant fraction of the propellant mass. By reducing the amount of propellant needed to perform a given maneuver, a spacecraft mission planner can increase the number or duration of maneuvers – or conversely the lifetime of the spacecraft or satellite can be increased– with the same overall propellant mass. Alternatively, the propellant mass can be decreased to maintain the same spacecraft maneuvering lifetime, allowing additional payload hardware to be added while maintaining the same overall spacecraft mass. Of course any combination of these two options is also possible. A third option is to decrease the total overall mass of the satellite in order to launch the spacecraft using a smaller (and less expensive) launch vehicle.

This thesis will focus on ion thrusters but the reader is referred to Refs. 1, 2, 5, 6, and 7 for descriptions of other types of thrusters and development efforts related to the electric propulsion systems.

1.2 Ion Thruster Operation

Within an ion thruster discharge chamber (see Fig. 1.1), electrons are supplied by a hollow cathode, called the discharge cathode, typically located at the center of the thruster at its upstream end. The electrons are supplied along with propellant atoms that are fed through (1) the discharge cathode and (2) a propellant plenum. Electrons are accelerated from the discharge cathode through the application of the discharge power supply that is used to bias the discharge chamber wall positive of the cathode. The

product of the electron emission current and the discharge voltage represents the discharge power that is used to ionize propellant supplied to the discharge chamber.

The components needed to generate thrust in a typical ion thruster, which are shown in Figure 1.1 include 1) a discharge chamber, 2) a filament or hollow cathode, 3) an anode, 4) screen and accelerator grids, and 5) a neutralizer.

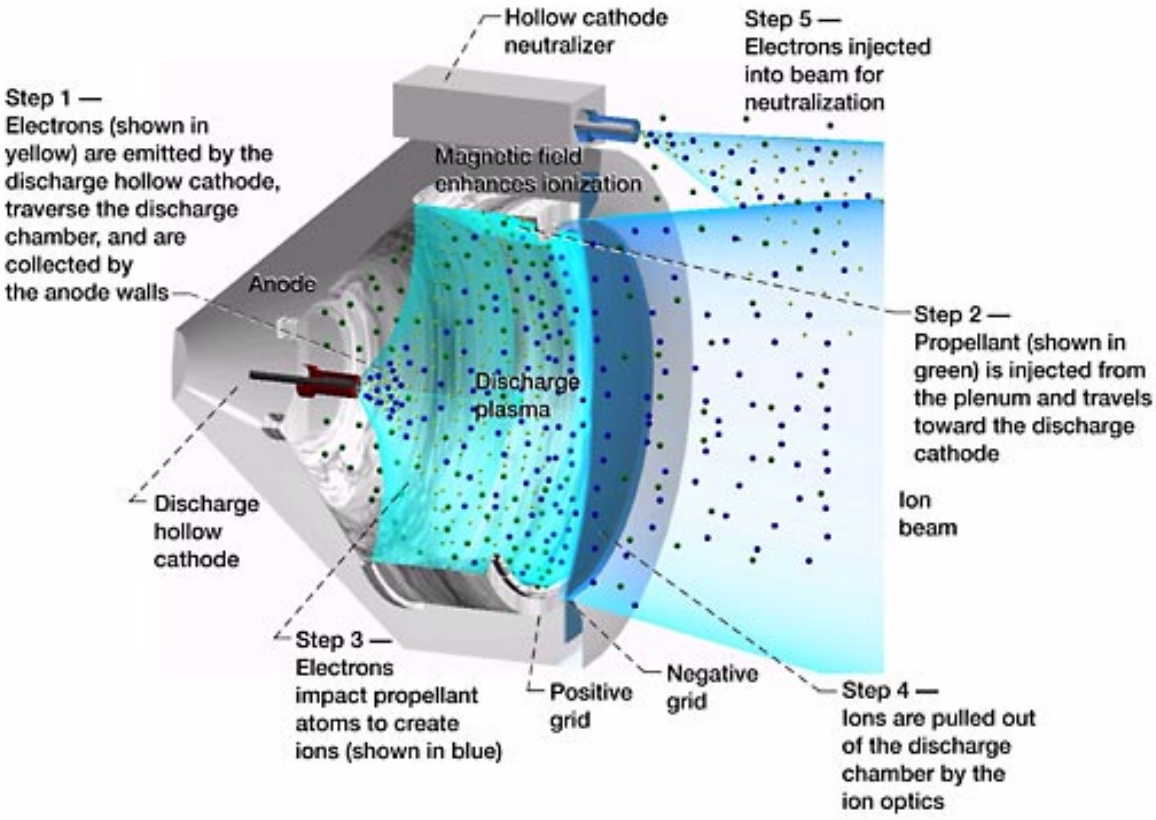

Figure 1.1 **Ion Thruster operation: Step 1--Electrons (shown as small, pale green spheres) are emitted by the discharge hollow cathode and are accelerated into the discharge chamber where they are eventually collected by the anode walls. Step 2--Propellant atoms (shown in green and injected through the cathode and plenum) are impacted by electrons where some are transformed into ions (shown in blue). Step 4--Ions are extracted from the discharge chamber by the ion optics. Step 5--Electrons that were stripped from the propellant atoms within the discharge chamber and collected on the anode are pumped though a power supply (used to bias positive the discharge chamber) and injected into the ion beam for neutralization. Image Credit: NASA Glenn Research Center.**

In some cases, when a high-energy electron (negative charge) from the discharge cathode strikes a propellant atom (neutral charge), a second electron is released, yielding two negative electrons and one positively charged ion. A collective action of these events leads to the creation of a moderately dense (10^{10} to 10^{11} cm^{-3}) plasma within the discharge chamber. High-strength magnets are placed along the discharge chamber walls so that as electrons approach the walls, they are redirected into the discharge chamber by the magnetic fields created with the magnets. One increases the chance that atoms will become ionized by maximizing the length of time that energetic electrons and propellant atoms remain in the discharge chamber. Propellant utilization within an ion thruster is typically greater than 90% for modern devices.

In a gridded ion thruster, ions are accelerated by electrostatic forces (i.e. electric fields). The electric field is generated by biasing two electrodes, called grids, relative to one another. The grids are insulated from one another and supported in an ion optics assembly. This assembly is attached to the downstream end of the discharge chamber. The greater the voltage difference between the two grids, the faster the positive ions move as they pass the negative charged grid. Each grid has thousands of coaxial apertures (or tiny holes). The two grids are spaced close together and the aperture centerlines are aligned from one grid to the other. Each set of apertures (opposing holes) acts like a lens to focus ions through the optics system.

Ion thrusters commonly use a two-electrode system, where the upstream electrode (called the screen grid) is charged highly positive along with the discharge chamber plasma, and the downstream electrode (called the accelerator grid) is charged highly negative. Ions generated in the discharge plasma that flow to the region nearby the screen

grid are attracted toward the accelerator grid and are focused out of the discharge chamber through the apertures, creating thousands of ion jets or beamlets. The stream of all the ion beamlets together is called the ion beam. The thrust created by the ion beam is proportional to the product of the beam current and the velocity of the beam ions once they fall through the potential difference between the discharge plasma and the ion beam plasma formed downstream of the grids. The velocity of the ions in the beam plasma is determined by the voltage applied between the two regions, and this voltage can be changed to either increase or decrease the ion exhaust velocity. Whereas the exhaust velocity of a chemical rocket is limited by the internal energy of the chemically reacting propellant and the heat-handling capability of the rocket nozzle, the effective exhaust velocity of an ion thruster is limited by the voltage that is applied to the ion optics, which is theoretically unlimited. In actuality, the voltage is limited by several mission-related considerations and physical factors, one of which is the maximum operating electric field in the region between the grids - one focus of this thesis.

1.3 Purpose of Study

The successful demonstration of the NASA Solar Electric Propulsion Technology Applications Readiness (NSTAR) ion engine on NASA's Deep Space 1 spacecraft and the Extended Life Test (ELT) of the NSTAR flight spare[8] has spurred interest in ion propulsion for more demanding missions requiring ΔVs ranging from 40 km/s to over 100 km/s. The most demanding missions would require power levels of 20 kW to 50 kW per thruster, specific impulses of 6000-9000 seconds, and operational lifetimes as high as 10 years.[9] The Nuclear Electric Xenon Ion System (NEXIS) ion thruster[10] was recently developed by a Jet Propulsion Laboratory-led team while the High-power Electric

Propulsion (HiPEP) thruster[11] was developed by a separate effort led by NASA Glenn Research Center personnel to meet these more ambitious missions. Carbon-based (pyrolytic graphite and carbon-carbon) grid materials are being investigated for increased thruster lifetime because these materials are more resistant to sputter erosion than molybdenum, which has been used on the majority of ion thrusters to date. In this regard, it is noted that the service life of the NSTAR ion thruster at full power was limited by erosion of the molybdenum accelerator grid[12]. The successful development of carbon-based ion optics could potentially eliminate accelerator grid erosion as the primary life-limiting concern of ion thrusters. It is important to note that carbon-based grids have been tested on thrusters that normally use molybdenum grids and similar performance has been obtained.[13, 14]

A major limitation to increasing the performance of an ion thruster is the maximum permissible electric field in the intra-grid region. Present high specific impulse ion thruster designs utilize relatively low electric fields (~2 kV/mm), which limit the maximum obtainable thrust density and require larger-than-desired thrusters to be built to handle a given amount of power and propellant.

The following simplified analysis shows how thrust density is related to intra-grid electric field strength. First the velocity of a thrust producing ion is related to the specific impulse and the propellant utilization factor by the following expression:

$$U_e = \frac{I_{sp} g}{\eta_u} \tag{1.1}$$

The net accelerating voltage is

$$V_N = \frac{m_+ U_e^{\,2}}{2q} = \frac{m_+}{2q}\left[\frac{I_{sp} g}{\eta_u}\right]^2 \quad . \tag{1.2}$$

Next, the total accelerating voltage (V_T) can be defined as:

$$V_T = \frac{V_N}{R} \quad . \tag{1.3}$$

By specifying the electric field, one can calculate the grid spacing to be

$$\ell_g = \frac{V_T}{E} = \frac{V_N}{ER} \tag{1.4}$$

The beam current per unit area can be related to the grid spacing and the total voltage using the following form of the Child-Langmuir equation for space-charge limited current flow:

$$j = \frac{4\varepsilon_o}{9}\left(\frac{2q}{m_+}\right)^2 \frac{{V_T}^{3/2}}{{\ell_g}^2} = \frac{4\varepsilon_o}{9}\left(\frac{2q}{m_+}\right)^{1/2} \frac{E^{3/2}}{{\ell_g}^{1/2}} \quad . \tag{1.5}$$

Although we recognize the three-dimensional effects of the geometry on the assumed 1-D behavior modeled in Eq. (1.5) may be important, this assumption allows us to proceed in a relatively straightforward way toward an approximate expression for thrust density:

$$f = \frac{\dot{m}\eta_u U_e}{A} = \frac{jm_+}{q} I_{sp} g \quad . \tag{1.6}$$

Combining Eqs. (1.2) and (1.4) gives

$$\ell_g = \frac{m_+}{2qER}\left[\frac{I_{sp} g}{\eta_u}\right]^2 \quad . \tag{1.7}$$

Equation (1.7) shows a direct dependence on m_+/q and I_{sp}^2 and an inverse dependence on the electric field, E. When Eqs. (1.5) and (1.7) are substituted into Eq. (1.6), one obtains an expression showing how the thrust density is related to the applied electric field between the grids:

$$f \approx \frac{\frac{4\varepsilon_o}{9}\left(\frac{2q}{m_+}\right)^2 E^{3/2}\frac{m_+}{q} I_{sp} g}{\left[\frac{m_+}{2qER}\right]^{1/2}\left[\frac{I_{sp} g}{\eta_u}\right]} = \frac{8\varepsilon_o}{9} E^2 \eta_u \sqrt{R} \tag{1.8}$$

From Eq. (1.8), one can see that thrust density is directly dependent on the square of the applied electric field (E), and one can conclude that as the applied electric field between the grids of an ion thruster is doubled the thrust density will quadruple. This result suggest that a 50% increase in electric field will result in a 125% higher thrust density and a thruster area reduction factor of 0.44. The reduction in thruster area would enable a similar reduction in thruster and gimbal specific mass. In general, maximizing the electric field between the electrodes results in higher perveance which can lead to smaller and lighter thrusters.

One concern identified by developers of the high performance NEXIS ion thruster is the long term ability of an ion optics system comprised of advanced carbon-based material to withstand applied voltages of ~5.5 kV and applied electric fields of ~2.3 kV/mm in an environment where the negatively biased accelerator grid is being bombarded and slowly eroded by a low current density of moderately energetic ions. Damage from an arc can include both melting and vaporization on some surfaces in combination with severe erosion of material due to intense plasma formation and subsequent energetic ion bombardment. Both forms of damage can become problematic if they cause the accelerator grid surface to become progressively more susceptible to the initiation of follow-on arcs. Surface damage increases with the charge transferred in an arc, and values above 5 mC can cause damage to both screen and accelerator surfaces comprised of carbon-based materials.[15] As an example of the severity of the problem, a

recent endurance test of an ion thruster with 14-cm carbon-carbon grids was terminated because of excessive arcing between the grids.[16]

To determine what will happen to electric field breakdown behavior early in life and later on during a mission, accelerated wear tests were conducted and will be described in this thesis. Briefly, selected areas of accelerator gridlets were sputtered with an ion beam in a SPECTOR™ Ion Beam Etching and Deposition system. This was done to "age" the gridlet in a way that simulates how wear occurs on the accelerator grid of an actual ion thruster. The highest electric fields on a negatively biased surface occur on the upstream face of the accelerator grid nearby the entrance to apertures, and so the "aging" process was performed using masks that limited wear to these regions where arcing was most likely to occur. Specifically, the accelerator gridlet was mounted beneath a mask on a fixture that was tilted and rotated relative to an energetic ion beam. The erosion caused during sputter processing was performed at rates that are hundreds of times faster than erosion rates expected during thruster operation in space on some surfaces. Although not identical to the wear that occurs during actual use in space, the accelerated-erosion processing results in a sputtered surface texture that is representative of an actual sputter-eroded accelerator grid. After fixed periods of aging, the gridlets were remounted in the gridlet test fixture, and the arcing characteristics were re-measured under ion beam extraction conditions. The aging and arcing characterization tests were repeated a number of times on different gridlets to determine how erosion processes would affect long-term ion thruster operation at high specific impulse conditions. In order to avoid unintentional arc damage, the electric-field breakdown tests were performed using

advanced arc suppression power supplies and high-speed switches that were provided by Colorado Power Electronics, Inc.[17]

This thesis is organized by first describing the experimental systems used for the gridlet tests and accelerated wear processing (along with gridlet evaluation techniques) in Chapter 2. Chapter 3 presents the experimental results. Conclusions and recommendations for future work are provided in Chapters 4 and 5.

2. EXPERIMENTAL APPARATUS AND PROCEDURES

The present investigation was undertaken in an attempt to provide a more complete understanding of the phenomena that limit the ion extraction capabilities of two-grid accelerator systems. Both experimental and theoretical techniques are used to analyze the limitations of high specific impulse ion optics. Direct impingement of high velocity ions, which causes sputter erosion of the accelerator grid, limits the extractable ion current for a particular grid geometry and set of operating voltages. Electron backstreaming, a second limitation to the operating range of the system, represents a power loss mechanism for the thruster. Field emission and Weibull statistical analysis are used to characterize electrical breakdown – a third phenomena that limits the operating range of the accelerator system through the region between the grids. The large electron currents that can flow between the grids during electric field breakdown can lead to destruction of the ion optics. A review of related research work, along with the implementation of field emission and Weibull analysis, is used to provide a more complete understanding of the origin and characterization of electric field breakdown phenomena.

2.1 Gridlet Testing Facility

Photographs of the gridlet test facility, the gridlet mounting assembly, and an operating ion source are shown in Figures 2.1-2.3. A sketch of the gridlet geometry is shown in Fig. 2.4. Table 2.1 contains a list of NEXIS ion optics geometrical parameters that corresponds to the sketch of Fig. 2.4.

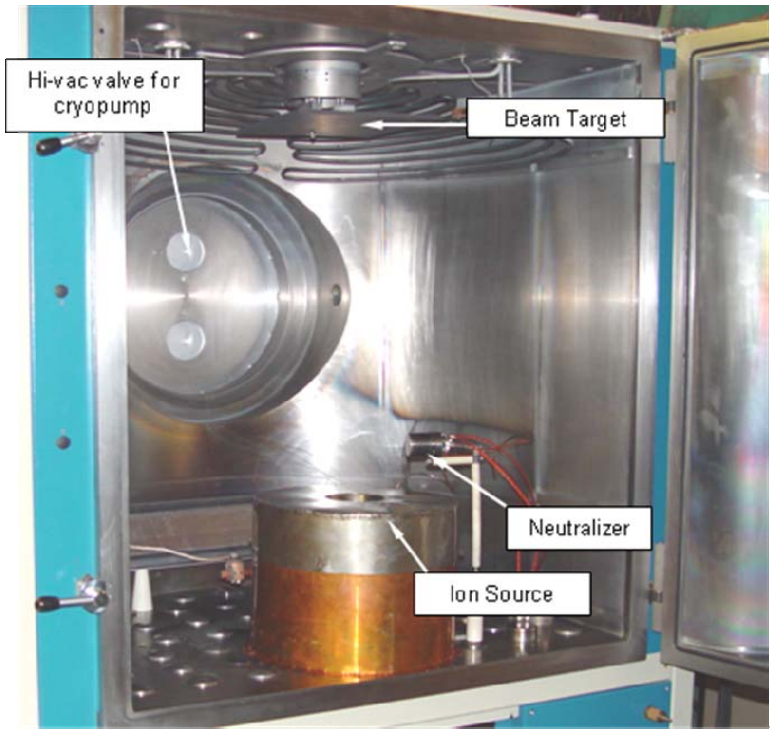

Figure 2.1 High voltage sub-scale ion optics testing facility.

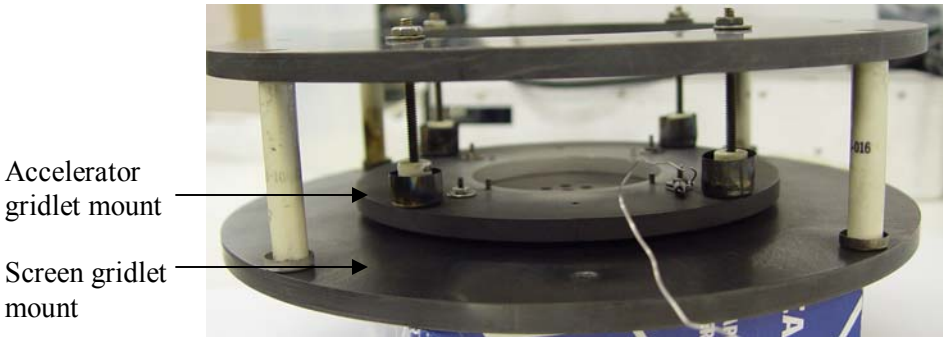

Figure 2.2 Mounting structure for gridlets.

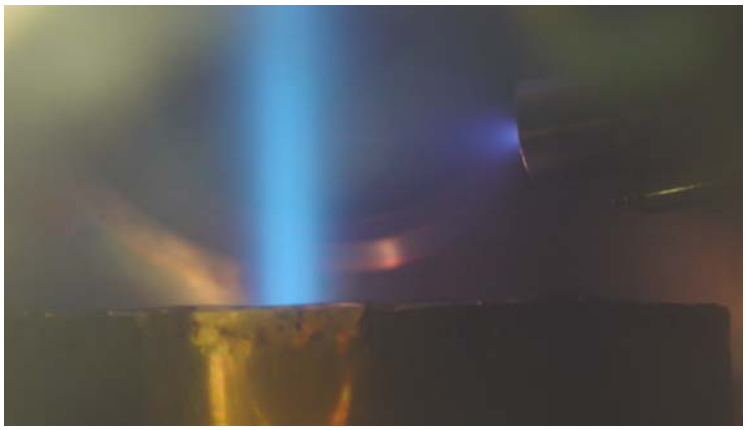

Figure 2.3 Gridlet ion source in operation at V_T = 8kV.

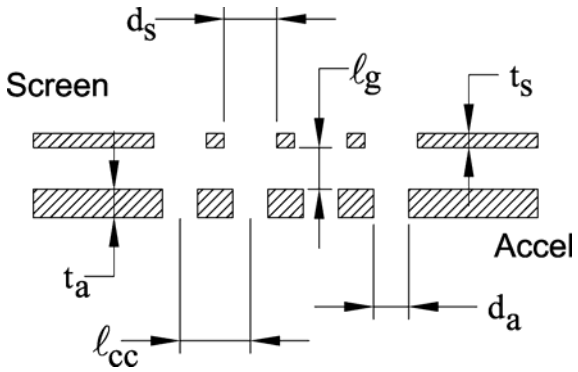

Figure 2.4 Gridlet geometry definitions. (See Table 2.1 for more information.)

Table 2.1 NEXIS geometry and nomenclature specific to the present study.

Parameter	Description	Dimension*
d_s	Screen hole diameter	3.600
t_s	Screen grid thickness	3.601
d_a	Accel hole diameter	3.543
t_a	Accel grid thickness	4.850
ℓ_g	Grid-to-grid gap^	3.575
ℓ_{cc}	Center to Center spacing#	3.620

* Dimensions are relative to NSTAR thruster optics
^ Varied in this study
# Hexagonal hole pattern

The gridlet characterization test facility (shown in Fig. 2.1 with the ground screen installed over the ion source) has a volume of 0.65 m^3 and a base pressure in the mid

10^{-7} Torr range. When the ion source is running at a xenon flow rate of 0.5 sccm, the pressure is 1.2×10^{-5} Torr. The facility is equipped with a cryopump to eliminate the concern of an oil-based pumping system that may interfere with arcing experiments (as discussed in section 2.8). The gridlets are ~70 cm away from a graphite target attached to the top of the chamber. The size of the target was chosen based upon ffx simulations,[18] which predict a maximum beam divergence angle of less than 20 degrees for most operating conditions.

Figure 2.5 shows photographs of a carbon-carbon screen and accelerator gridlet set prior to testing. Gridlets were also fabricated from pyrolytic graphite, molybdenum, and Poco graphite. The dimensions and geometry of the gridlets were identical for all the materials tested (see Table 2.1). These gridlets have the same dimensions and geometry as the Nuclear Electric Xenon Ion System (NEXIS) ion thruster full-scale grids (57 cm active beam diameter) developed by the Jet Propulsion Laboratory.[10]

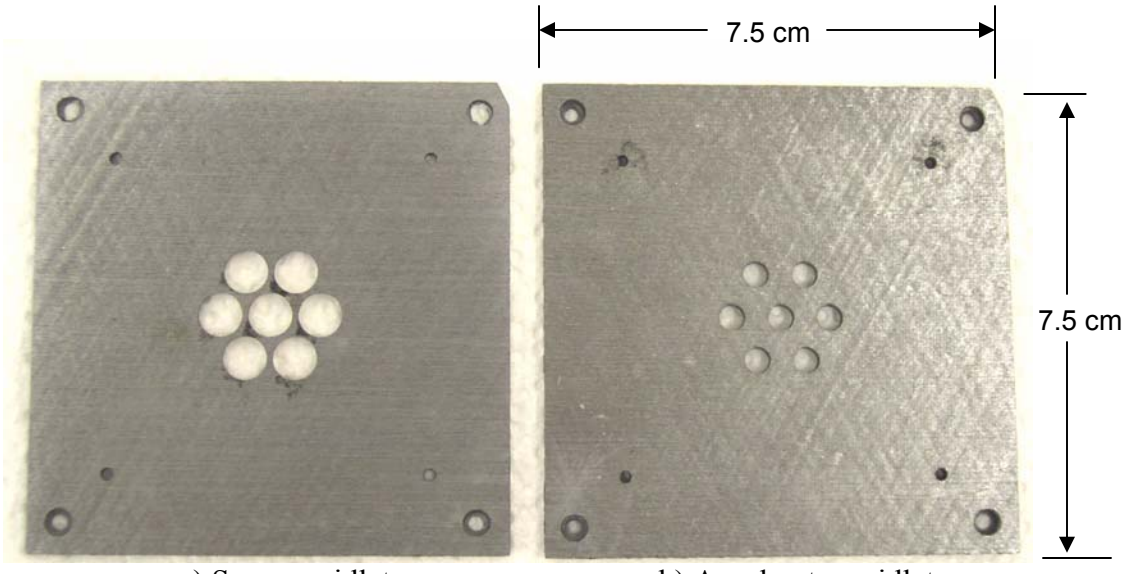

a) Screen gridlet b) Accelerator gridlet

Figure 2.5 NEXIS-style carbon-carbon gridlets prior to testing.

The molybdenum gridlet material had apertures drilled using a CNC machine, followed by careful burr removal, rounding of the gridlet edges and corners, and grit blasting to provide a surface texture similar to the material used in actual flight thrusters. The Poco graphite gridlet apertures were also drilled using a CNC machine followed by light sanding with fine (600 grit) sand paper. After drilling the holes into the surface, the edges and corners around the perimeter of the part were also rounded. No other cleaning or surface preparation (other than blowing air over the surface to remove loose debris) was conducted. The carbon-carbon composite material was fabricated, CVD infiltrated, and coated by AllComp (see Beatty[19] for more details) to fill any voids and smooth the surface. Unlike the other materials, the apertures in the CC plates were laser drilled. Following this, the soot and debris generated from the laser drilling process was cleaned away using acetone and lint-free wipes. Detailed descriptions and photos of each gridlet material are included in Chapter 3.

Tests were conducted by mounting an assembly comprised of two gridlet electrodes (shown in Figure 2.2) to a ring-cusp discharge chamber. The screen and accelerator gridlets were insulated from one another using standoff insulators and were aligned through the use of pins that were passed through precision-placed holes. The inner diameter of the discharge chamber was much larger than the active diameter of the gridlets to ensure that the discharge chamber plasma properties would be uniform over the entire gridlet ion extraction area, and thereby impose common behavior in all beamlets. The uniform discharge plasma condition allowed division of the measured beam current by the number of apertures to obtain the current per hole or beamlet current. A ground screen was placed between most of the inactive area of the accelerator grid and

the beam plasma to limit the collection of beam plasma ions on the inactive regions of the accelerator gridlet surface. This allowed the impingement current collected by the accelerator grid to be converted to a per aperture value by dividing the ammeter reading by the number of active accelerator grid apertures.

2.2 Current Impingement Limitations

One important goal of gridlet testing is to measure the operational limitations of large diameter, high specific impulse ion thrusters and identify constraints on throttling range and plasma uniformity. The data are also useful for the validation of numerical models of high specific impulse ion optics systems.

Figure 2.6 depicts a portion of a multi-aperture two-grid ion accelerator system showing the coaxial aperture geometry and ion beamlet formation with the variation in electrical potential associated with the grid geometry and when typical voltages are applied. As shown in Figure 2.6, the discharge chamber is at a potential of a few tens of volts positive of the screen grid, which is itself at a high positive potential of several hundred to several thousand volts. The purpose of the screen grid is to (1) prevent direct access of the accelerated ions to the accelerator grid webbing, (2) provide a boundary for a sheath to attach, and (3) direct ions so they are properly extracted into well-formed beamlets. It is the accelerator grid, with its negative potential, that actually accelerates the ions from the discharge plasma. The discharge chamber plasma potential is near anode potential, and the potential drop across the screen hole plasma sheath is approximately equal to the discharge voltage (V_D). The net accelerating voltage used herein, consequently, is defined as the sum of the discharge voltage, which was set to 30 V, and the screen voltage

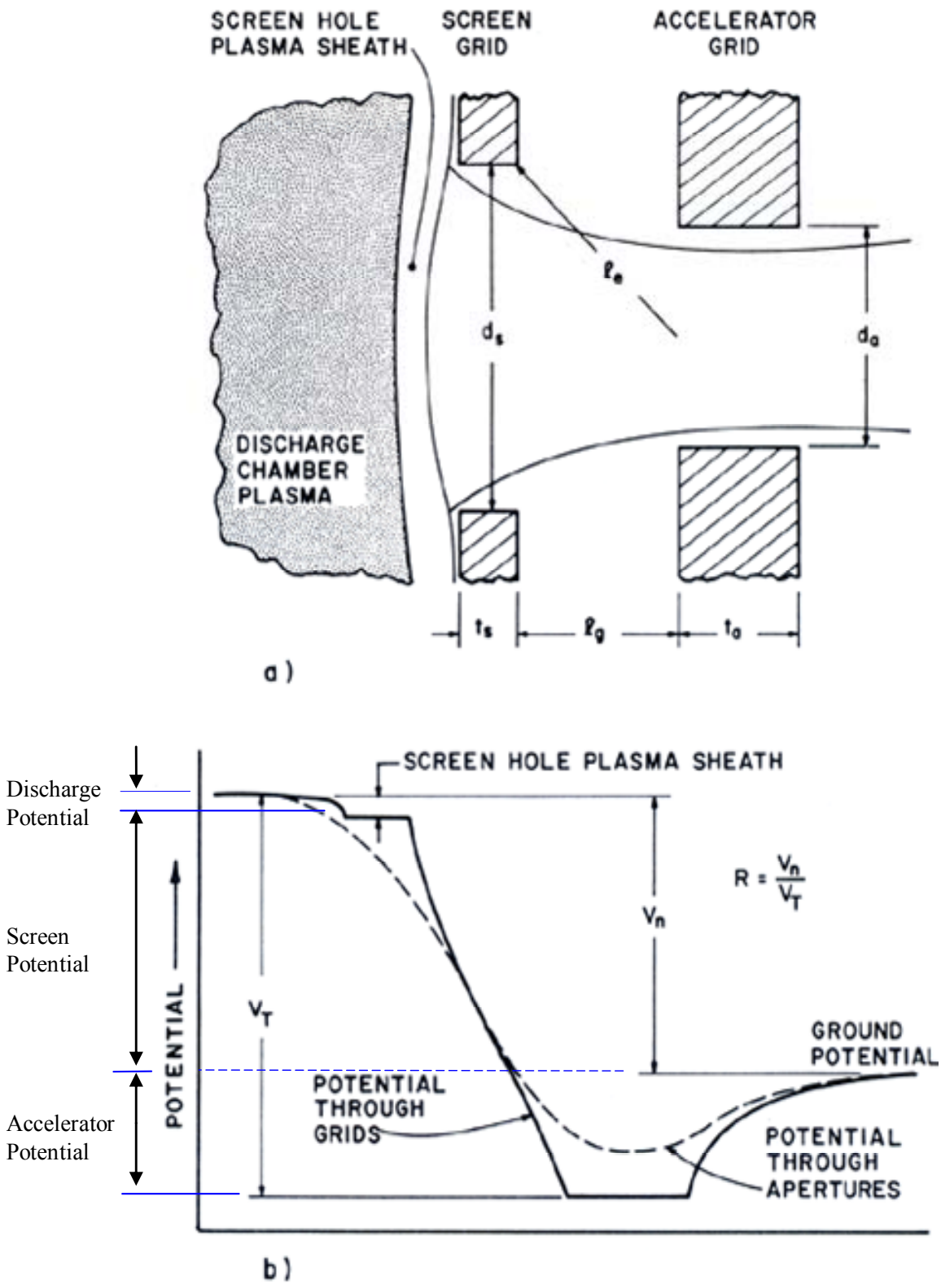

Figure 2.6 **Sketch of a beamlet being formed in a two-grid ion acceleration system (a) along with an idealized plot of the potential variation through the centerline of the ion accelerator system (b). (From Ref. 20)**

$$V_N = V_D + V_S \tag{2.1}$$

The total accelerating voltage applied to the accelerator system is defined as the sum of this net accelerating voltage and the absolute value of the accelerator grid potential,

$$V_T = V_N + |V_A| \tag{2.2}$$

or

$$V_T = V_D + V_S + |V_A| . \tag{2.3}$$

Finally, the ratio of the net accelerating voltage to the total accelerating voltage (R) is defined as

$$R = \frac{V_N}{V_T} \tag{2.4}$$

In normal operation, a concave shaped sheath, shown at the entrance to the screen hole in Figure 2.6, is observed. As the plasma density, and, consequently, the ion flux to the sheath increases, the sheath moves closer to the hole and begins to flatten out. Eventually, an operating point is reached where the sheath is sufficiently flat or even slightly convex so that ions directed toward the accelerator grid are no longer focused properly and they begin to impinge directly upon the accelerator grid apertures. The direct impingement by these high velocity ions causes sputter erosion of the accelerator grid and this process can result in rapid destruction of the accelerator grid. The onset of direct ion impingement due to under focusing thus limits the maximum extractable ion current for a particular grid geometry at a given operating voltage.

The uniform discharge plasma condition in our discharge chamber (as described earlier) allowed division of the measured beam current (J_B) by the number of apertures to obtain the per hole or beamlet current (J_b). In addition, the impingement current collected

by the accelerator grid (J_A) was converted to a beamlet value (J_a) by dividing the ammeter reading by the number of active accelerator grid apertures.

Perveance

One goal of gridlet testing is to determine the range of beamlet currents (ion current per hole) where an ion optics system can be safely operated. Limits on the beamlet current occur at both low and high values where over and under focusing processes occur that drive energetic beam ions directly into the accelerator grid. These current limitations can manifest themselves during initial testing of a grid set or after many tens of thousands of hours of operation during a particular mission or acceptance/qualification test sequence. This is especially true when thrusters with wide variations in beam flatness uniformity are tested or when wide throttling ranges are evaluated. To avoid unintentional damage to hardware, the ion optics characteristics of any proposed ion acceleration system must be carefully determined before a device is placed under test at a given operating condition. These limitations can easily be characterized using a gridlet by watching for a sudden increase in the impingement current flowing to the accel grid as the beamlet current is varied.

As shown in Fig. 2.7, when the beamlet current is low, the sheath that separates the discharge chamber plasma from the ion acceleration region is dished upstream to the point where ions are over-focused, their trajectories cross, and, at the limit, ions in the beamlet begin to impinge directly on the downstream edge of an accelerator grid aperture. A low beamlet current condition can occur at the edge of an ion optics system or over the entire optics system of a thruster that is operated at a low throttle condition (i.e., at high beam voltage and low beam current), and this limiting beamlet current

condition is referred to herein as the crossover limit. In contrast, the perveance limit is used to describe the condition where the beamlet current is high and the ions are under-focused to the point where they begin to impinge directly on the upstream side of the accelerator grid.

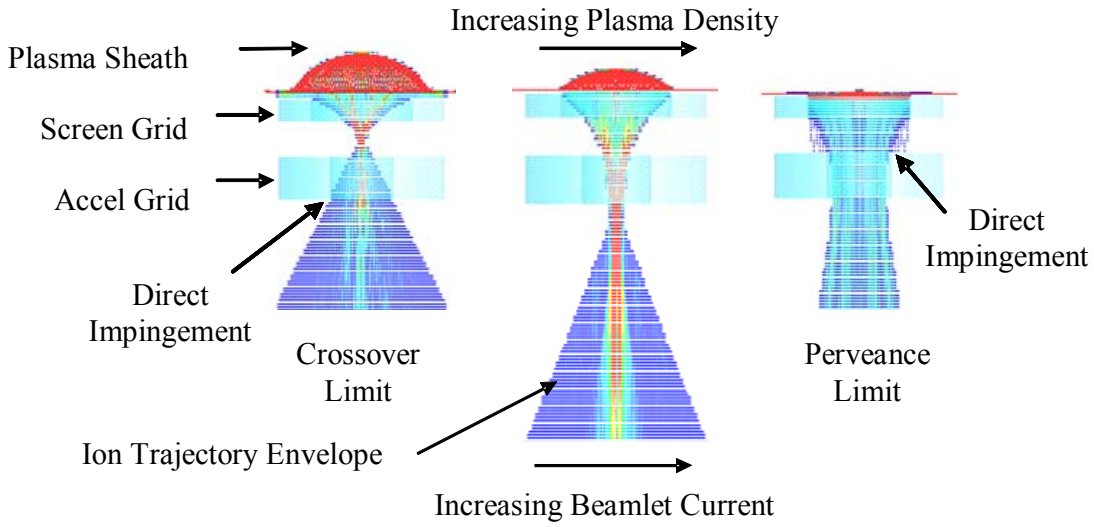

Figure 2.7 Numerical simulation results demonstrating perveance and crossover current limitations.

Typical data from accel grid impingement current measurements display a "U" shape when plotted as a ratio of impingement-to-beamlet current versus beamlet current as shown in Fig. 2.8. Note that the beamlet current was varied in this experiment by varying the discharge current while holding the discharge, beam, and accel voltages constant. At low beamlet currents, the relative impingement current rose due to crossover ion impingement on the downstream edge of the accel hole barrels. At moderate beamlet currents, the relative impingement current is flat and at a value dependent upon the background neutral density and the propellant utilization efficiency of the ion source. In our small vacuum facility operating at low propellant utilization, the baseline impingement current typically lies between 1% and 5% of the beam current. As the

beamlet current is increased to higher values, the relative impingement current again rose quickly indicating that direct ion interception was occurring on the upstream edge of the accel hole barrels due to perveance (or space-charge) limitations. Figure 2.8 indicates that the safe operating range of the NEXIS gridlets was relatively large at 6.05 kV of total accelerating voltage (V_T) and the ratio of perveance to crossover beamlet currents was ~7:1.

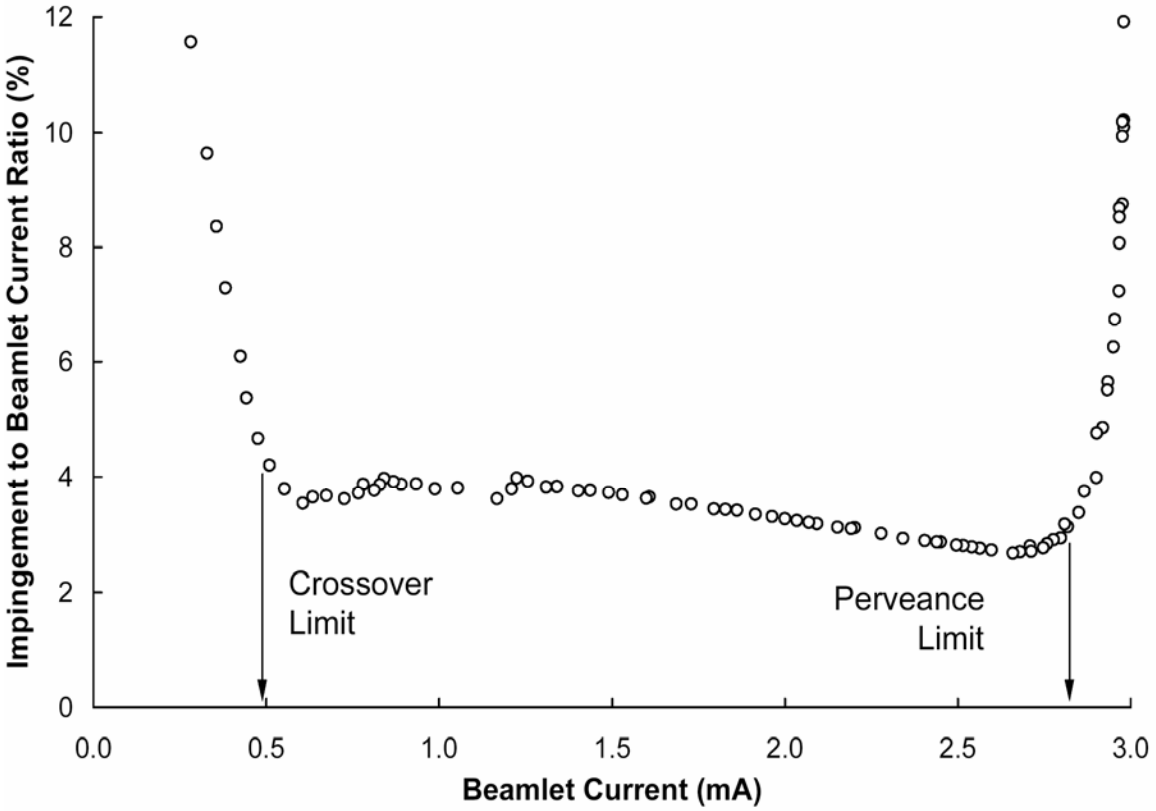

Figure 2.8 Typical impingement data collected at V_T= 6.05 kV.

One consequence of direct impingement concerns high rates of material being sputtered from the accelerator grid that may re-deposit onto the downstream surface and within the aperture barrel regions of the screen grid. The deposited film on the screen grid can build up to the point where it may crack, de-laminate, and peel from the screen grid

sooner than if only charge exchange ion impingement was occurring on the accelerator grid. If a flake of the deposited film protrudes onto a screen hole, the ion acceleration processes near the screen electrode will be strongly affected and additional ions may be directed into and erode the accelerator grid.[21] In addition to formation of rouge holes, flakes that span the gap between the accelerator and screen grids can cause recycles to occur, and, if the flakes are large in cross-sectional area, they may require excessive use of grid clearing circuitry. Debris transferred from the screen to the accelerator electrode can also initiate arcs from the accelerator. Finally, it is pointed out that excessive direct impingement on the accel grid could cause structural failure of the electrode.

The maximum current density capability of a grid set can be quantified using the Child-Langmuir law[22] as shown in Eq. (2.5)

$$J_{b,pl} = \frac{4\varepsilon_o}{9}\sqrt{\frac{2q}{m}}\frac{V_T^{3/2}}{\ell^2} \tag{2.5}$$

In Eq. (2.5), ε_o represents the permittivity of free space, q the charge on a singly ionized ion, m the mass of a xenon ion, and ℓ the length through which the ions are accelerated by the potential difference applied between the surfaces (V_T). This equation describes the one-dimensional space charge limited current density, which can be drawn between two flat, parallel surfaces. Applying Child's law to the three-dimensional geometry of the accelerator system requires an assumption concerning the acceleration length ℓ. In past investigations[22,23] the acceleration length used to correlate the performance of various grid geometries that are not truly one-dimensional is the effective acceleration length ℓ_e. The effective ion acceleration length, ℓ_e, was calculated using the following equation

$$\ell_e = \sqrt{(t_s + \ell_g)^2 + \frac{d_s^2}{4}} \tag{2.6}$$

In Eq. (2.6), t_s represents the screen grid thickness and the other parameters are described above, in Table 2.1, and in Figure 2.4. Substituting this effective acceleration length into the one-dimensional Child's law, Eq. (2.5) can be rewritten as

$$J_{b,pl} = \frac{\pi\varepsilon_o}{9}\sqrt{\frac{2q}{m}}\, V_T^{3/2}\, \frac{d_s^2}{\ell_e^2} \quad . \tag{2.7}$$

In Eq. (2.7), $J_{b,pl}$ represents the beamlet current at the perveance limit.

The perveance ($\alpha\ J_b/V_T^{3/2}$) level at which impingement occurs at either limit is determined by the electrode aperture geometry, the discharge plasma density, and the electrode spacing.

2.3 Electron Backstreaming

A third and equally important operational limit on ion optics systems is the back-streaming limit, which is the voltage that must be applied to the accelerator grid to prevent beam plasma electrons from backstreaming. Ideally, the accelerator grid voltage should be held negative but as close to this limit as possible. This will ensure that damage due to the small current of charge exchange ions that sputter erode and limit the lifetime of the accelerator grid will be minimized. Unfortunately, the backstreaming limit can change as the accelerator grid wears over time or when the beam current is changed, and compromises on selecting the magnitude of the accelerator voltage must be made. Many factors can affect the backstreaming voltage including aperture geometry, net voltage, beamlet current, and the plasma flow field environment in the ion beam.[24] The onset of backstreaming can also be strongly affected by the operational conditions associated with the neutralizer and conductive plasma-bridge that forms between the

neutralizer plasma and the beam plasma.[25] During a mission, the accelerator grid can erode to the point where the voltage limit of the accelerator power supply is no longer adequate to stop electrons from backstreaming. This condition defines the end-of-life (EOL) for the thruster/power-supply system. The magnitude of the negative voltage that must be applied to the accelerator grid to prevent electron backstreaming, the backstreaming limit, was measured by (1) setting the accelerator voltage magnitude to a value where no backstreaming occurs, (2) slowly decreasing the accelerator voltage magnitude and simultaneously monitoring the beam current, and (3) reducing the beam current/accelerator voltage data to determine the voltage where the beam current increases to a value 2% above its baseline value due to backstreaming electron flow. Figure 2.9 presents a plot of apparent beamlet current as the accelerator voltage magnitude was varied from 600 V to 200 V when the beamlet current (due to ion flow) was fixed at 3 mA at an accelerator grid bias of -600 V. The increase in apparent beamlet current at 350 V is due to beam plasma electrons that backstream through the grids and deposit their energy into the ion source discharge chamber. Voltage magnitudes larger than this limit must be applied to the accelerator grid to avoid excessive electron backstreaming and potentially harmful heat deposition within the discharge chamber.

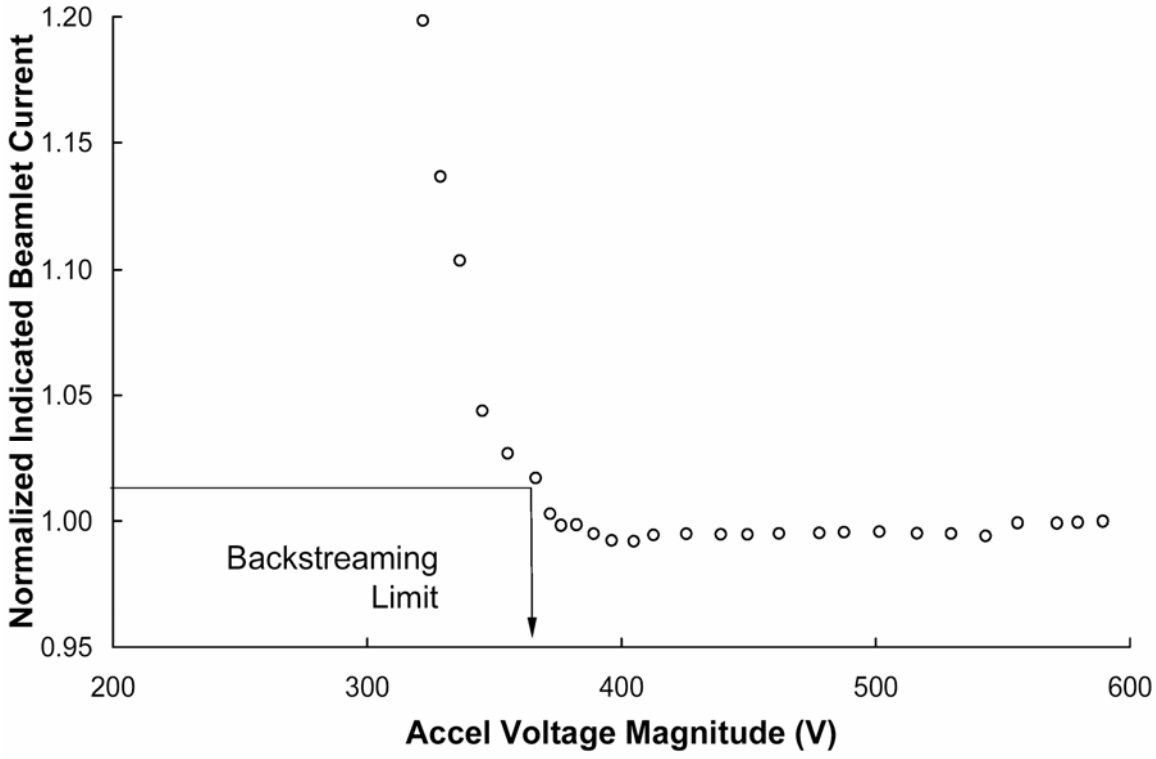

Figure 2.9 Typical beamlet current versus accelerator voltage plot used to determine the backstreaming limit.

The black dotted line of Fig. 2.6b shows the potential variation along the centerlines of grid aperture pairs that are operating normally. As the negative potential on the accelerator grid is reduced, however, the potentials through the accelerator grid become less and less negative until eventually a condition is reached where the potentials at all points along the centerline become positive (i.e., above the ground potential). When this occurs beam plasma electrons are able to enter the gap between the high voltage screen and accelerator grid, and they are then accelerated by the beam power supply to energies equivalent to the net voltage. When large numbers of electrons begin to backstream, an energetic electron beam will form that can damage not only the ion source discharge cathode assembly, but also any of the discharge surfaces upstream of the ion

acceleration optics that the electrons happen to impact. Generally speaking, electron backstreaming is prevented by operating the accelerator grid at a sufficiently negative voltage to ensure that the central region of the accel aperture are negative of the beam plasma by several to many volts. This condition will provide the necessary margin to prevent significant backstreaming potential in the accelerator aperture. Operation at a very negative accelerator grid voltage (required to provide margin in some grid designs), however, enhances charge-exchange ion erosion. In this respect, the required presence of the negative voltage region near the accelerator grid aperture to prevent electron backstreaming, actually enhances another problem – erosion of the accelerator grid.

2.4 Accelerated Erosion Techniques

An ion beam facility, previously described in Martinez *et al.*[26], was developed to erode sub-scale accelerator grid surfaces in an accelerated fashion where 20-hrs of exposure in some regions produced wear that is equivalent to many 1000's of hours of in-space operation of a thruster. Photographs of a gridlet subjected to accelerated erosion testing are shown in Figure 2.10. The facility is fully automated and utilizes a 16-cm diameter radio frequency (RF) ion source (see Figure 2.10a) to ion bombard (and sputter erode) accelerator gridlet surfaces either through masks (Figure 2.10b) or directly to produce erosion patterns and surface texture similar to what is expected at the upstream entrance of apertures, on the webbing of the downstream face, and within the aperture barrels. Figure 2.10c contains a photograph of an ion beam striking a gridlet surface that was mounted to a water-cooled target plate. The target plate was rotated to different zenith angles relative to the ion beam to vary the angle of incidence of the ions on the gridlet and better simulate the erosion that occurs in an actual application. Note that the

azmuthal angle of the gridlet surface relative to the target mount was also varied by periodically stopping the test and rotating the mount.

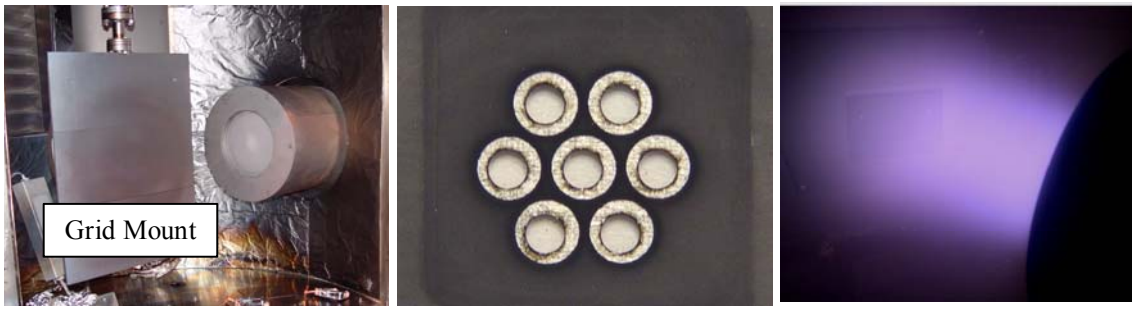

a) b) c)

Figure 2.10 Photographs of (a) ion beam deposition facility used for performing accelerated wear tests, (b) erosion mask placed over NEXIS CC accelerator gridlet and (c) ion beam eroding the upstream side of an accelerator gridlet through a mask.

An analysis was performed using CSU's ffx numerical simulation program to estimate how fast the upstream surface of a NEXIS accelerator grid will be worn during use in space. Sputtering data from Williams *et al.*[27] were used to estimate sputter erosion while estimates of NEXIS total impingement current in space conditions were obtained from Goebel[28]. Using the estimated erosion rates, the total mass loss was obtained, which was used to determine the time needed to expose the grid in the accelerated wear facility. Based on this analysis, 120 hours in the accelerated wear test facility would erode the surface to the equivalent of 3-yrs of on-orbit operation. This erosion process was only conducted with the carbon-carbon material and the resulting etch rate in this facility is at least 50 times higher than the erosion rate expected under deep space conditions.

It is noted that the accelerated wear testing technique can be used as an alternative to extended ground testing of ion thrusters to investigate certain lifetime issues. This is because accelerated wear processes performed in this way are not affected by backsputtering of beam target materials, which can decrease the sputter erosion of ion

optics surfaces in ground-based test facilities and therefore mask actual wear rates and surface feature evolution that would occur during an actual mission.[29,30]

A technique of directly impinging the upstream surface of the accelerator gridlet surface by operating at very high beamlet currents (as suggested by D. Byers, private communication, April 2005) was developed in a similar way as the accelerated wear technique using the ffx simulation program. Through an iterative process, a beamlet current operating point was found that would erode the upstream surface to the equivalent of 3-yrs of in-space operation in a matter of 22 minutes. Further information on this technique can be found in Ref. 31. The accelerated wear testing technique was used on a CC grid set designated as #1 while the direct impingement method was used on CC grid set #2.

2.5 Arc Suppression Switch System

To avoid unintentional arc damage of sensitive carbon-based surfaces, the electric-field breakdown tests were performed using arc suppression circuitry that consists of high-speed (opening) switches. Photographs of the switch and the enclosure used to mount it are shown in Figure 2.11. The circuit diagram of the switch placement in the power supply system is shown in Figure 2.12. Operation at total voltages up to 8 kV is possible with significant (>100x) reductions in charge transfer levels over typical laboratory power supplies equipped with fast arc suppression circuits.

The switch system is capable of limiting the charge transfer in an arc to values as low as 10 μC. To provide additional charge to an arc between the accelerator and screen gridlets, a capacitor is added across the grids and downstream of the switch. The value of the capacitor and the voltage applied between the grids was used to set the desired charge

transfer value (i.e., Q = CV with the assumption that the total charge stored in the capacitor will transfer through the arc). For this study, the arc transfer level was varied from 0.01 mC to 10 mC. A digital output signal from the switch control card that indicates when an arc occurs was monitored with a data acquisition system. Both switches open (70-100 μs delay) simultaneously when an arc event is detected between (a) the screen electrode and ground, (b) the screen and accelerator electrodes, or (c) the accelerator electrode and ground. The switches are capable of operating at a repetition rate of up to 10 Hz under a condition where a hard short exists between the grids. Care was taken to ensure that the trip point of the current sensors of 10 A was well below the peak current generated during an arc (>1000 A).

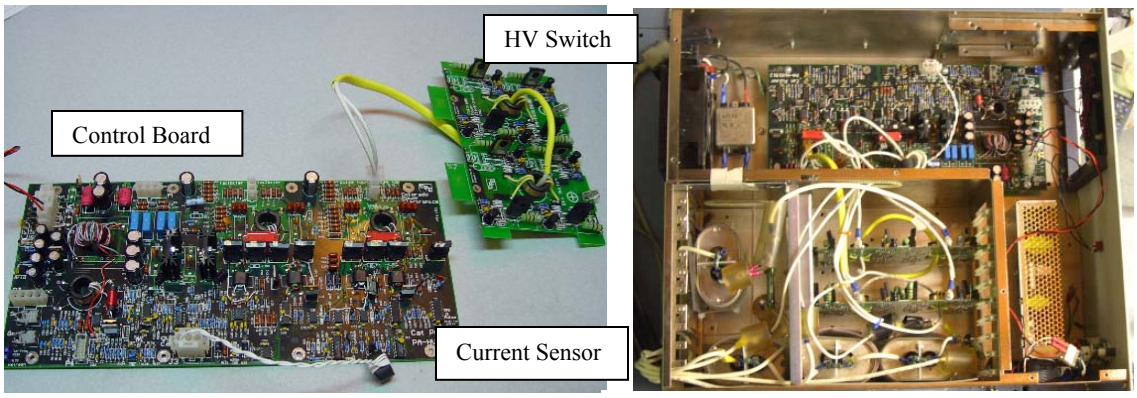

(a) (b)

Figure 2.11 Photographs of (a) the high voltage switch circuit boards and (b) the enclosure for the switch hardware.

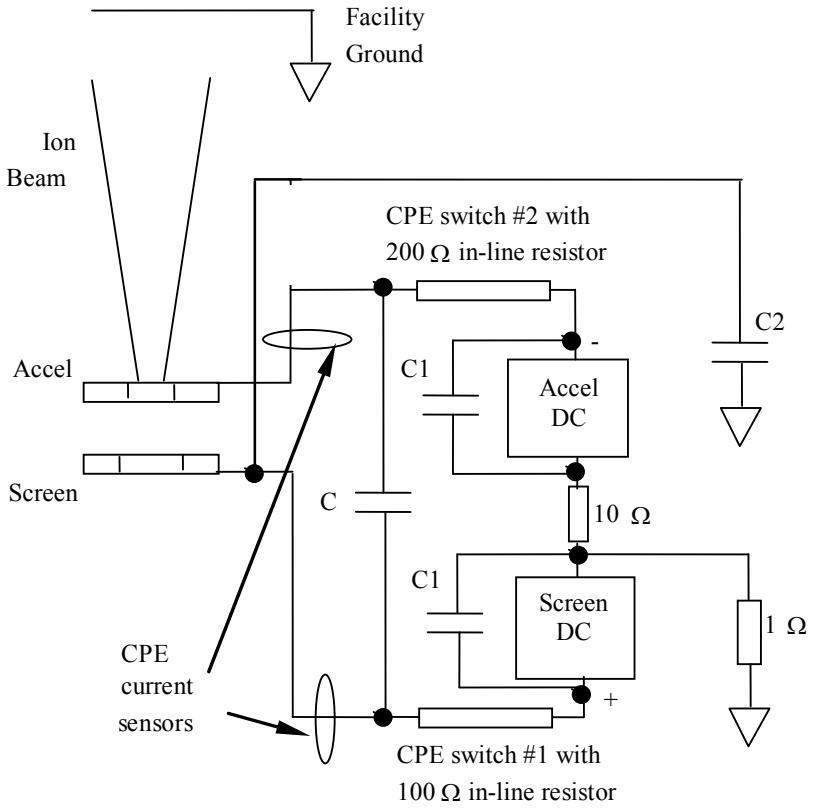

Figure 2.12 Circuit for setting the charge transfer in an arc between the screen and accel gridlets. C1 = ~2 μF. C2 (~1 nC) is the capacitance of discharge and heater supplies (not shown) relative to ground. C is varied to set the charge transfer at a given total voltage condition (i.e., $Q = CV_T$). No impedance other than the electrical leads themselves was used to limit the peak arc current flowing between the gridlets under test, however, reverse bias diodes (not shown) were placed across C to eliminate ringing.

2.6 Field Emission Analysis

The phenomena related to electrical breakdown between two electrodes have been investigated for over a century. The mechanism of voltage breakdown in vacuum is significantly different from gaseous discharges because the mean free path of the ionizing particles is much greater than the gap distance between the electrodes (~0.25-2.7 mm). In low-pressure regimes, it is well known that breakdown is associated with microscopic features of the surface. There are two main causes of electric field breakdown:

(1) emission of electrons due to high local electric fields, and (2) detachment, and subsequent impingement, of loose particles due to electrostatic forces produced by the applied field. Work on the second of these mechanisms has shown that particles injected deliberately into an electrically stressed vacuum gap can cause breakdown.[32] However, when a laser interferometer technique was used with a particle detection sensitivity of 10 μm, no particles were detected prior to breakdown when using electrodes covered with the debris from previously generated, high-current vacuum arcs.[33] In addition, other experiments with arced vacuum switches[34], have shown that field emission of electrons is as important or often more important than dust particles in determining whether an electrical breakdown will occur.

Before voltage breakdown (arcing onset) occurs, small electron currents are often observed. In 1928, Fowler and Nordheim developed a theory of the tunneling probability of an electron through a triangular potential barrier and applied it to predict the emission of electrons from a metal under the influence of a strong electric field.[35] This phenomenon is now referred to as Fowler-Nordheim field emission. The work function of a conductive material describes the height of the roughly square potential well that keeps conduction electrons from leaving the surface of the material. Applying an electric field to the metal makes the walls of the potential well slant, which enhances the probability that an electron can tunnel out of the well. Alpert et al.[36] showed, in a quantitative manner, the relationship between the observed values of pre-breakdown (field emission) currents with observed values of breakdown voltage. The principal outcome of Alpert's study was a phenomenological picture, which was applicable to broad area electrodes as

well as to point-to-plane geometries, and which provided an explanation for most phenomena observed in arcing studies.

The basic Fowler-Nordheim (F-N) model persists to this day, albeit with various modifications and enhancement. In particular, Latham[37] presents the derivation of the most useful form of the F-N equation:

$$\ln\left[\frac{J_{FE}}{E^2}\right] = \ln\left[\frac{1.54x10^{-6}\,A_e}{\phi}\,\mathrm{x}10^{4.52\,\phi^{-0.5}}\right] - 2.84x10^{9}\,\phi^{1.5}\,\frac{1}{E} \tag{2.8}$$

In Eq. (2.8), J_{FE} is the field emission current (in Amperes), E is the electric field (in V/m), A_e is the effective emitting area (in m^2), and Φ is the work function (in eV). If we assume that the field emission current flowing between the grids comes from a single microprotrusion at which the electric field is enhanced by a factor β_{FE} over the macroscopic value E existing at a perfectly smooth grid surface, then the microscopic field E_m acting at its tip will be given by

$$E_m = \beta_{FE} E = \beta_{FE}\,\frac{V_T}{\ell_g} \tag{2.9}$$

In Eq. (2.9), V_T is the total applied voltage difference between the electrodes and ℓ_g is the grid spacing. Substituting Eq. (2.8) into Eq. (2.9), yields a logarithmic form of the F-N equation expressed in terms of the externally measurable parameters J_{FE} and V_T,

$$\ln\frac{J_{FE}}{V_T^{\,2}} = \ln\left[\frac{1.54x10^{-6}\,A_e\beta_{FE}^{\,2}10^{4.52\phi^{-0.5}}}{\phi\,\ell_g^{\,2}}\right] - \frac{2.84x10^{9}\,\ell_g\phi^{1.5}}{\beta_{FE}}\,\frac{1}{V_T} \tag{2.10}$$

If the current-voltage data are presented in the form of an F-N plot, $\ln(J_{FE}/V_T^2)$ versus $1/V_T$, a straight line will result (assuming field emission is significant) with a slope of

$$\frac{d(\ln(J_{FE}/V_T^{\,2}))}{d(1/V_T)} = -\frac{2.84x10^{9}\,\ell_g\phi^{1.5}}{\beta_{FE}} \tag{2.11}$$

and an intercept of

$$\left[\ln(J_{FE}/V_T^{\,2})\right]_{V=\infty} = \ln\left[\frac{1.54x10^{-6}\,A_e\beta_{FE}^{\,2}10^{4.52\phi^{-0.5}}}{\phi\,\ell_g^{\,2}}\right] . \tag{2.12}$$

Thus, from the slope of an F-N plot, one can obtain an approximation of the local electric field caused by a surface imperfection or protrusion extending from the ion optics surface by multiplying the field enhancement factor, β_{FE}, by the applied electric field, V_T/ℓ_g. Experimentally, the quantities measured are the field emission current, J_{FE}, and the total applied voltage, V_T. Of important note is the work function of the surface, which when at low temperature and in the presence of gases (even at low pressure) can often be lower than the work function of a perfectly clean and flawless surface comprised of atoms from the bulk material. Herein, we assume that the work function is at the value of the bulk material when using Eq. 2.11 to reduce experimental data and obtain estimates of the field enhancement factor. This assumption can cause one to vastly underestimate the area of a protrusion found from Eq. 2.12 It is argued that, although this assumption yields unrealistic small values for the area of a protrusion, the work function is not changing significantly during a test, and, consequently, changes in the enhancement factor observed during a test are due to changes in the geometry, number, and size of the protrusions responsible for the observed level of field emission. Alternatively, the reader could interpret the field enhancement factors reported herein as being proportional to $\beta_{FE}/\phi^{1.5}$.

At high vacuum there are few ionizing collisions within the electrode spacing, therefore, the electrodes instead of the background gas are the primary source of material that can be ionized. The presence of an electric field between two electrodes will result in field emission of electrons from the negative electrode (the accelerator grid) that can impact and heat small areas of the screen grid upon colliding with it, and give rise to evaporation of the screen material or to the liberation of absorbed quantities of gas. An arc can develop in the stream formed of the vapor of liberated or evaporated gas (see Figure 2.13).

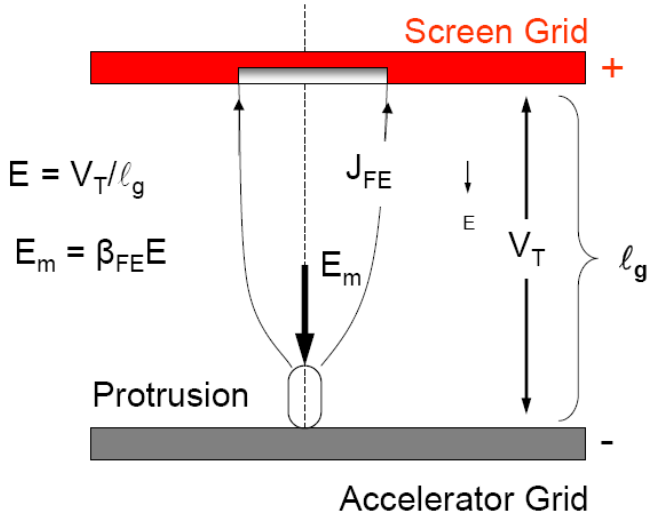

Figure 2.13 Illustration of the field emission mechanism.

Figure 2.14 contains a typical F-N plot. The usable field emission region between the arrows was used to obtain the field enhancement factors. No F-N data are used before or after this usable field emission region. The breakdown voltage is at the arc initiation point. Manually recorded data taken over longer periods of time are often used to construct higher quality F-N plots. The field enhancement factor is a good indicator of the quality of a grid surface, and, as explained later, can be used to predict the breakdown

voltage. Specifically, as the enhancement factor decreases, the surface quality improves and the breakdown voltage increases. Experimental evidence suggests[38,39] that the micro-protrusions responsible for field enhancement, sometimes invisible by ordinary optical methods, can serve to multiply the average electric field by a factor of hundreds or more. Figure 2.15 is a scanning electron micrograph of a projection on an aluminum surface capable of high field magnification (from Ref. 39).

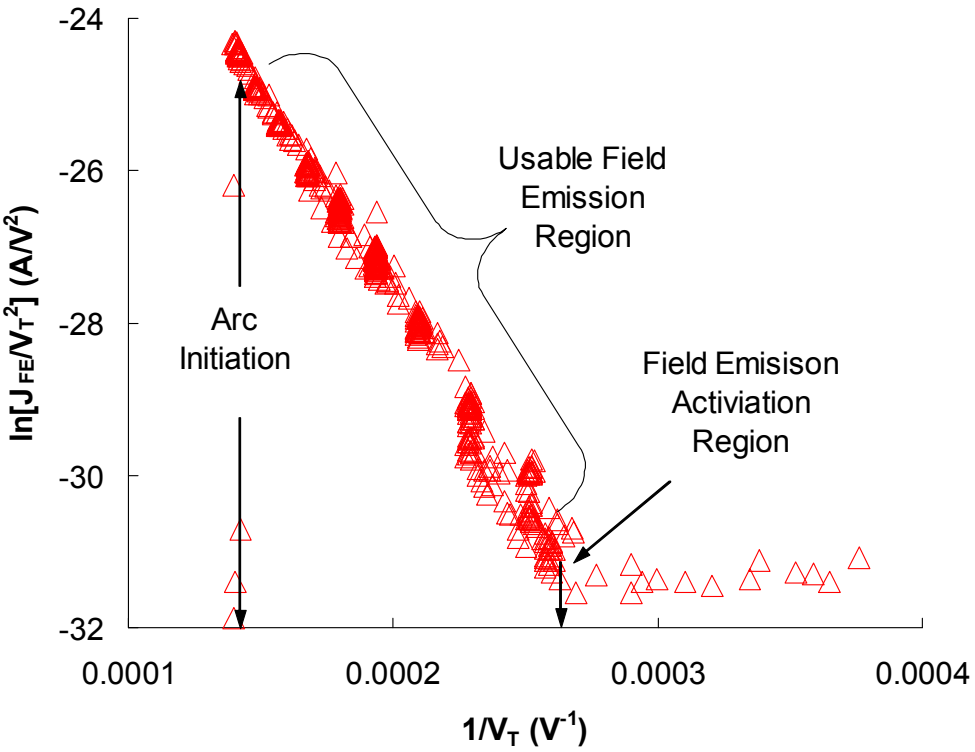

Figure 2.14 Typical Fowler-Nordheim (F-N) plot.

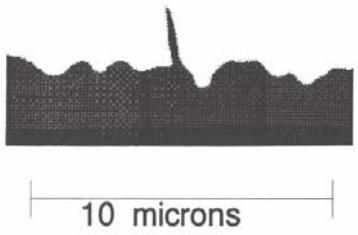

Figure 2.15 Protrusion on a surface (from Ref. 39).

Figure 2.16 shows a typical plot of the variation of the localized electric field enhancement factor with the number of conditioning arcs (1 mC/arc) for a set of CC gridlets at an electrode spacing of 0.5 mm. One possible reason for the initial drop in the enhancement factor in Figure 2.16 is that relatively sharp protrusions on the surface are vaporized by the conditioning arcs. Once sharp protrusions are removed or blunted, subsequent smaller emission-producing sites are blunted as each conditioning arc is applied, hence the slower drop in the enhancement factor after 100 arcs. Another possibility is that the initial breakdown is caused by a loose particle on the surface. The slight increase in the enhancement factor at 600 arcs could be due to the temporary sharpening of a protrusion or the creation of new points.

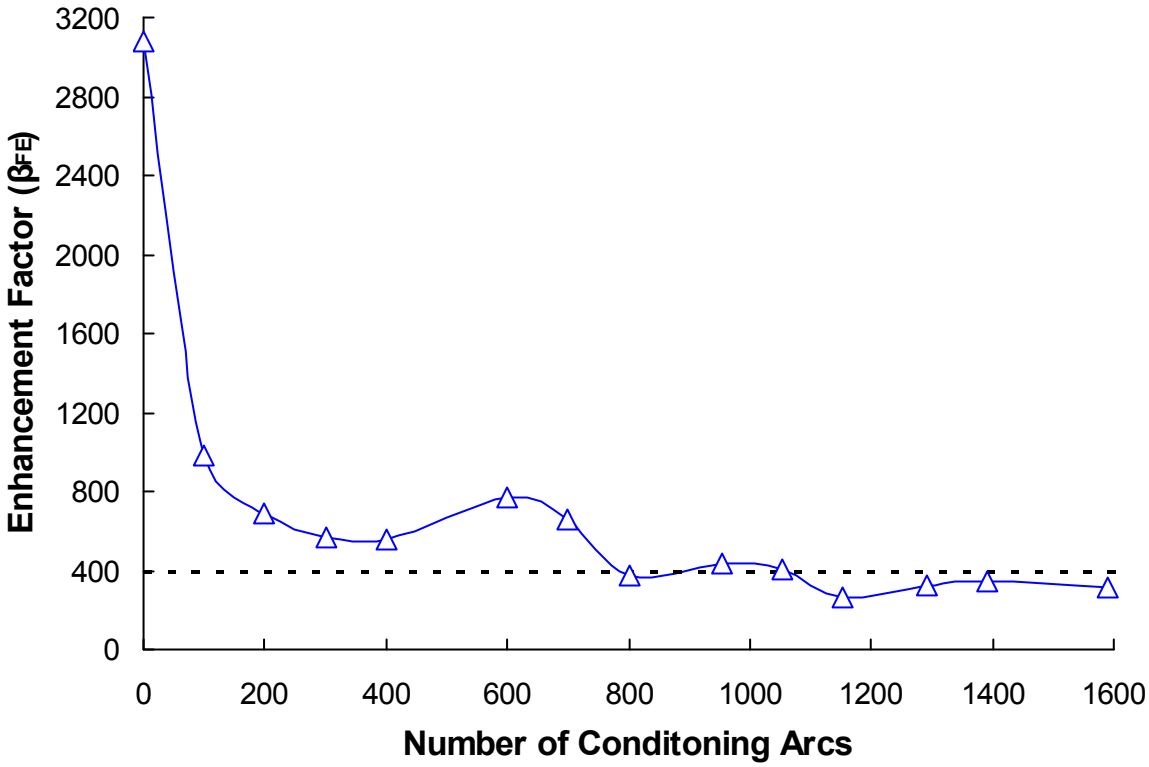

Figure 2.16 **Electric field enhancement factor variation with number of conditioning arcs for carbon-carbon gridlets.**

Using Eq. 2.12 one can also determine an approximation of the emitting area. The emitter area is extremely sensitive to the intercept, however, and calculated areas can vary over unphysical ranges. As mentioned above, the large uncertainty in emitter area is most likely caused by adsorbed surface layers and impurities, which alter the pre-exponential term in the F-N equation.[39] No estimates of the emitter area are presented herein due to the large and hard-to-quantify errors associated with these estimates.

2.7 Weibull Statistical Analysis

In 1939, Waloddi Weibull developed a method for statistically evaluating the fracture strength of materials using small population sizes (i.e., small numbers of measurements).[40,41] This method, now called Weibull analysis, can be used to make predictions about the life of a product, compare the reliability of competing product designs, statistically establish warranty policies, or proactively manage spare parts inventories. In academia, Weibull (also referred to as log-normal) analysis has been used to model such diverse phenomena as the length of labor strikes, AIDS mortality, and earthquake probabilities. The Weibull distribution has the great advantage in reliability work in that through adjustment of the distribution parameters, it can be made to fit many life distributions. The major use for the Weibull distribution is as a time-to-failure model since by proper choice of its parameters it can represent the lifetime characteristics of a wide diversity of equipment. Many researchers attribute the success of Weibull analysis to its ability to identify the weakest link in complicated systems. In the case of ion propulsion systems that utilize biased electrodes, Weibull analysis can be used to characterize the mean period between arcs that occur as a function of operating condition and geometrical configuration. The primary advantage of this analysis technique is its

ability to provide arc period characteristics with extremely small sample size (i.e., the attainment of accurate arc rate data at low arc rate conditions in a few hours is possible). In addition to providing statistically correct estimations of the mean arc period, Weibull analysis provides a simple graphical form for presentation of data that allows one to easily distinguish between different populations. Specifically, Weibull plots are useful for graphically demonstrating if one grid surface is better than another in terms of arcing rate or if a grid surface is degrading over time due to sputter erosion processes for example. In our Weibull plots, the horizontal scale is the time between two successive arc events and the vertical scale is the cumulative distribution function (CDF), describing the chance that an arc will occur after a given amount of time. The characteristic arc period is defined as the amount of time when 63.2% of the arcs in a given population will have occurred. The characteristic life (a.k.a., the B63.2 life) can be determined on the plots in this thesis by noting the intersection of the data trend line with the horizontal dashed line drawn at 63.2%. The characteristic life is equivalent to the arc period.

The 2-parameter Weibull distribution function[42] was used to fit the arc period measurements, i.e.,

$$f(t) = (\beta_w/\eta)(t/\eta)^{\beta w-1} \exp-(t/\eta)^{\beta w} . \qquad (2.13)$$

In Eq. (2.13), the value of β_w indicates whether the measurement of interest is increasing, constant, or decreasing with time. A value of $\beta_w<1$ indicates that either (a) the grids are arcing more in a "burn-in" period at the beginning of a test or (b) the grid arcs are occurring in clusters where one arc causes a series of follow-on arcs. A value of $\beta_w = 1$ indicates a constant arc rate probability independent of the test duration. A value of $\beta_w>1$

indicates an increasing arc period with time. In our plots, $\beta_w>1$ would correspond to either (1) an increasing amount of time between arcs as a test is being conducted or (2) the occurrence of an arc results in an improved grid condition that is less likely to arc again. Finally, the Weibull characteristic life, η, is a measure of the scale in the distribution of data, which corresponds to the mean arc period.

The goals of the statistical analysis included (1) determining if arc conditioning performed prior to a test effects the mean arc period, and (2) measuring the mean arc period as a function of the electric field value.

The approach used for this study was to characterize the electrical breakdown behavior (i.e., record the time of each arc event over a preset period of time) using the lowest arc charge transfer setting of our power supply system (~0.01 mC) after conditioning the accelerator gridlet with a number of arcs at a higher arc charge transfer setting. A data acquisition system was used to record the time of an arc event from a signal in the arc suppression switch circuitry. The time of an arc event was monitored using a time stamp resolution of 0.5 sec, and, consequently, the minimum resolution of an arc period measurement was ~1 sec. Figure 2.17 shows a typical plot of the arcs recorded during the operation of a gridlet set over a 3-hr period.

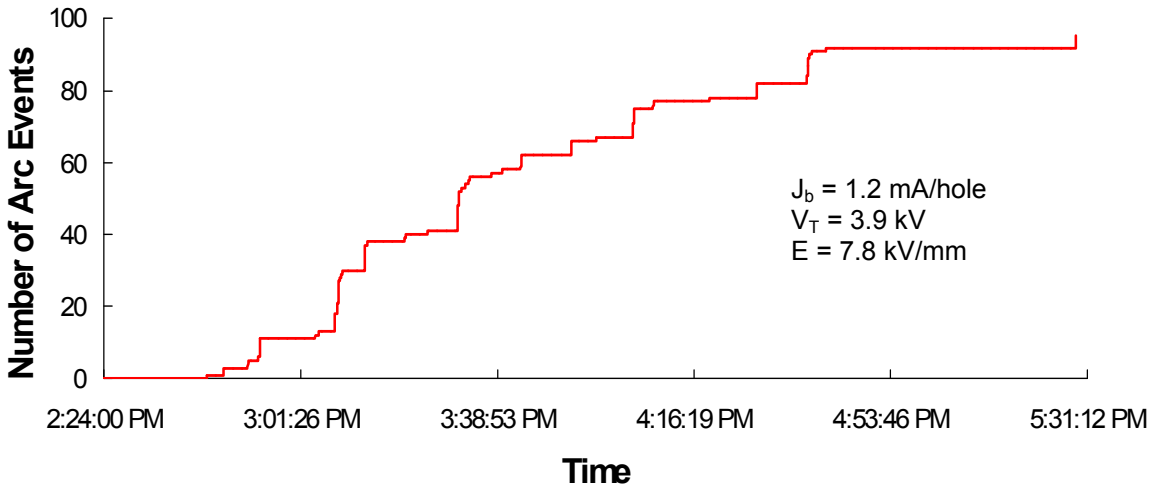

Figure 2.17 Arc history during a 3-hr period of operation of a set of CC gridlets operated at a total voltage of 3.9 kV.

For statistical analysis purposes, the arc events that occurred in a particular test were ranked from the shortest period between two arcs to the longest period between two arcs, and then plotted on a Weibull plot. Figure 2.18 shows how the time between arcs was determined while Figure 2.19 shows a Weibull plot of these measurements.

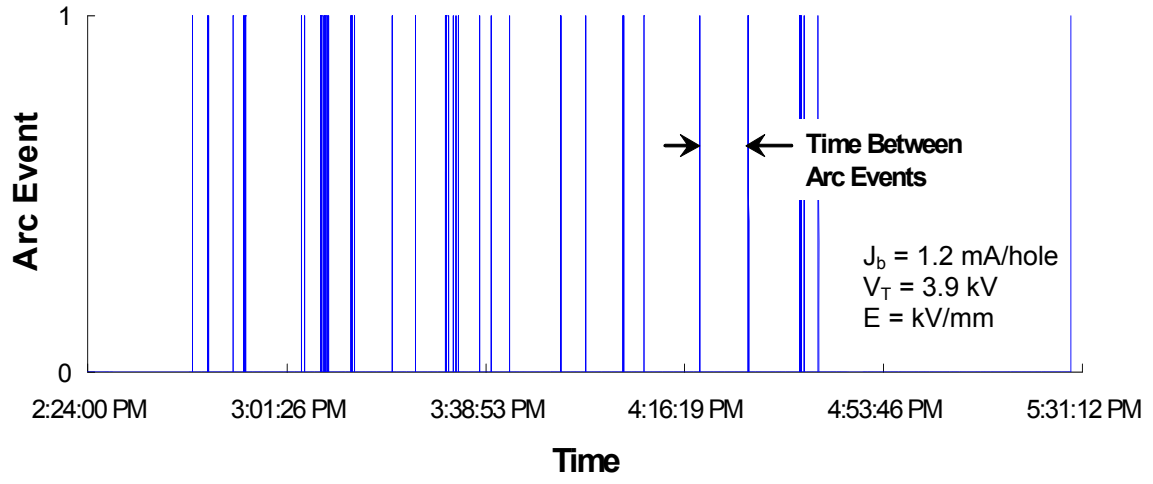

Figure 2.18 Arc event history showing how the time between arc events was determined.

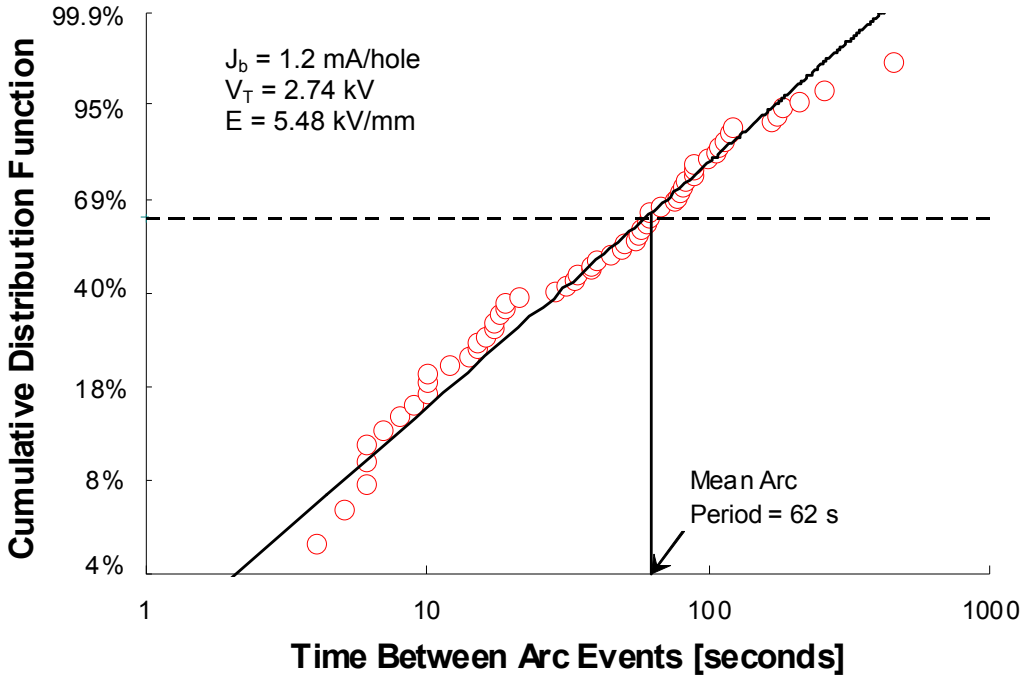

Figure 2.19 Typical Weibull plot obtained with beam extraction. One would expect that as the electric field is increased the curve would move to the left indicating more frequent arcing. Note that most data sets were obtained during 3-hr long runs.

Weibull analysis provides accurate estimates of most physical phenomenon with the minimum number of measurements.[40-43] This feature is important for ion propulsion applications because it minimizes the amount of time required to perform a given test. The Appendix presents a method of how to use Microsoft Excel to generate a Weibull plot from a given set of measurements and extract the characteristic life and slope parameters.

2.8 Review of Research on Electrical Breakdown

In tests described herein, arcing characterization tests were performed to determine the effects of surface conditioning, intra-grid electric field, beam extraction time, below nominal grid spacing, active gridlet area, and beamlet current. Post test

inspections were performed to locate areas where arcs occurred, and numerical simulations have also been performed to determine regions where the highest electric fields exist and regions where the highest concentrations of charge exchange ions are being collected.

When conducting experiments to determine the origin of electric field breakdown under vacuum between closely spaced electrodes, a wide range of issues concerning the experimental conditions need to be considered and carefully chosen to characterize the arcing behavior of a given material properly. The fact that our experiments involve materials with drilled apertures along with operation under conditions where ion beamlets are being extracted adds additional considerations.

Two overriding issues were identified as important in the evaluation of the arcing behavior of gridlet surfaces under conditions where ion beamlets are being extracted:

1) Wear of test accelerator gridlet surfaces by ion bombardment is needed to simulate the surface condition of an actual accelerator grid during in-space operation,

2) Conditioning of test accelerator gridlet surfaces with arcs of specified coulomb transfer levels and applied voltage is needed to prepare gridlet surfaces worn by ion bombardment prior to characterization of arcing behavior at various electric field values.

The primary goal of the effort was the determination of the electric field value where nearly continuous arcing occurs at nominal and reduced grid spacing for various levels of simulated wear and arc conditioning values. Note that the onset electric field

was evaluated at the minimum coulomb transfer value per arc of the equipment, which is about 10 μC at nominal total voltages, during ion extraction operation.

Other areas of investigation included studies of how the onset of arcing data scales from gridlet tests to full-size grids and how the active gridlet area-to-total gridlet area ratio might affect the onset of arcing measurements. An additional issue was determination of the magnitude of the total voltage that may be necessary at nominal spacing to induce arcs (when the accelerator gridlet surface is in a pristine BOL condition).

Measurements of arcing threshold data collected on drilled and un-drilled ion optics material (without ion beam extraction) have been made by Goebel[15]. The arcing threshold data were presented in terms of onset electric field versus spacing. These data showed that arcs with charge transfer value of about 1.0 mC appeared to be a near optimum value to condition the surface and increase the maximum voltage standoff capability of the grids without causing damage that results in more frequent arcing.

A review of high voltage arcing experiments conducted under vacuum provided data on the sensitivities of various experimental conditions on the voltage standoff capability of a given electrode material. Below is a summary of the main factors that influence the arcing characteristics of electric field induced breakdown.

2.8.1 Conditioning Process

By conditioning one refers to any method, prior to application of high voltage, which reduces field emission and improves the electric field strength capability of a vacuum gap. There are several types of conditioning including heat treatment, ion etching, acid etching, ultra-pure water rinsing, and electrical conditioning. The types of

conditioning employed depend on the application. Heat treatment involves simply heating up the electrodes to temperatures in the range of 200-1000°C to remove emitting sites associated with adsorbed gases, oils, and high vapor pressure contaminates. Ion etching is commonly performed by adding ~1 Torr of argon or hydrogen to a chamber holding the electrodes and starting a ~100 V DC glow discharge with a current density of ~1mA/cm^2. This process is believed to have the effect of sputtering away high field enhancement spots.[37,44] Direct ion bombardment, has also been found to reduce the conditioning period for a surface to reach a given electric field capability.[45] In addition, acid treatments and ultra-pure water rinsing are effective at reducing field emission[46], however, electrical conditioning is perhaps the most effective and widely used type of conditioning.[37]

The goal of electrical conditioning is to remove the worst of the field emission sites through controlled breakdown. At high fields, sharp tips and protrusions can vaporize, which usually initiates a full breakdown causing damage to the electrodes. If, however, a large resistor is used to limit the current, the damage to metal electrodes can be minimized. Gruszka and Moscicka-Grzesiak[47] studied conditioning of several types of metals with varying degrees of surface finish. They found that there is an optimum conditioning current that is a function of both the material and the surface roughness. They also found that lower currents work better for rougher surfaces and that rougher surfaces show the greatest improvement after conditioning. Conditioning is generally required to obtain a reproducible current-voltage relationship and breakdown voltage.

2.8.2 Residual Gas and Facility Effects

Residual gas in the vacuum chamber affects breakdown voltage. At pressure – grid-gap products less than the Paschen breakdown minimum, there are two major effects to consider: (1) Changes in the work function of the metal by absorbed gas and (2) Sputtering of the metal surface by low-energy gas ions. There is some question about the influence of these effects on breakdown when the surface is well conditioned. Hackman and Salman[48] measured the breakdown voltage for stainless steel gaps of 0.76, 0.50, and 0.30 mm over a hydrogen pressure range from $3x10^{-9}$ to 10^{-2} Torr and observed a near constant breakdown field. The effect of Paschen breakdown was only observed in the largest gap at the highest pressures, where the breakdown voltage drops rapidly with increasing pressure.

Although Hackman and Salman observed little effects of residual gas in their experiment with hydrogen, others have found that the type of residual gas and level of conditioning are important. Bloomer and Cox[49] found that adding oxygen to their system with a field applied improved the breakdown voltage while adding argon had no effect. Since the ionization cross section and sputtering properties of argon and oxygen are similar they concluded that an increase in the work function of the molybdenum electrodes by 1.7 eV due to oxygen chemisorption was responsible. Among the gases studied (H_2, D_2, He, Ar, N_2, SF_6 and dry air), helium, followed by nitrogen, consistently give the best results; i.e. as measured by the improvement in the hold-off voltage of the gap and the increase in the slope of the F-N plot of the current-voltage characteristic.[44,50,51] Further, the physic-sorption process associated with ion bombardment phenomena has been shown to effect the work function.[37] Hackman and

Raju[50] suggest that the fact that He is adsorbed more efficiently than Ar ions could offer an explanation of why He gas gives a higher breakdown voltage than argon.

At higher pressures, the level of conditioning may also determine the effect of residual gas. With non-conditioned stainless steel electrodes with various gap lengths Cooke[52] measured a six-fold improvement in the breakdown voltage with nitrogen pressures in the millitorr range compared to the breakdown voltage at 10^{-4} Torr. The effect, which was reduced for partially conditioned electrodes, was attributed to ion bombardment and sputtering of emitter sites.

Collazo *et al*.[53] reported an increased emission current they attributed to the presence of adsorbates on carbon nanotubes and explained that the adsorbates would introduce a resonant state enhancing the tunneling probability of the electrons. Adsorbed gas on the grid surface can be liberated under electron or ion bombardment by pre-breakdown current to provide a medium in which sufficient current amplification occurs to produce breakdown.

In many instances, if the electrodes are not outgassed, micodischarges are observed. This effect was observed by a number of researchers.[54, 55] The microdischarges were attributed to a cascade process in which ions produced at one electrode can cross the gap and produce ions on the opposite electrode. The microdischarges consist of currents of micro-amperes and duration of milli- to micro-seconds. This process seems to occur only under certain conditions, namely when there is a layer of oxide or other contamination on the electrodes such that the impinging ions can produce secondary ions in approximately a one-to-one ratio and/or can also place materials on the surface having lower work function properties. After the anode was heated, the threshold voltage for

microdischarges was increased by a factor of about three. This was attributed to the removal of oxides or adsorbed gases there by reducing the probability of ion production at the anode.

Surface contamination may be due to the careless handling of electrodes or due to the pumping system used. Other researchers[56] have investigated this and concluded that the effect of an oil film on the electrode surfaces facilitates the occurrence of microdischarges.

The desorption and adsorption of gas from the electrodes as the voltage is increased and decreased can also lead to an abrupt change in the slope of the Fowler-Nordheim plot. This effect could be attributed to the adsorbed gases altering the potential barrier at the surface of the metal and hence modifying the field emission process.

The concern over possible oil contamination of the electrodes during this investigation led to the replacement of the oil-based pumping system with an oil free cryopump facility along with a high-purity feed system. Prior to any testing, the facility was pumped down to base pressures in the mid 10^{-7} Torr range for 12-15 hours after exposure to the atmosphere.

2.8.3 Electrode Surface Preparation

The ideal electrode surface would be one that is free of microparticles that are loosely attached to the material. There is thus a need for an electrode finishing treatment in which the operational surface is first subjected to some sort of microscopic polishing procedure and then to a final cleaning treatment for removing all traces of superficial debris. Metallurgical polishing techniques are based on mechanical, chemical, and electrochemical processes.

Causes of electron emission at lower fields can be the presence of oxide films or absorbed particles on the surface. The lack of cleaning the electrodes prior to testing can also lead to electron emission characteristics that are not easily described with Fowler-Nordheim theory. A lack of cleaning the electrodes increases the chances of "whiskers" being left on the material surface, which can originally be lying down on the cathode, which are then gradually pulled upright by the increasing electric field as the voltage is increased.

Microprotrusion regions like cracks, grain boundaries, and edges of pits can cause high field emission to originate from the cathode surface.[57] This current, in turn, would heat both the anode and cathode surfaces causing them to give up adsorbed gas, which could then be ionized by the field emitted electrons causing a flow of both negative and positive particles between the electrode and an enhanced likelihood of initiating a breakdown. This again shows the need to consider carefully the surface preparation to prevent surface defects in materials used for high voltage electrodes. Cox and Williams[58] developed a probe-hole method to locate the emission sites and found an insulating particle on a surface that was dominating the emission from their sample. They postulated that the very first initial breakdowns probably were caused by these insulating particles. Jumps in the current, which increased with voltage, to much higher values at a voltage just below the breakdown voltage and then drop to very small values are probably due to the transit of the insulating particles from one surface to the other.[58]

As will be discussed in the next chapter, each of the electrodes tested in this study were carefully cleaned, smoothed (made less rough), and heated prior to testing. In addition, the experimental equipment coming into contact with the electrodes was

cleaned and, along with the electrodes themselves, only handled after dust-free nitrile gloves were worn. However, the grid materials were cleaned in laboratory air so small dust particles could still exist on the surface after chamber pump down.

2.8.4 Electrode Separation

The gap length has been shown to have a significant effect on the origin of electric field breakdown.[39] Latham[37] and numerous other researchers have concluded that for small gaps ($d \leq 0.5$ mm), breakdown tends to be field dependent, whereas at large gaps ($d \geq 2$ mm) breakdown becomes voltage-dependent. In other words, the small gap behavior corresponds to breakdown being initiated by the field emission mechanism described earlier, while the large gap behavior becomes dominated by the microparticle processes also discussed earlier in this chapter.

For plane-parallel gaps that have been prepared according to optimum specifications (i.e., highly polished flat plates), the typical dependence of the breakdown voltage (V_{Tb}) on electrode gap will take the form illustrated in Figure 2.20 by Alpert[36] and Latham[37]. The breakdown voltage is defined as the point where a high current, low impedance luminous arc forms between the electrodes. As described in reference 37, for $d \leq 0.5$ mm the linear relation

$$V_{Tb} = E_b d \tag{2.14}$$

holds, and for $d \geq 2.0$ mm, i.e. beyond the transition region $0.5 \leq d \leq 2.0$ mm, the power relation

$$V_{Tb} = kd^n \tag{2.15}$$

(where V_{Tb} is in kV, k is in kV/mm, and d is in mm) begins to dominate. In equation 2.15, k and n are constants of the material and geometry. At high electric fields, k and n

can vary between ~30-45 kV/m and 0.5-0.8, respectively, depending on surface properties and the geometry of the electrodes.[37, 59] Other data shown in Figure 2.20 by Goebel[15], Kohl[60], and Staprans[61] illustrate the variation in breakdown voltage due to changes to the geometry and experimental setup.

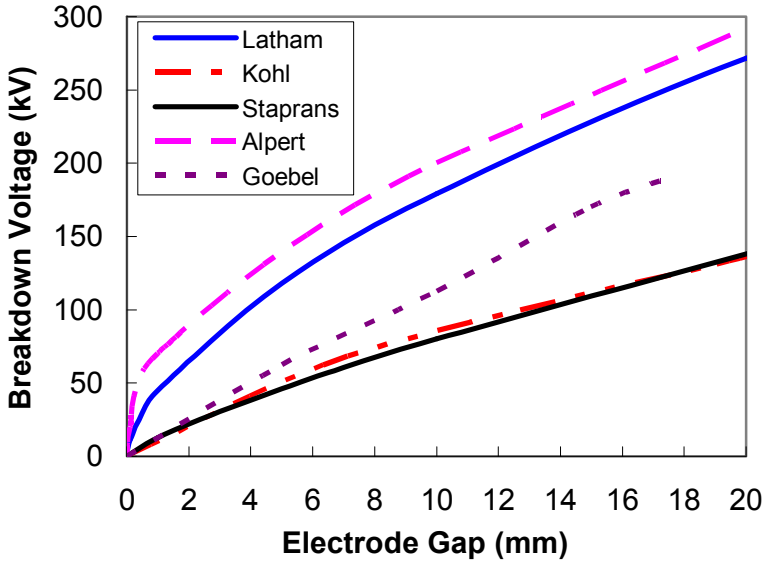

Figure 2.20 Breakdown voltage versus gap spacing for refractory metals with data from Goebel[15], Alpert[36], Latham[37], Kohl[60], Staprans[61].

Due to the variation in breakdown voltage shown in Figure 2.20 for non-perforated electrodes, a need to analyze the voltage standoff capability of more complex geometries like accelerator grids for ion sources is required. In addition to the effect that grid spacing has on the mechanism for voltage breakdown, the aperture geometry, aperture layout pattern, and overall size of the electrodes can also play a significant role.

2.8.5 Electrode Geometry

In high voltage gaps, a term referred to as the "area-effect" needs to be considered when electrodes are required to sustain a given electric field. This "area-effect" refers to the fact that an increase in the electrode gap at a constant electrode area will lower the

electric field at a given applied voltage and hence result in a higher voltage hold-off capability, whereas an increase in the area at constant electrode gap will generally lead to a lower voltage hold-off capability since more hazards in the form of emitting sites and microparticles will be present. This "area-effect" has been shown to account for discrepancies in published breakdown characteristics of plane-parallel electrode gaps of a given material, such as stainless steel.[62]

When conducting breakdown characterization experiments, a plate and ball geometry is typically used to avoid edge effects in the breakdown region that might cause additional arcs. When the local curvature differs from the main surface area (such as at the edges) local variations in the lines of equipotential can occur. The resulting distortion can lead to a divergence of the lines of force, and is equivalent to a lens effect, which can lead to field magnification. Byers experimentally showed that rounded edges when compared to square edges do provide larger breakdown fields between grids with holes.[63] The effect is illustrated in more detail in Figure 2.21, which contrasts the distribution of electric field lines associated with pairs of unprofiled (where the sharp edges result in a local macroscopic enhancement of the gap field) and profiled electrodes (which give a uniform surface field). Ideally, the profiled electrode ensures that the electrode surface applied field never exceeds its uniform mid-gap value. The Rogowski profile[64], defined in terms of the gap length, is preferred when practical and is defined such that short gaps require a sharper radius profile compared to large gaps.

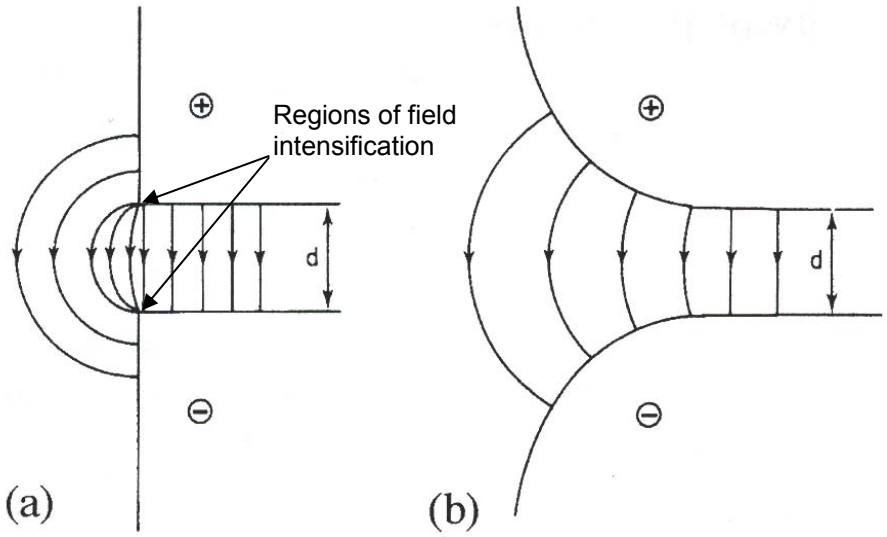

Figure 2.21 The electric field lines associated with a planar electrode gap formed from (a) unprofiled electrodes, and (b) profiled electrodes. [37]

The issue of profiling becomes more significant when referring to electrodes with apertures drilled into them, as is the case with ion thruster grids. Numerical simulations were used to determine the regions where the highest electric field exists on the accel electrode. Figure 2.22 is an electric field plot at a beamlet current of 1 mA/hole for the NEXIS geometry operated at a net voltage that corresponds to a specific impulse of 7500 seconds. As expected, the highest electric field conditions on the negatively biased accel surface are at the upstream entrance of an aperture. The presence of apertures may provide numerous emission sites due to the hole forming operations. These emission sites may be made more emissive by the macroscopic field enhancement of the hole edge. Byers conducted tests with stainless steel electrodes with different numbers of holes and found that the voltage breakdown level decreased with the number of holes drilled in the grids.[63]

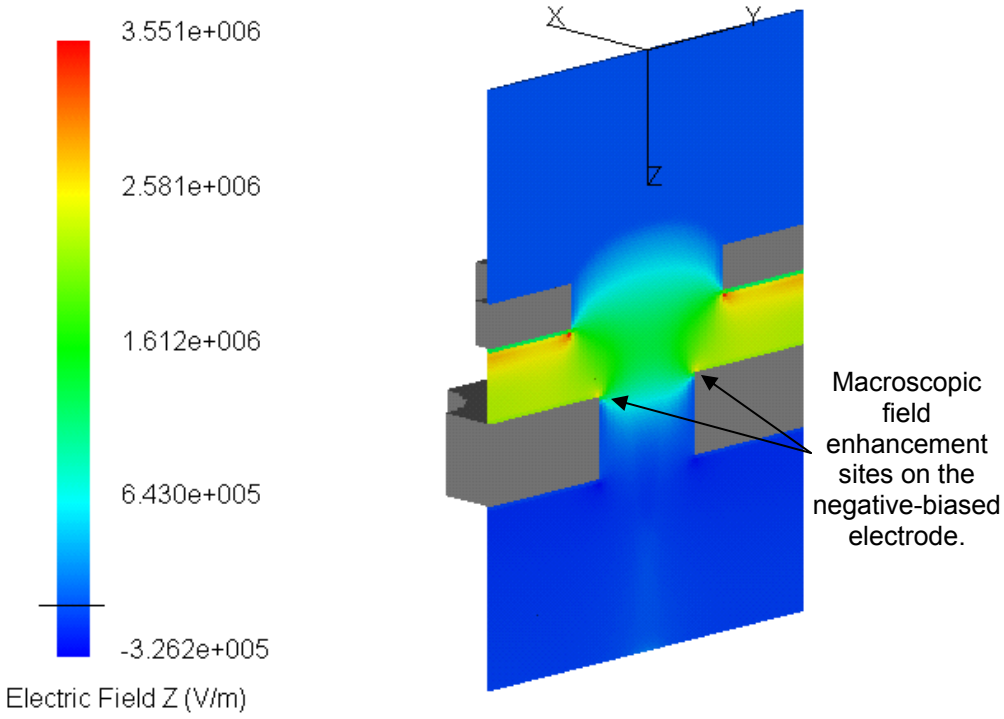

Figure 2.22 Electric field with ion extraction from ffx simulation results for NEXIS geometry at BOL.

2.8.6 *Impact of Electrical Circuit*

When conducting electrical breakdown experiments, consideration needs to be given to the amount of stored energy in the power supply and the possible damage that a large amount of capacitive energy transferred during an arc can have on the subsequent voltage standoff capability of the electrode material. This energy plays a vital role in feeding the growth of the initiating arc and therefore determines the extent of the surface damage ultimately sustained by electrodes during a breakdown event. Damage can be in the form of melting or evaporation of electrode material due to the localized energy deposition on the surface during the arc. To avoid the potentially irretrievable loss in voltage hold-off capability of a gap, it is imperative to take precautionary measures, firstly to limit the available energy, and secondly, to control its rate of dissipation. The

lack of concern with regard to the stored energy in the power supply and the amount of energy deposited on the grid surface during an arc is one possible reason for the problems encountered during earlier development and testing of carbon-based grids for ion thruster.[16, 65]

In order to avoid unintentional arc damage of sensitive surfaces (such as carbon-carbon composite and pyrolytic graphite), electric field breakdown tests need to be conducted using arc suppression power supply systems as described in Section 2.5. The minimum charge transfer value per arc of the equipment used for this study was 10 μC. This value of charge transfer per arc is not believed to cause damage to a surface.[15]

The experimental procedure for breakdown voltage determination was to increase the voltage slowly to (1) detect the onset of field emission and (2) then watch for the voltage where the rate of increase in emission current began to rise. Additional increases in voltage after condition 2 is reached typically correspond to the breakdown voltage limit. All breakdown testing was performed with the arc suppression systems set at the lowest charge transfer setting of 10 μC per arc. The initial breakdown voltage is usually attributed to the presence of surface particulates and/or absorbed gases. Therefore, to obtain the actual maximum breakdown voltage of the material, the breakdown voltage was defined as the voltage where continuous breakdown occurred. The following chapter presents the electric field breakdown characteristics for several materials, Coulomb transfer conditioning levels, and gap spacings. In addition, the impact of surface erosion via energetic ion bombardment was studied.

3. EXPERIMENTAL RESULTS AND DISCUSSION

This chapter presents the experimental results of the electric field breakdown characteristics of carbon-based and molybdenum materials. The field emission data obtained on the NEXIS-style carbon-carbon gridlets before and after undergoing accelerated erosion processes are presented first. Then data for applied and enhanced electric field breakdown as a function of conditioning arcs, beamlet current, interelectrode gap, and electric field are presented. Next Weibull statistical analysis is used to characterize the arc rate as a function of applied voltage and grid operational lifetime. Similar data are then presented for pyrolytic graphite, molybdenum, and Poco graphite along with comparisons. Finally, a preliminary study of the effect that active area has on the electric field breakdown characteristics is presented.

3.1 Carbon-Carbon Composite Material

Although a range of materials were tested for this study, carbon-carbon (CC) composite material was the primary focus of the electric field breakdown work due to the numerous samples generously provided by the NASA Jet Propulsion Laboratory and the promise that this material has for ambitious missions. The fabrication of the NEXIS-style CC gridlets used for this study is described by Beatty *et al.*[19]. The only difference being that the gridlets in our study did not receive the final surface coating by chemical vapor deposition after the laser machining process was performed to drill the holes and cut the outside dimensions of the gridlet plates. This final process typically fills the open voids exposed during laser drilling and provides a surface finish of glassy carbon. Although this final coating increases the voltage standoff of the grid assembly,[15] it is expected that the coating will erode away on some surfaces after a few thousand hours into a mission.

3.1.1 Field Emission Evaluation

Fowler-Nordheim (F-N) data analysis described in Chapter 2 was used to investigate how accelerator grid surface geometry and microscopic features can enhance the applied electric field and lead to arcs. Experiments have been conducted to determine how the field emission characteristics vary with and without beam extraction, grid spacing, and grid surface conditioning. As a check, the data were also analyzed with regression analysis using Schottky emission and insulation leakage models by plotting the measurements using the appropriate mathematical form of these relations and judging the quality of the straight line plot that was obtained. Although other models occasionally provided a good curve fit, only the F-N model resulted in consistently high correlation coefficients. Figure 3.1 contains typical F-N data taken in this investigation.

Field emission plots are shown in Fig. 3.2 for various electrode gaps. Although similar plots were taken for ten different grid gaps, only four (ℓ_g = 1.04 mm, 1.27 mm, 1.78 mm, and 2.70 mm) are shown as examples. The data from Figures 3.1 and 3.2 fall on straight lines over a range of several orders of magnitude, which suggests that F-N field emission is responsible for the monitored currents and that very little leakage is occurring across the insulators. A comparison between data taken by increasing and then decreasing the applied voltage to the grids was performed, and the resulting plots were nearly identical with no evidence of hysteresis. Care was taken to ensure that stable emission conditions were established before the F-N measurements were made and that no arcs occurred during a test. The variation of the slope of the F-N plots with grid spacing can be interpreted as a change in field enhancement, β_{FE}, with grid spacing, since it may be supposed that the work function of the emitting point(s) is constant.

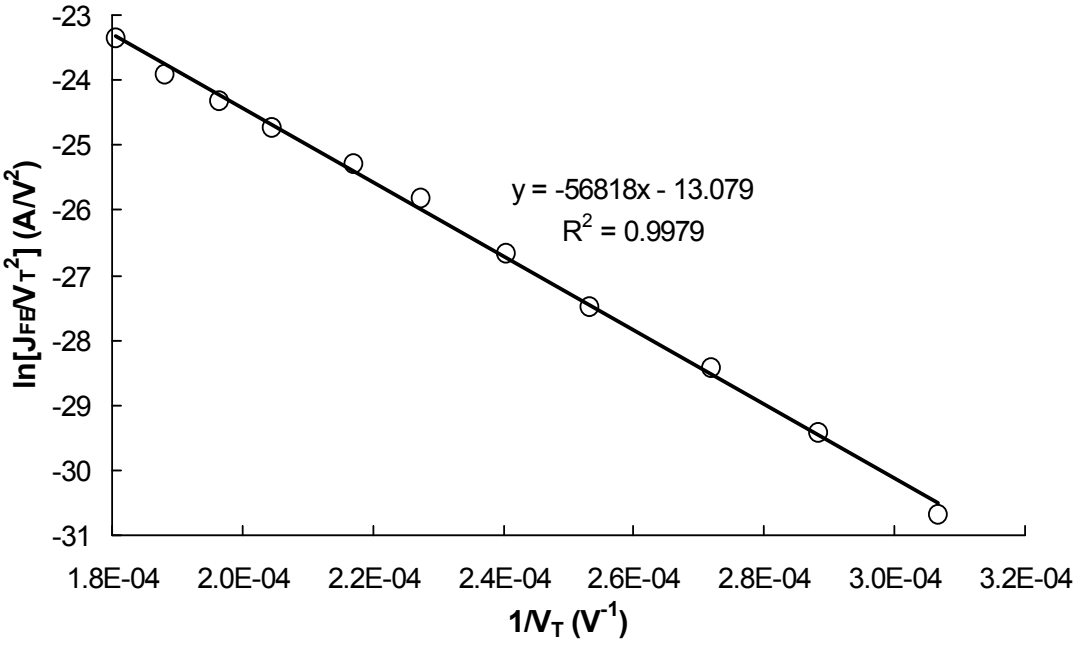

Figure 3.1 Typical F-N plot of a carbon-carbon gridlet.

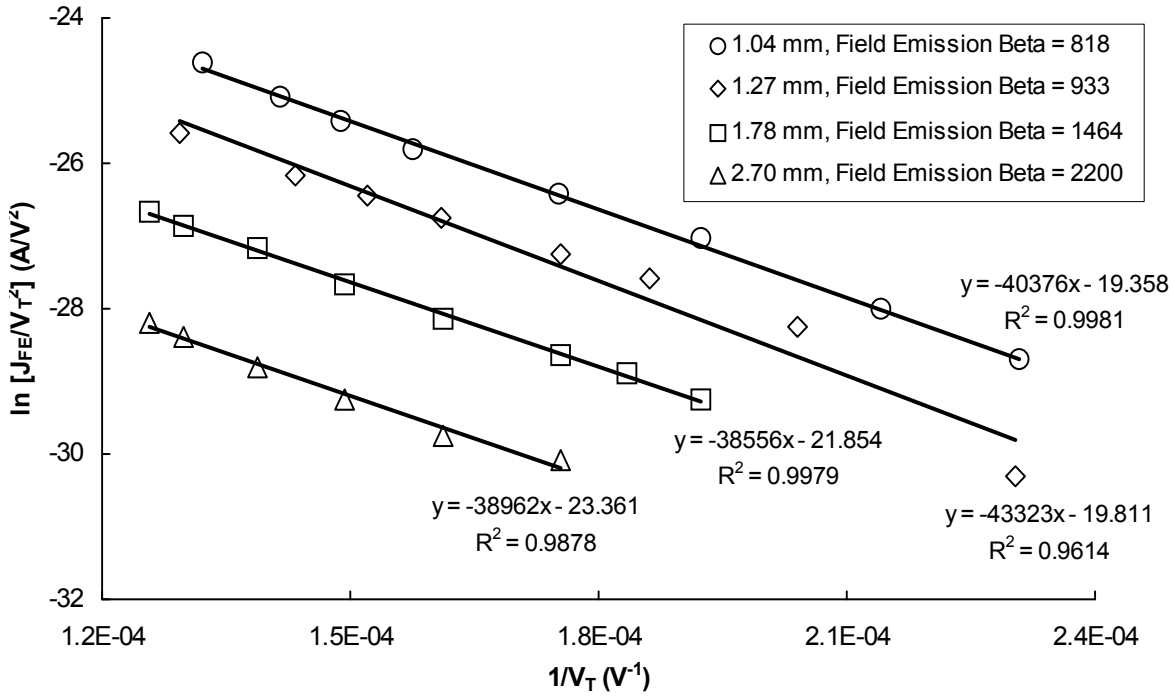

Figure 3.2 Typical F-N plots for various grid gaps. Selected data taken manually to minimize clutter. Note: Minimal conditioning was conducted on the gridlet surface prior to recording the field emission measurements and enhancement factors shown.

Figure 3.3 contains a comparison between the F-N curves taken with and without ion beam extraction for a 1.04 mm grid gap condition using carbon-carbon gridlets. Although similar, the C-C curves obtained with beam extraction were almost always observed to fall just below the curves obtained without beam extraction (when the data without beam extraction was acquired immediately after the data with beam extraction). Some variability in the F-N data was observed, however, and the curve without beam extraction would slowly shift to the left over time for some materials (especially the carbon-based grids). The slope of the curves, and hence the enhancement factors, are similar in Fig. 3.3 indicating that ion extraction and the presence of xenon neutrals and CEX ions only has a minor effect on the localized electric field nearby a protrusion. The measured variability of the F-N data with time suggests that the work function of the accelerator electrode is affected by the presence of xenon on the electrode surface.

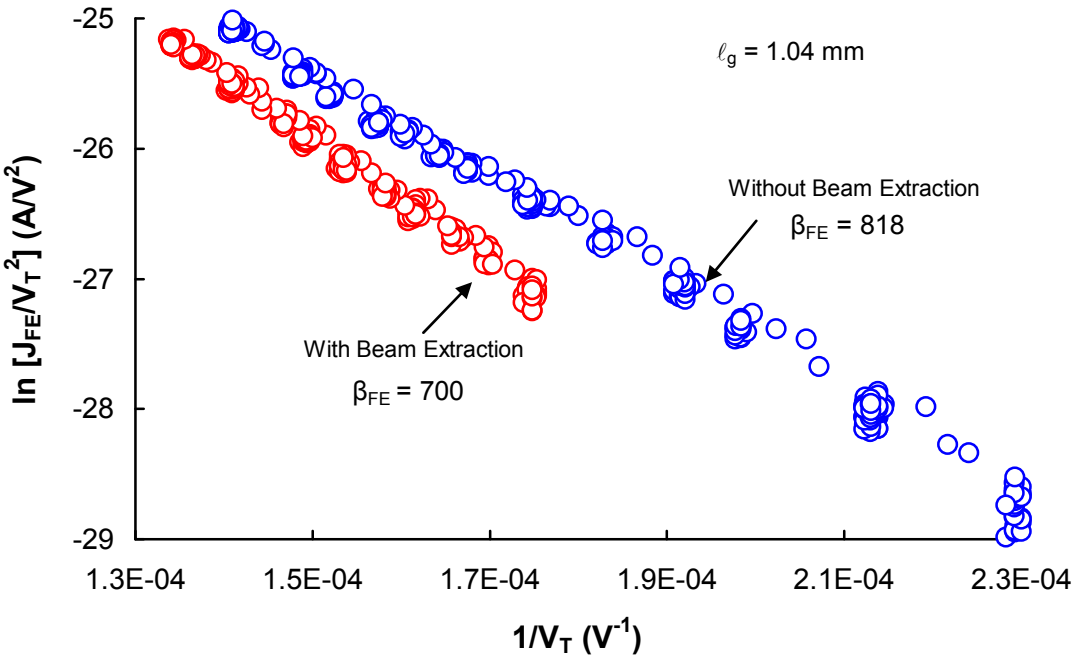

Figure 3.3 Fowler-Nordheim plots with and without ion beam extraction.

There is a perception that arcing is more prevalent when ions are extracted from electrodes. The data in Fig. 3.3 suggest that this perception is not based on arcing resulting from field emission processes. In addition, the effect of CEX ion bombardment of the accel grid does not appear to enhance the amount of field emission current that flows from the accelerator grid to the screen grid for the high electric field operating condition in Fig. 3.3. As suggested above, the presence of xenon gas and CEX ion bombardment during ion beam extraction may serve to suppress the field emission through adsorption of xenon on the accelerator surface and near surface regions and subsequent modification of the surface properties. Experiments conducted with molybdenum to be described later have indicated that upon injection of xenon gas into the ion source, the measured field emission initially increases by 10%, but then drops and levels off at a value that is 10% to 30% below the original field emission value measured prior to gas injection. Similar observations were observed by other researchers when using argon.[49] When the xenon gas flow is stopped the field emission eventually returns to its original value after several tens of minutes.

It is likely that arcing rates are enhanced by out-gassing that may occur nearby small surface protrusions that are being heated by field emission current (as will be shown later in the chapter). In addition, more out-gassing may occur during ion extraction as a grid set is first operated and heated. The effect of out-gassing (caused during ion extraction) on high arcing rates may be mitigated in our experiments due to baking and arc conditioning. Finally, for the tests described herein, the grid spacing is well controlled (within $\pm$2%), but this may not be the case in broad area sources where

interfaces exist between structures with different (1) coefficients of thermal expansion, (2) temperatures, and (3) temperature gradients.

Measurements of field emission made between arc conditioning sequences and typical Fowler-Nordheim plots of these data are shown in Fig. 3.4. As can be seen, a few hundred 1-mC arcs effectively condition the surface while roughly 1500 arcs are required before little to no change is noted from one conditioning sequence to the next.

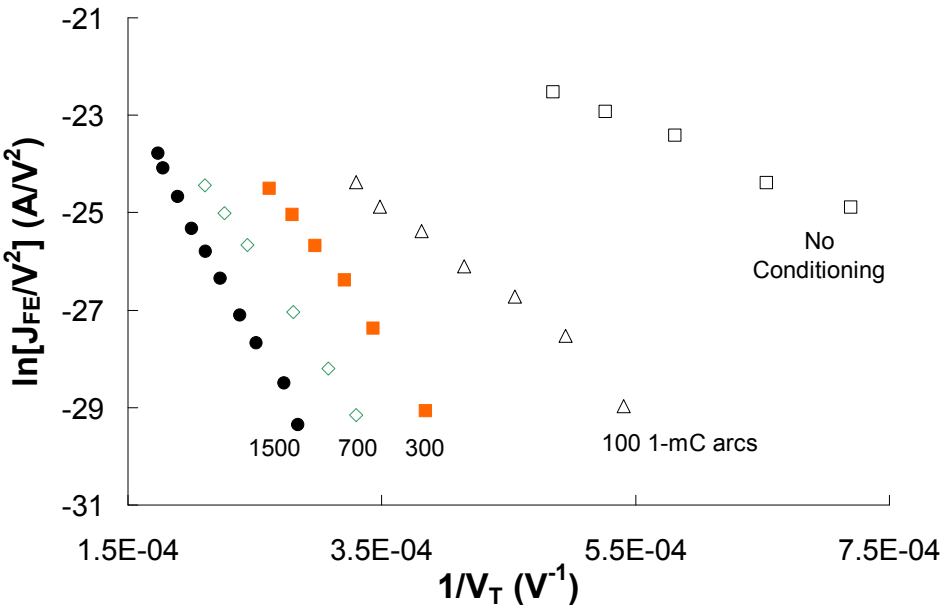

Figure 3.4 Typical Fowler-Nordheim plots of conditioning process.

After investigating the accelerated erosion rate process (described in Chapter 2) using the ffx simulations, it was determined that the two erosion sites on the accelerator gridlet (the barrel region of an aperture and the upstream surface immediately adjacent to an aperture entrance) cannot be eroded to the same amount of in-space operation with the current mask that was used in the accelerated wear facility. We estimate that when the equivalent of ~6 years of in-space erosion has been performed on the barrel region, approximately 48 years of erosion has been performed on the upstream side of the

accelerator grid. Therefore, the grid set exposed in the accelerated erosion facility can be thought of as a worst-case scenario. Figure 3.5 shows a photograph of grid set #1 after being conditioned with the equivalent of 48-yrs of in-space erosion on the upstream surface of each aperture. The high magnification image indicated that a very rough texture was formed around the hole edges consistent with what is observed after long periods of ion bombardment. Measurements of field emission were made between arc conditioning sequences and F-N plots of these data at BOL and with 48-yrs of erosion are shown in Figures 3.6 and 3.7. The BOL and worn gridlets were observed to have lower field emission as the number of conditioning arcs were increased except for the region between 300 and 950 conditioning arcs on the worn gridlet. It is possible that the constant field emission enhancement factor observed between ~500 and 950 arcs in Figure 3.7 could due to a large number of protrusions that were difficult to modify at the 1 mC arc level. An interesting feature of Figure 3.7 is that an increased level of field emission is observed between 300 and 500 arcs possibly due to the formation of new protrusions or ones with sharper edges.

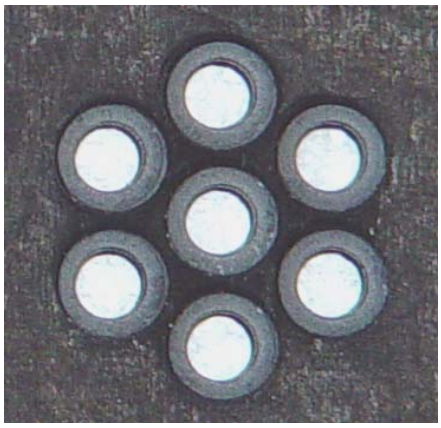

Figure 3.5 **Grid Set #1: NEXIS-style accel grid after testing with the equivalent of 48 years of erosion on the upstream side.**

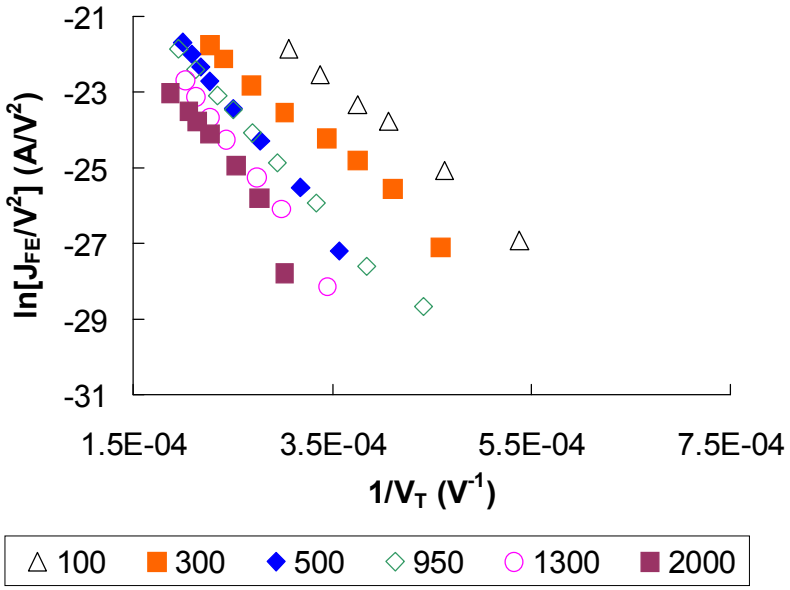

Figure 3.6 **Grid Set #1: BOL. The shift to the left and to higher slope magnitudes corresponds to decreasing field enhancement factors and decreasing effective emission area caused by the application of the 1-mC conditioning arcs. Data with zero arcs was not taken.**

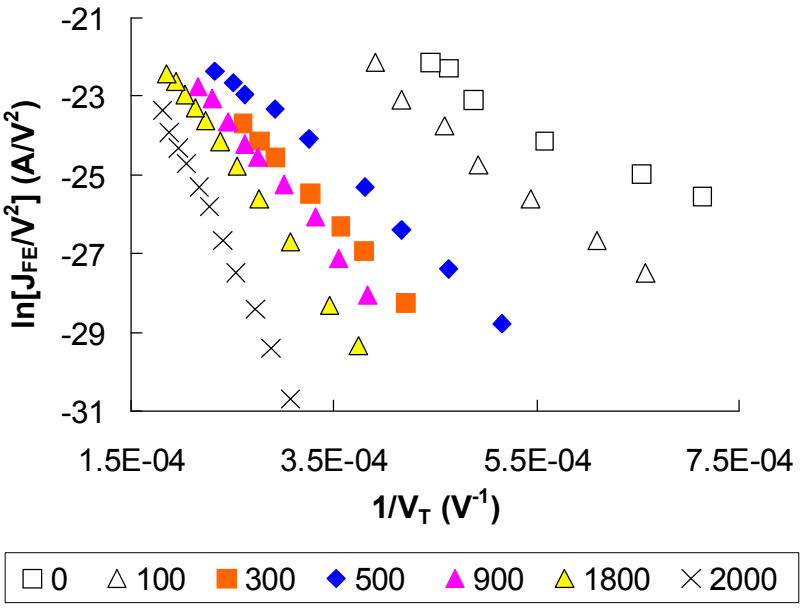

Figure 3.7 **Grid Set #1: 48-yrs equivalent erosion on upstream side and 6-yrs equivalent erosion in the barrel region.**

Recall that the C-C grid set #1 was eroded using the exposure technique conducted in the accelerated wear test facility with the use of masks, while a second grid set designated #2 was eroded using the fast exposure method conducted in the gridlet test facility at high perveance conditions through direct impingement. The direct exposure allowed the upstream surface of the accelerator gridlet to be eroded to the equivalent of 3 and 6 yrs of on-orbit operation in just minutes of testing under high perveance conditions. Figure 3.8 shows a photograph of grid set #2 after the equivalent of 6-yrs of in-space erosion. The difference in color compared to Fig. 3.5 is caused by a camera lighting difference. Measurements of field emission were made between arc conditioning sequences and F-N plots of these data at BOL and with 6-yrs of erosion are shown in Figures 3.9 and 3.10. Figure 3.9 shows how a few hundred 1-mC arcs effectively condition the surface while roughly 1500-1800 arcs are required to condition the BOL grids fully. Improvements in the worn #2 grids are evident in Figure 3.10, but little improvement is observed beyond 900 arcs in terms of lower field emission levels.

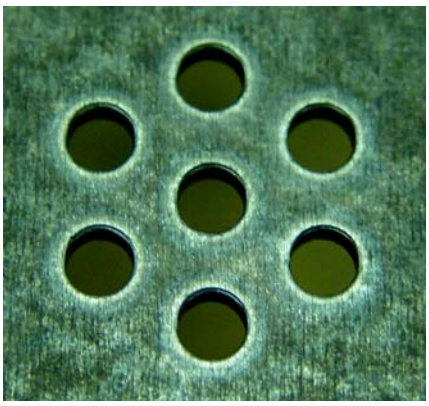

Figure 3.8 Grid Set #2 after testing with equivalent of 6-yrs of on-orbit operation.

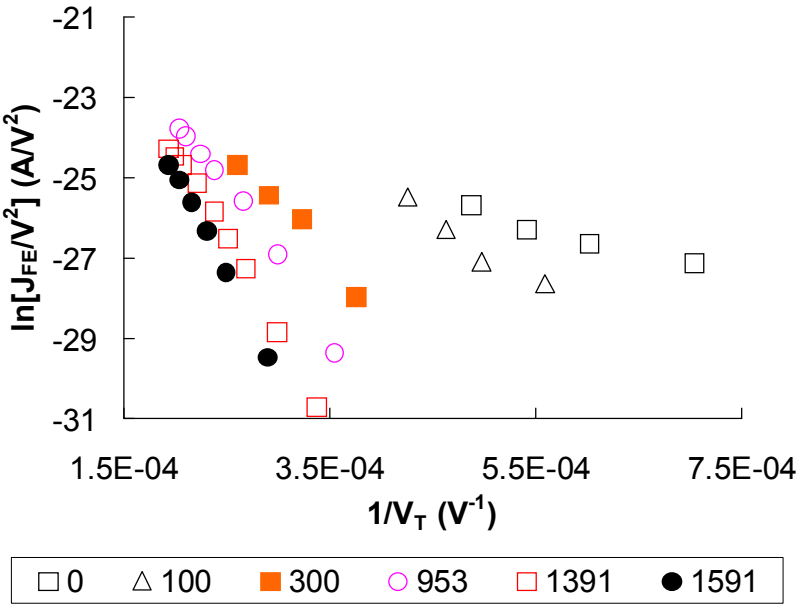

Figure 3.9 **Grid Set #2: BOL. F-N plots for BOL**

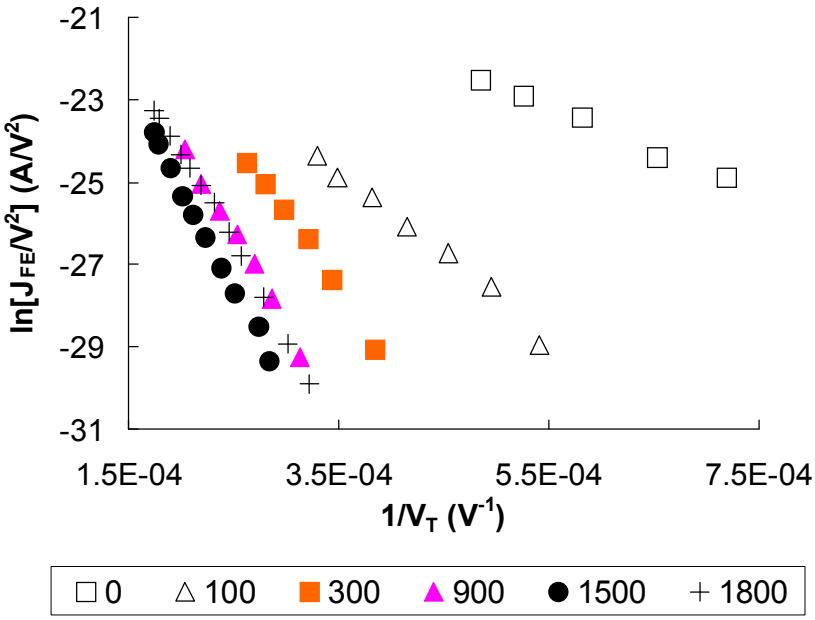

Figure 3.10 **Grid Set #2: 6-yrs equivalent erosion using the fast exposure method.**

Figure 3.11 gives the variation of the localized electric field enhancement factor (using Eq. 2.12 with $\phi = 5$ eV for CC grid material) with the number of conditioning arcs at the 0.5 mm grid spacing for both sets of gridlets. It is assumed that the work function remains constant once the conditioning process begins, although surface adsorbates and contamination could alter the local surface work function at the beginning of testing prior to initiating any conditioning arcs and just after exposure to the atmosphere. As mentioned in Chap. 2, work function changes can result in an apparent change in the enhancement factor (i.e., the sensitivity of the field enhancement factor to the surface work function is 1.5%/%). The number of conditioning arcs is believed to result in a blunting of sharp microscopic surface features and a reduction of the value of β_{FE}. Early on in the testing (with less than 200 conditioning arcs), the sharp drops seen in Figure 3.11 are likely due to relatively large (or very sharp) protrusions on the surface being vaporized by the conditioning arcs. It is noted that enhancement factors in the thousands have been reported for carbon-based electrodes with unconditioned surfaces.[66] While factors of 200-300 are common for fully conditioned molybdenum electrodes.[67] In both studies, the work function was assumed to be that of a pristine and undisturbed surfaces of graphite and molybdenum, respectively. An alternative explanation for the large initial enhancement factors is provided by Collazo[53] who reported an increased emission current, which was attributed to the presence of adsorbates on carbon nano-scale structures where he proposed that adsorbates could introduce a resonant state enhancing the tunneling probability of electron emission. Note that this effect can also be attributed to a reduction of the work function.

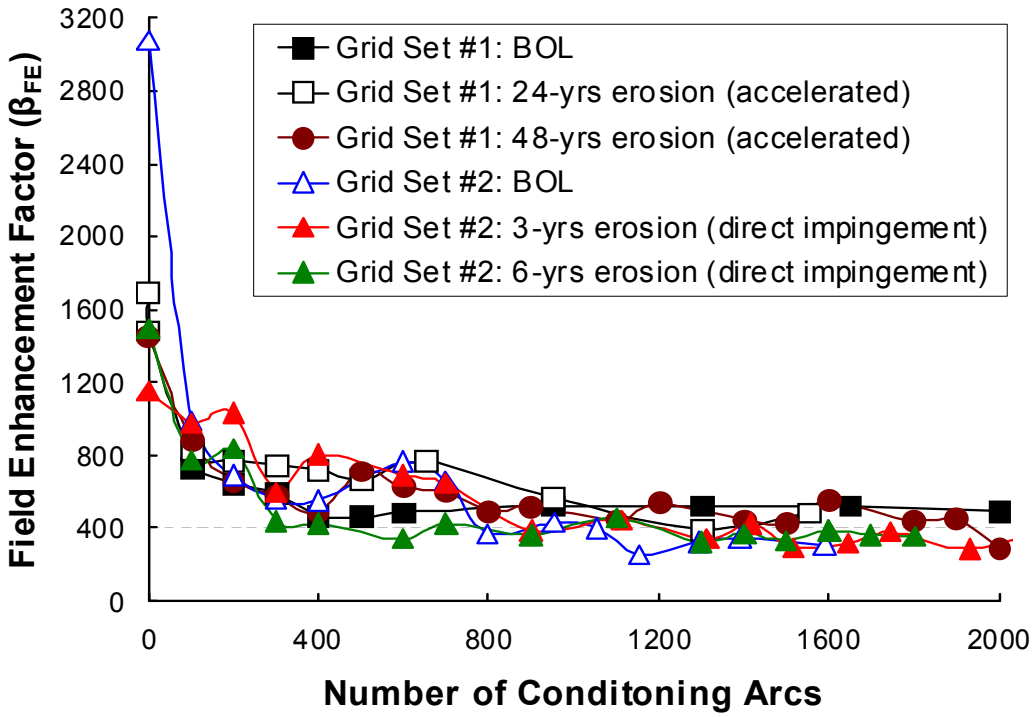

Figure 3.11 Electric field enhancement factor variation with number of conditioning arcs for carbon-carbon gridlets.

After each testing sequence was completed, photographs of the screen and accelerator gridlets were taken to document erosion sites and grid condition. Figure 3.12 shows a photograph of the downstream side of the screen grid and the upstream side of the accelerator gird after testing with the accelerator grid having the equivalent of 24-yrs of on-orbit erosion. The reader can compare Figure 3.12 to the pristine image of the grids shown in Figure 2.5. Notably Figure 3.12 contains signs of arcing present over the entire face of the gridlets, and not just in the active region (near the apertures) where ions were being extracted.

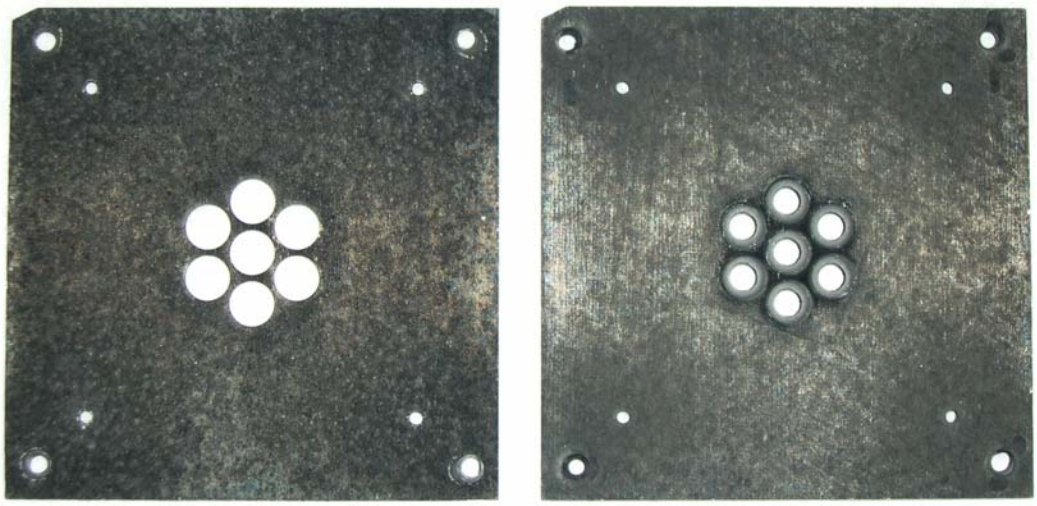

a) Screen gridlet b) Accelerator gridlet

Figure 3.12 NEXIS-style CC gridlets after testing with the equivalent of 24-yrs of on-orbit operation on the upstream surface and 6-yrs in the barrel region.

High magnification photographs are shown in Fig. 3.13 of both the downstream side of the screen gridlet and the upstream side of the accelerator gridlet after arc conditioning the gridlets. Craters on the downstream side of the screen grid are likely due to vaporization caused by the high arc energy deposition rates and the low thermal diffusivity of CC material. In contrast, the upstream side of the accelerator grid was observed to have much smaller diameter craters. One possible mechanism leading to electrical breakdown involves field emission from a protrusion on the accelerator grid that proceeds (such as the one shown in Figure 3.14) as a beam to the screen gridlet where it locally heats and possibly vaporizes screen gridlet material or releases adsorbed gases. Some of the evolving vapor becomes ionized by the electron beam. Any ions formed from the gases evolving from the gridlets that strike the accelerator can produce secondary electrons. In this way, the presence of the ions intensifies the electron emission

still more, eventually causing breakdown of the gap. To investigate this theory further, upon fully conditioning each grid material, the ground screen was removed to allow viewing of a portion of the grid gap region. Interestingly, not only did all the arcs occur between the grids but about a quarter of the arcs were preceded by a slight glowing of a small area of the screen grid – presumably due to electrons streaming from an adjacent, localized region on the negatively-biased accelerator grid. Only a portion of the grid gap was visible through the view port, so it is conceivable that other regions of the screen grid had glowing dots as well. It is also noted that the glowing area of the screen grid did not usually correspond to the location where an arc was observed to occur. The glowing regions on the screen electrode occurred across the entire surface and often tens of seconds passed before an arc occurred.

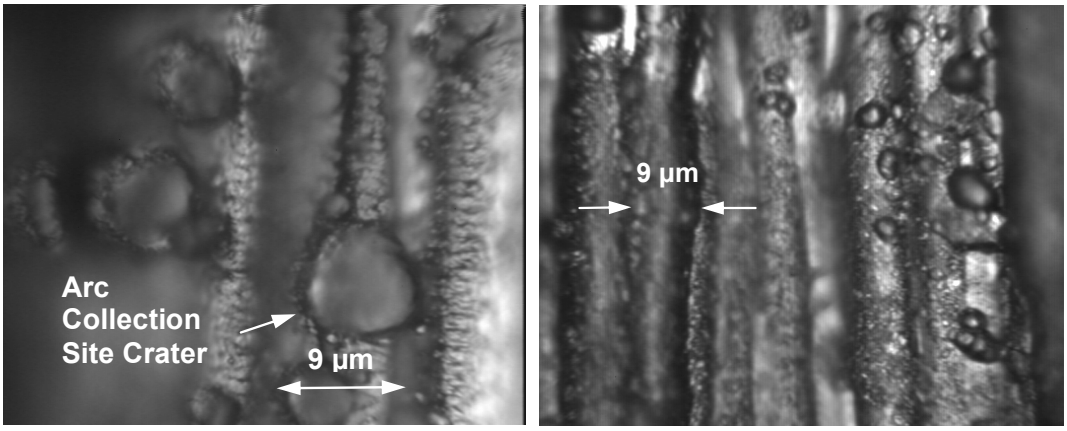

(a) (b)

Figure 3.13 Microscopic photos of (a) edge of center hole on downstream side of screen grid and (b) just beyond the active area on the upstream side of the accelerator grid. Each fiber is ~9 µm in diameter.

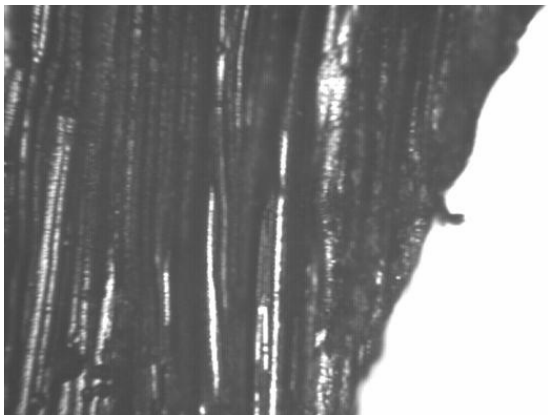

Figure 3.14 Microscopic photograph of a protrusion upstream side of the accelerator gridlet aperture. Each fiber is ~9μm in diameter.

Numerical simulations were used to determine if the arc site locations correspond to regions where the highest electric field exists. Figure 2.22 (shown here again as Figure 3.15 for convenience) is an electric field plot at a beamlet current of 1 mA/hole for the BOL NEXIS geometry using ffx. As expected, the highest electric field conditions on the negatively biased accelerator surface are at the upstream entrance of an aperture, and, although arc initiation sites were observed at the edges of the accelerator apertures, many more arc sites were observed on the accelerator grid webbing and in the regions of the electrode where no apertures existed. The high electric fields near the downstream side of the screen grid holes, as determined by the numerical simulations, correspond to where the largest craters are observed in Fig. 3.13, but it is noted that a portion of the arc current could be directed through a screen grid hole and into the discharge chamber plasma.

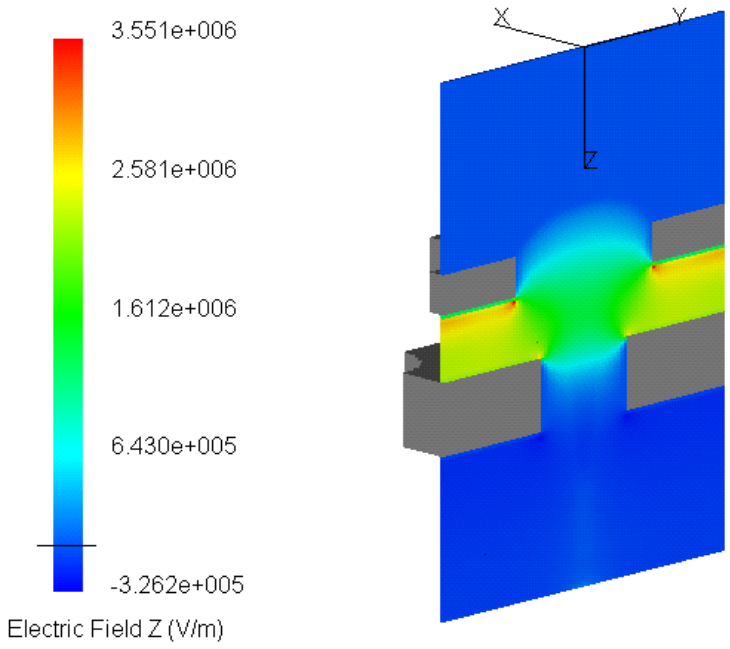

Figure 3.15 Electric field with ion extraction from ffx simulation results for NEXIS geometry at BOL.

As mentioned above, after eroding a surface to simulate operation in space, a 3-hr run was initially conducted (at the lowest possible charge transfer value of 0.01 mC) prior to beginning the arc conditioning process. Two instances of erratic accelerator current were recorded during our tests: 1) during the first 3-hr run after the upstream side of the accelerator grid was eroded to 24-yrs of on-orbit operation (3-yrs in the barrel region) and 2) during the first 3-hr run after the accelerator grid was eroded to 48-yrs of on-orbit operation (6-yrs in barrel region). No erratic accelerator current behavior was observed after performing the direct impingement tests. Figure 3.16 shows the erratic behavior during the first 3-hr run for grid set #1 after being eroded to the equivalent of 48-yrs and prior to being conditioned.

Initially the accelerator grid current was relatively high or noted to be gradually increasing at a fixed beamlet current. The spikes in the accelerator grid current did not

correlate with arc events or result in an arc in about half of the spike events. Similar anomalous accelerator current behavior was observed in the NEXIS 2000-hr wear test just after a cryopump regeneration.[68]

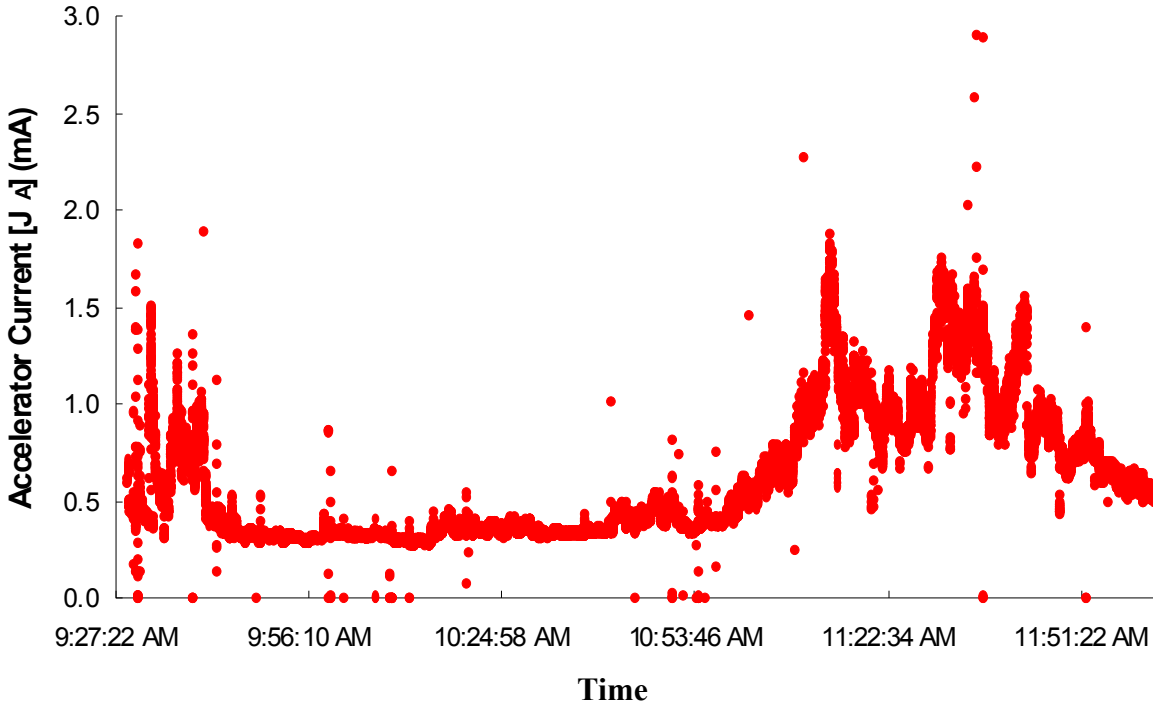

Figure 3.16 Accelerator grid current during the first 3-hour test after eroding the accelerator grid upstream surface to an equivalent of 48 years. Note the presence of accelerator current noise. Upon initiation of the first set of 100 arcs at 1-mC, the accelerator current spikes were eliminated and did not return even at higher electric fields values.

From Figure 3.11, one can see that the field emission enhancement factor was very high prior to initiating any 1-mC conditioning arcs implying that very high local electric fields are present on the grid surface at this time. Upon initiating the first 100 conditioning arcs, the field emission enhancement factor dropped substantially. In addition, the accelerator grid current was observed to be steady with very little noise ($<\pm 2\%$) after 100 conditioning arcs had been applied.

Although the gridlets had been under vacuum (<$1x10^{-6}$ Torr) for 11 hours prior to the data collection documented in Fig. 3.16, testing began after just one hour of applying filament heater power. The experimental results are insufficient to determine if surface contamination is being removed by the 1-mC conditioning arcs or if protrusion blunting is occurring as well. A related explanation for the anomalous accelerator gridlet current could be due to the discharge filament and discharge plasma initially heating the screen gridlet, causing contaminants from the hotter screen gridlet surface to re-adsorb on the initially cooler accelerator grid. Figure 3.17 shows how the enhancement factor varies depending on when and how the grids are heated and de-gassed. Once the discharge and neutralizer filaments have been on for 1 hr, the enhancement factor can increase by 60% from the initial measurement taken prior to heating the discharge chamber and grids. After extracting a beam and running the ion source for 1 hr, the enhancement factor begins to level off to a value just below the initial value measured. The enhancement factor remains at or near this value as long as the grids remain under vacuum (except when conditioning arcs are applied). One possible explanation of why the enhancement factor increases as the grids are first warmed up is a temporary reduction in the work function of the surface as it is being wetted by out-gassing products (the sensitivity of field enhancement, β_{FE}, to a change in work function is 1.5 %/%). Although a work function change is a possibility, the measurements suggest a work function decrease of 40% would have had to occur, which is quite large.

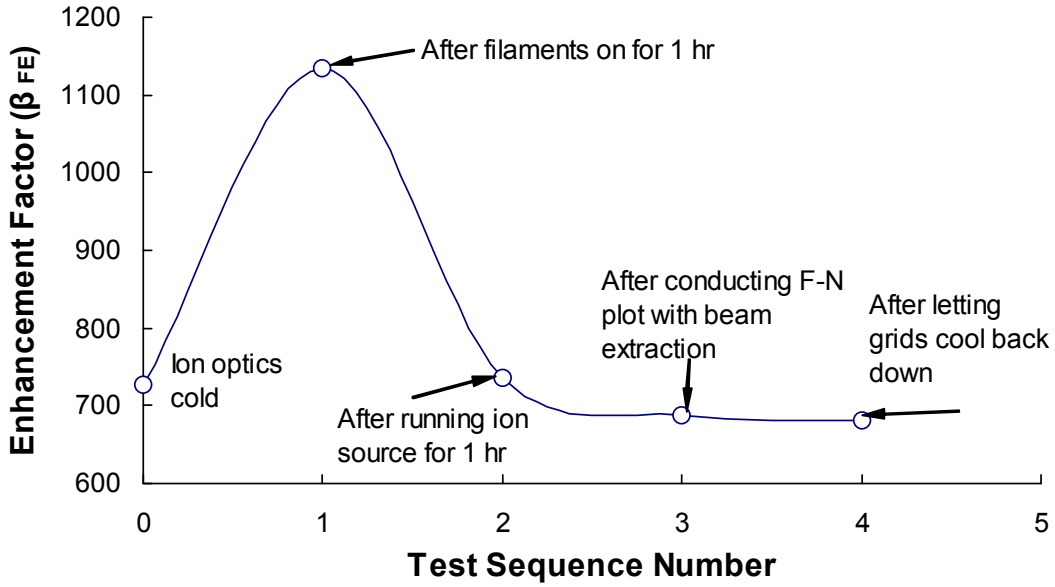

Figure 3.17 Typical enhancement factor variation during ion source operational steps without beam extraction.

3.1.2 Applied Electric Field Evaluation

Experiments were conducted to determine how the breakdown electric field and the enhancement factor vary with grid gap and grid surface condition. The charge transfer per arc during these tests was limited to 0.01 mC. Although other arcing studies of ion optics materials have defined the electric field breakdown point more conservatively by the onset of a certain field emission current level or after a single arc was observed,[15] it was decided herein to utilize the less conservative continuous arcing field value to avoid outlier bias of the results. Researchers[58] have indicated that the initial breakdown between flat electrodes at low voltages can usually be attributed to an insulating or foreign particle on the surface and therefore not truly reprehensive of the actual material properties.

Electric field breakdown data were first measured with beam extraction at a moderate beamlet current. Then the xenon flow was turned off along with both the

discharge and neutralizer filaments, and once the vacuum pressure dropped to ~$1x10^{-6}$ Torr, the electrical breakdown point was re-measured without beam extraction.

Following each conditioning process, electric field breakdown tests were conducted to record the variation in the breakdown voltage as a function of beamlet current, number of conditioning arcs, and grid spacing. Figure 3.18 contains a plot that compares field breakdown characteristics with and without beam extraction. It should be noted that very similar results were obtained for 1-mC arcs, but approximately an order of magnitude fewer conditioning arcs were required at the 1-mC level to achieve the same results. Differences in the two methods of obtaining the breakdown value are within 5% for the carbon-based materials and within 10% for molybdenum. It is noted that the insensitivity of the electric field breakdown point to whether ions are extracted or not lends validity to tests performed without beam extraction.

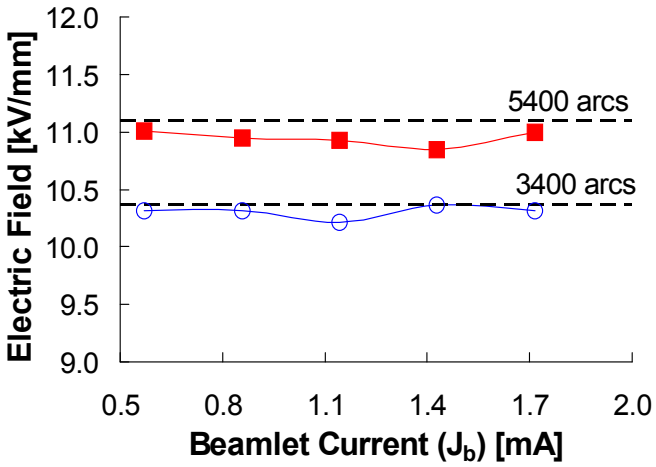

Figure 3.18 Breakdown field comparison with and without beam extraction after 3400 and 5400, 0.25-mC conditioning arcs. Note: at 1-mC the values were achieved with an order of magnitude fewer arcs. Dotted line represents results without beam extraction

Numerical simulations using the ffx code were conducted to study the effect of increasing the electric field on the relative erosion rate of the upstream surface of the

accelerator electrode. As the net voltage is increased, the energy of intra-electrode CEX ions increases causing an increase in the erosion rate of the upstream side and aperture barrel region of the accelerator grid. Increasing the electric field from 2.2 kV/mm to 10 kV/mm resulted in a proportional increase of the accelerator upstream erosion rate by a factor of five during the first 20,000 hours of operation. It is noted that the erosion rate of the upstream surface of the accelerator grid is not the limiting factor in accelerator grid lifetime for the NEXIS class thruster, and a 5x increase in this rate does not affect the throughput capability of the ion optics system in terms of erosion by sputtering.

Figures 3.19 and 3.20 summarize the effect that the number of 1-mC conditioning arcs has on the applied electric field breakdown strength for grid set #1, which used the accelerated erosion method, and #2, which used the direct impingement erosion method. One can see that the curve for grid set #1 begins to level off after 400 conditioning arcs have been initiated between the grids. Grid set #2 (regardless of whether it was sputtered eroded or not) takes many more arcs to reach the 10-11 kV/mm mark than grid set #1. This may be due to grid set #2 being kept in a plastic bag for approximately three weeks after undergoing the laser beam soot cleaning process discussed earlier. This exposure to the atmosphere could have built up a relatively large amount of adsorbates on the grid surface requiring many more conditioning arcs to achieve operation at the 11 kV/mm level. General guidelines from ion implanter and neutral beam injector technology indicate that arcing will occur if the electric field is increased above ~10 kV/mm. This result was observed once the CC gridlets have been conditioned properly. The maximum breakdown field recorded for CC gridlets used in this study was 11.4 kV/mm.

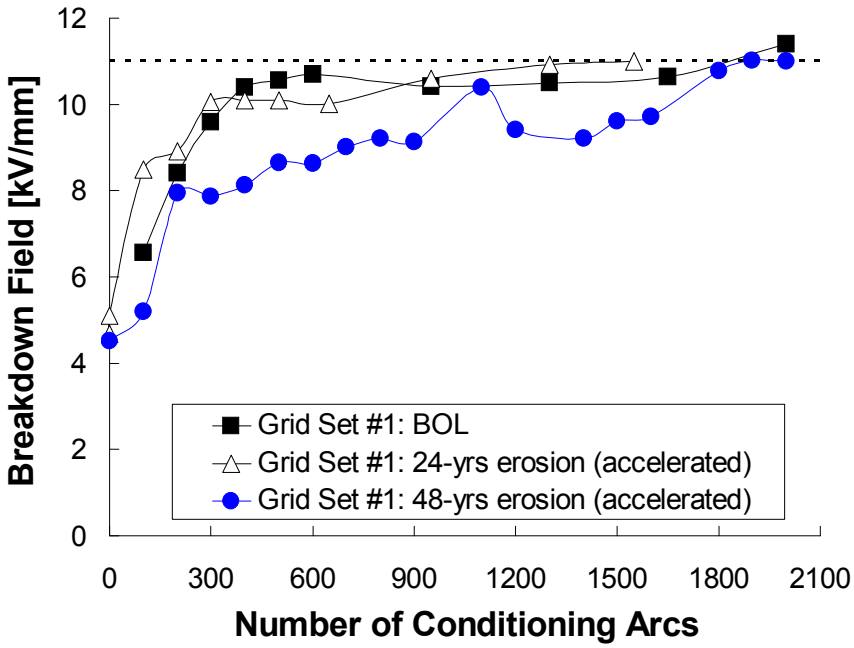

Figure 3.19 **Breakdown field dependency on the number of conditioning arcs before and after accelerated wear processing.**

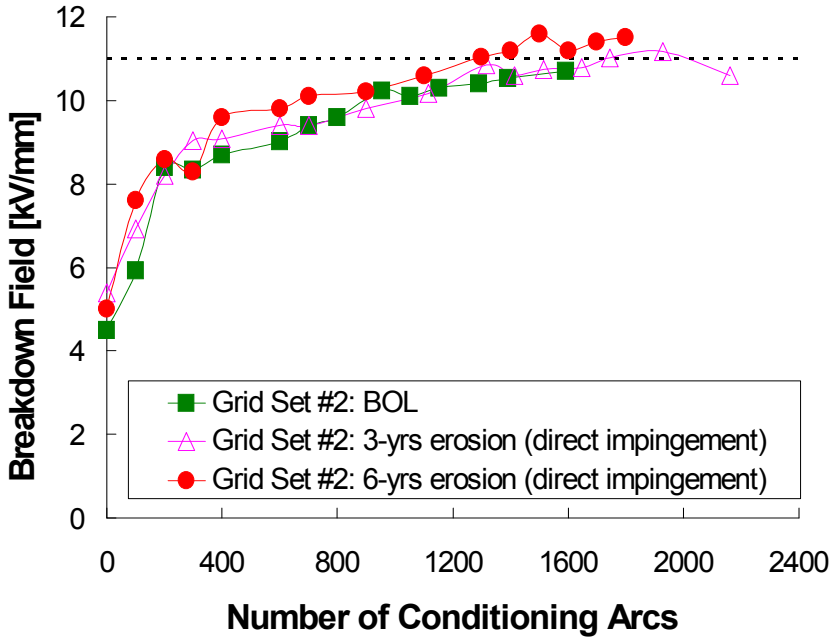

Figure 3.20 **Breakdown field dependency on the number of conditioning arcs before and after wear from direct impingement processing.**

An interesting observation from the plots in Figures 3.19 and 3.20 is the fact that despite the significant erosion performed on the upstream side of the accelerator gridlet, with proper conditioning of the grid surface, the BOL maximum breakdown field can still be achieved. It is noted that the 48-yr erosion data shows quite a bit more scatter than the data for the BOL and 24-yr erosion curves indicating that the significant amount of erosion around the upstream side of the accelerator grid is beginning to have a greater effect on the breakdown field for a given number of conditioning arcs. Although, the sputter erosion on the upstream surface of the accelerator gridlet is much more severe than what is expected to occur in space, we have found that the resulting standoff voltages (and other arcing related behavior) are identical to the BOL grid surface once the accelerator gridlet surface has been conditioned with several hundred 1-mC arcs.

The maximum applied electric fields are plotted in Fig. 3.21 as a function of grid spacing for the CC material. Using the curve-fit equation, one obtains a maximum electric field of 11.85 kV/mm for a grid gap of 0.5 mm (4% higher than measured) and ~5 kV/mm (through extrapolation to 2.36 mm spacing) for the NEXIS nominal grid gap. It should be noted that using the enhanced electric field of 5400 kV/mm for CC one obtains a predicted maximum electric field of 4.5 kV/mm (+/- 10%) for the NEXIS nominal grid gap as will be shown in the next section.

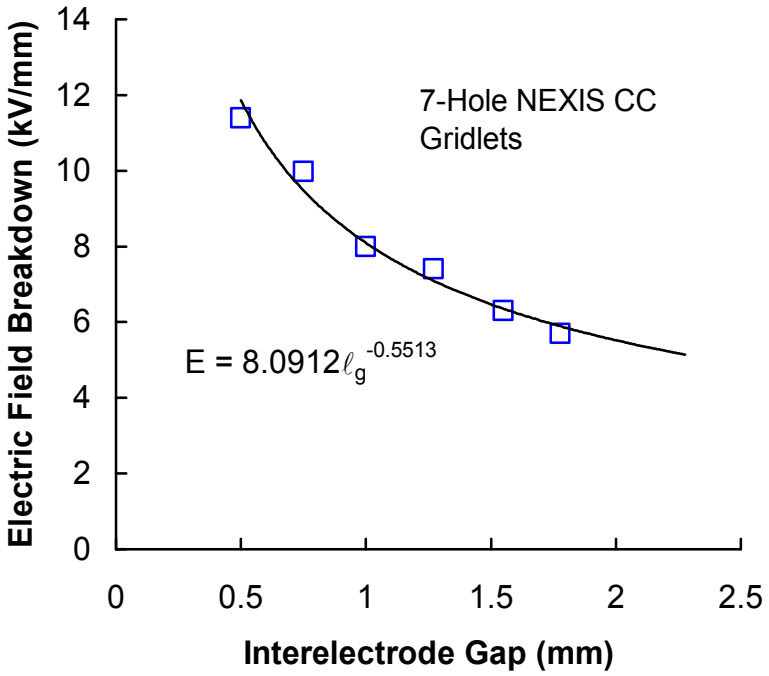

Figure 3.21 Grid Set #1: Maximum electric field for partially to fully conditioned CC gridlets at various grid gaps.

Figure 3.22 contains field emission current data collected at a grid spacing of 0.5 mm for the carbon-carbon material. The unconditioned cases correspond to the gridlet surface prior to initiating any conditioning arcs at BOL or after the grids were eroded in either the accelerated wear testing facility or through the direct impingement method. Fully conditioned corresponds to not only the minimum field emission state of the surface but also to the case where the maximum voltage standoff was achieved. As indicated above, the maximum breakdown field for both grid set #1 and #2 is ~11 kV/mm. From Figure 3.22, an applied electric field of 11 kV/mm would be at a relatively high level of field emission. If no (or very little) field emission was desired, then the maximum breakdown field for a 0.5 mm grid gap would be approximately 6.5 kV/mm. As Figs. 3.19, 3.20 and 3.22 clearly indicate, the onset of field emission may begin at a

certain electric field value, but the ultimate breakdown field (defined as just prior to continuous arcing) can be significantly higher.

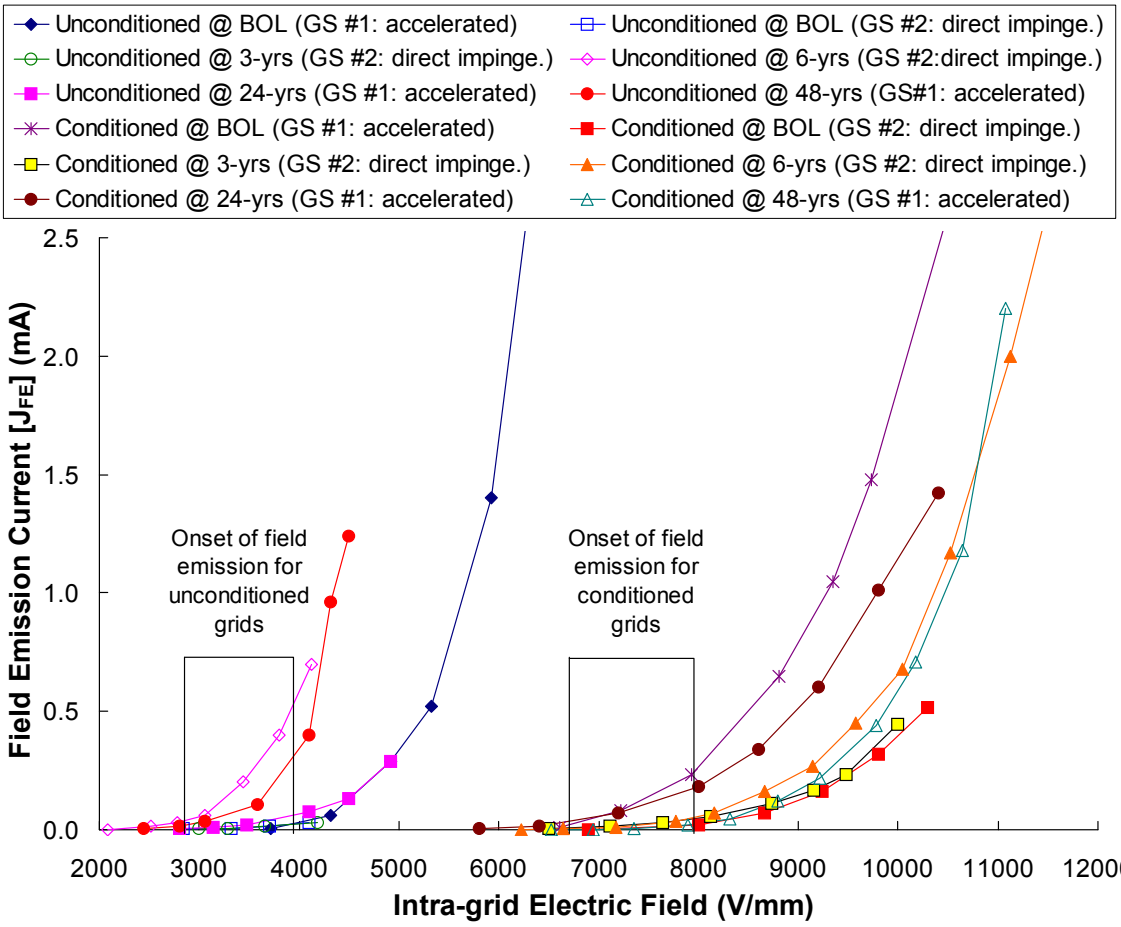

Figure 3.22 Threshold electric field for field emission. Note: Unconditioned = prior to initiation of any 1-mC arcs, Conditioned = once the maximum voltage standoff is reached with a fully conditioned grid surface, GS = Grid Set, accelerated = exposure in the accelerated wear test facility, direct impinge = exposure using the direct impingement method. Onset of field emission = 0.01 mA.

Most ion thrusters typically operate at conservative electric fields of 2-3 kV/mm due to electrical breakdown concerns. Figure 3.22 shows that through proper conditioning of small ion optics systems using controlled arcs at a level of ~1mC/arc, future ion thrusters could potentially be operated at much higher electric fields and

correspondingly higher thrust densities. As pointed out in Chapter 1, as the applied electric field between the grids is doubled the thrust density will quadruple.

3.1.3 Enhanced Electric Field Breakdown

The electric field enhancement factors are plotted in Fig. 3.23 as a function of grid spacing for the CC material. The trend of increasing enhancement factor with grid spacing follows the trend observed by others[31,36,49,62], however, one important difference is that most published work shows the enhancement factor leveling off between 1 and 2 mm grid spacing. This difference could be due to the fact that most published work has focused on solid flat and solid spherical electrodes whereas we are using flat electrodes with holes. Due to the 8 kV voltage limitation of the arc suppression switch, the grids could not be re-conditioned at the largest grid gap conditions. The continuous increase of the enhancement factor with grid spacing shown in Fig. 3.23 may also be due in part to enhancement of the electric field at small protrusions on the surface of the accelerator grid that is further enhanced by the presence of geometrical features. Another possibility is that localized areas with different work functions exist, but this is considered unlikely because work function effects are not expected to be gap dependent. The variation of the enhancement factor with grid gap can be interpreted in terms of the combined effects of an enhancement, β_{FE1}, due to microscopic protrusions on the accel grid, and a local enhancement, β_{FE2}, associated with macroscopic changes in the electric field distribution at larger gap spacing due to fringing around hole and edge features, where the overall enhancement is the product of these factors.[36] Thus at larger grid gaps, fringing effects may become more significant at influencing the overall enhancement factor while the microstructure at the accelerator grid surface most likely remains unchanged. Analysis

reported by Alpert[36] using a model of a pair of semi-infinite slab electrodes with rounded corners indicates that when the gap spacing becomes large compared to the radius of curvature at the edges of the electrodes, the enhancement factor β_{FE2} may become appreciable. The fact that the gridlets used in this study did not have rounded corners could also partially explain the lack of a saturation point in the enhancement factor at the largest grid gaps. It is noted that arc marks were also observed beyond the edges of the 7.5-cm x 7.5-cm gridlet area on the grid assembly mount. When the local curvature differs from the main surface area (such as at the edges), local variations in the electric field and compression of the equipotentials nearby can occur. Byers[16] experimentally showed that rounded edges when compared to square edges do provide larger breakdown field margins between electrodes containing holes.

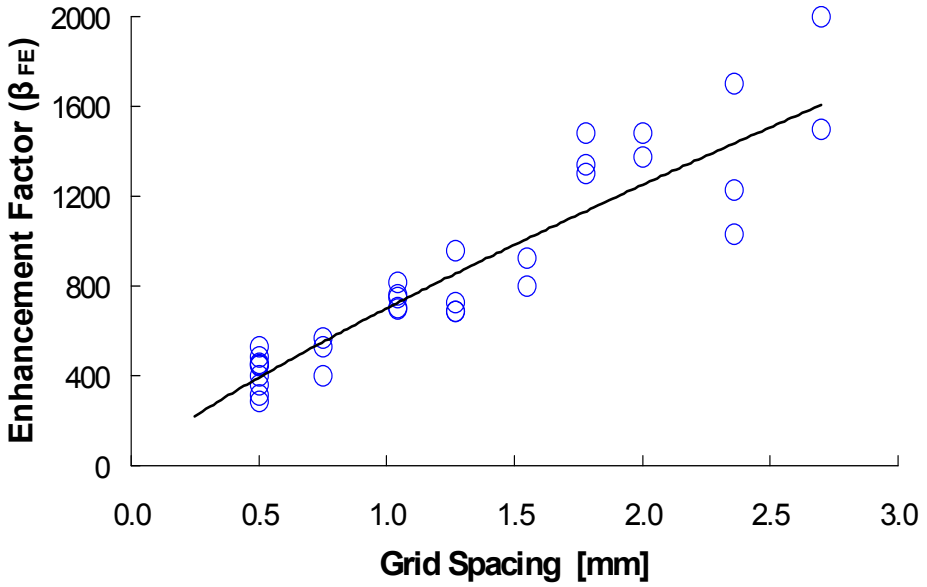

Figure 3.23 Plot of field enhancement factor against grid spacing of NEXIS-style CC gridlets.

Due to arc suppression equipment constraints, plots such as the one shown in Fig. 3.23 could not be made for every grid spacing tested. The maximum voltage of the

arc suppression power supply is 8 kV, which is less than the voltage required to cause breakdown for grid spacing beyond 1.04 mm after just a few hundred conditioning arcs are applied. Once the grids were fully conditioned at the 0.5 mm grid spacing, the grid assembly was removed from the chamber and the grid gap was manually changed using shims of known thickness. Once the gap was reset, the assembly was re-attached to the ion source inside the vacuum chamber and left at vacuum for 6 hours. The discharge and neutralizer filaments were also on for several hours to heat the grids and assist with out-gassing.

The enhanced electrical-breakdown field (or microscopic field) at the accelerator grid surface is determined by multiplying the enhancement factor by the applied electric field (i.e., $E_m = \beta_{FE} V_T / \ell_g$). Figure 3.24 contains a plot of the enhanced electric field versus electrode separation. Although there is considerable scatter in the data, Fig. 3.24 suggests that the enhanced electric field is relatively independent of the grid gap as expected from the literature.[36,62,69] The enhanced electric field value at breakdown will vary from one material to another, and can be dependent upon surface treatment. Similar electric field breakdown work conducted on other types of electrode materials has shown a similar constant enhanced electric field breakdown trend over many orders of magnitude in gap spacing.[36,62,69]

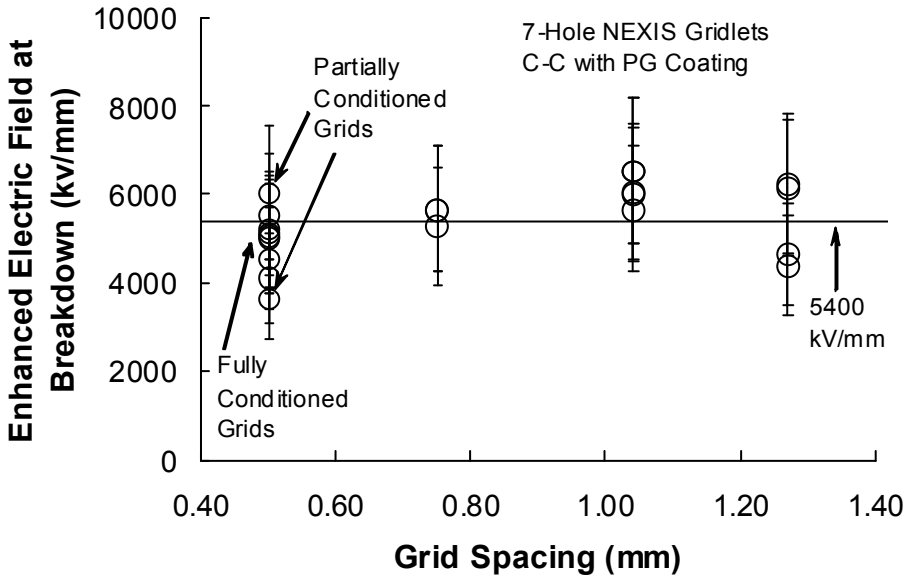

Figure 3.24 Enhanced breakdown field versus gap spacing. For each point, the breakdown field is the product of the breakdown voltage and the enhancement factor, determined from Fig. 3.23.

An important consequence of Fig. 3.24 is that the value of the breakdown voltage is directly related to, and predictable from, the observed characteristics of the pre-discharge field emission currents and knowledge of the material dependent enhanced electric field breakdown value. The average value of the enhanced electric field at breakdown from Figure 3.24 (shown by the black line across the plot) is 5400 kV/mm. This enhanced electric field value lies within values measured for a variety of electrode materials, which range from 4,000 to 11,000 kV/mm for fully conditioned electrodes.[70] Dividing this value by the measured enhancement factor at a given grid gap will result in an approximation of the maximum applied electric field possible with fully conditioned ion optics. For example, using the average enhanced electric field of 5400 kV/mm and dividing by the average enhancement factor of 420 for the 0.5 mm grid gap, one gets a maximum applied electric field of 12.8 kV/mm for CC gridlet material. This prediction of the electric field is within 10% of the maximum electric field at breakdown measured

for fully conditioned grids at this grid gap (see Fig. 3.19 and 3.20). Due to the scatter in Fig. 3.23 at the highest grid gaps it is difficult to estimate what the breakdown field would be at the nominal NEXIS thruster grid gap of 2.36 mm with a high level of confidence. But an approximation of the breakdown field can be made using the 5400 kV/mm enhanced electric field measurement (shown in Fig. 3.24) and the enhancement factor of 1200 measured at a grid gap of 2.36 mm (shown in Fig. 3.23) is estimated to be 4.5 kV/mm for fully conditioned grids. It is noted that our total voltage limitation of 8 kV resulted in a maximum applied electric field of 3.3 kV/mm at this grid gap and no indication of arcing was observed. Interestingly, other research has shown that the enhanced electric field strength is nearly constant regardless of the electrode area.[71]

3.1.4 Weibull Statistical Analysis

As discussed in section 2.7, Weibull statistical analysis was used to analyze the arc period probability distribution of a gridlet set when operated at given electric field and intra-grid spacing while extracting ion beamlets. Our approach was to characterize the electrical breakdown behavior (i.e., record the time of each arc event over a preset period of time) using the lowest arc charge transfer setting of our power supply system (~0.01 mC) after conditioning the accelerator gridlet with a number of arcs at a higher arc charge transfer setting that was set using a capacitor connected between the screen and accelerator gridlets. The time of an arc event was monitored using a time stamp resolution of 0.5 sec, and consequently, the minimum resolution of an arc period measurement was ~1 sec. For analysis purposes, the arc events that occurred in a particular test were ranked from the shortest period between two arcs to the longest period between two arcs, and then plotted on Weibull probability graph paper.

The arc period was observed to increase significantly as the grids were conditioned. Figure 3.25 contains comparisons of Weibull plots that demonstrate this observation. The beamlet current was set at 1.2 mA for these tests. The Weibull shape parameter for all the measurements on CC material was approximately 0.70, but the characteristic arc period changed by nearly two orders of magnitude due to conditioning of the gridlets and operation at higher values of electric field.

Although some of the Weibull curves fall on a straight line (which implies that the Weibull distribution can be used to describe the probability distribution of arc period accurately), some data sets do not fall on straight lines. Possible reasons for this could be changing grid temperature, grid conditioning, or erosion; an incorrect time origin; or effects due to arcing at 0.01 mC. Considering the last possibility, it could be that the data need to be split up into several smaller time intervals and then plotted with more than one curve especially during early testing.

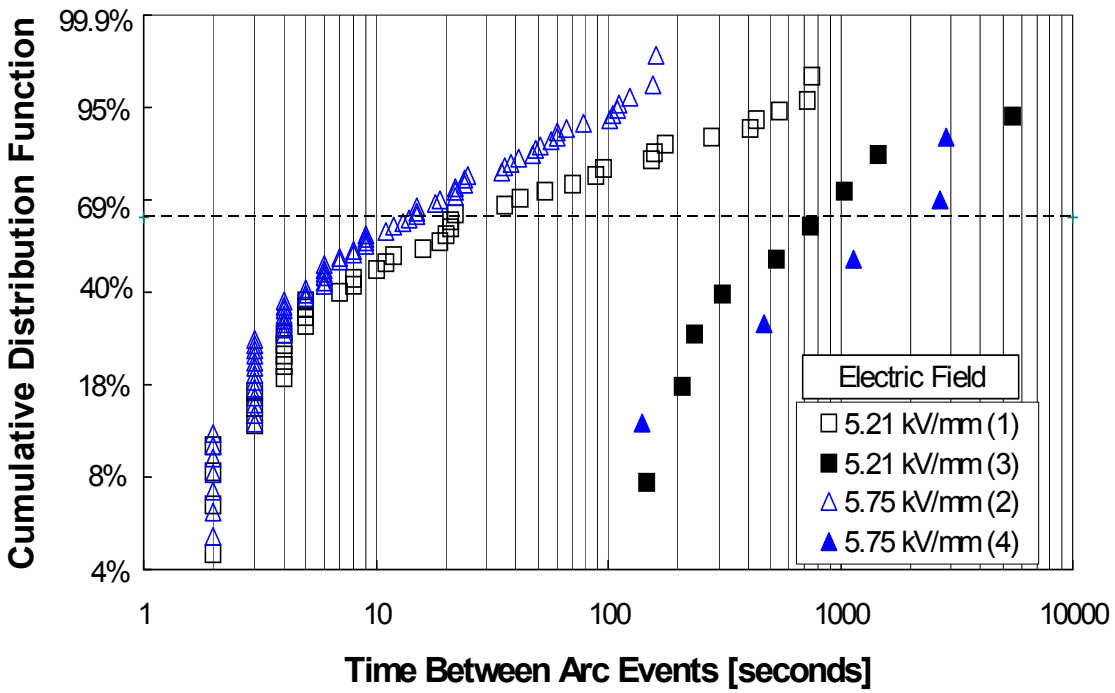

Figure 3.25 **Weibull plots for 5.21 and 5.75 kV/mm showing effect of conditioning at 10 μC per arc. The number in parentheses indicates the test sequence. Note that 5.75 kV/mm (2) contains fewer arcs than 5.21 kV/mm (3). This is due to test case 5.75 kV/mm (2) being performed after raising the electric field above 6.5 kV/mm for a short time to determine if the grids would begin to arc continuously. Note: each data curve was taken over a 3-hr run.**

Figures 3.26 shows the effect of increasing the number of 0.25 mC conditioning arcs on the arc period for a grid gap of 0.5 mm. Each data set corresponds to the ion source being operated for 3-hrs. The general trend is that the mean time between arcs increased as more conditioning arcs were initiated. The non-linear Weibull plot behavior at short arc periods did not occur as often during tests conducted later in the test matrix. Figure 3.27 shows the effect of increasing the charge transfer to 1.0 mC. As can be seen, for the same order of magnitude increase in the mean time between arcs, an order of magnitude fewer arcs are needed for 1 mC conditioning compared to 0.25 mC conditioning.

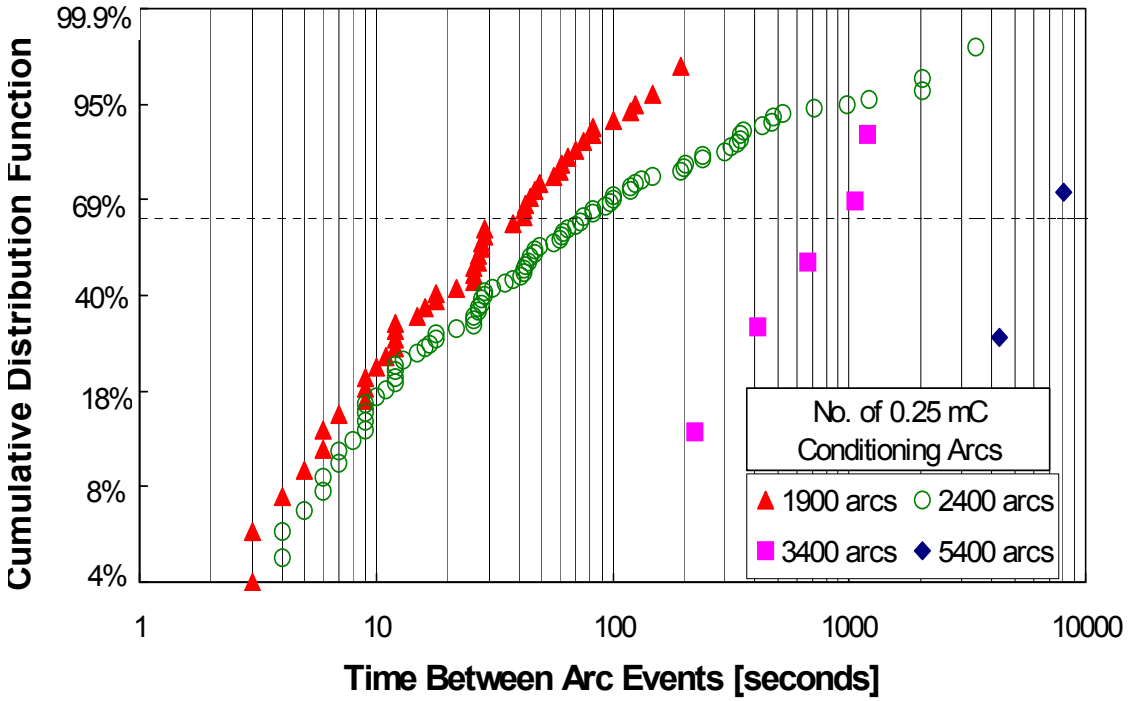

Figure 3.26 **Weibull plots showing the effect of increasing the number of ~0.25-mC conditioning arcs on the arc period at the 0.5 mm grid spacing with E = 7.41 kV/mm. Each data set was recorded over a 3-hr run.**

Dozens of Weibull plots were recorded for various values of arc charge transfer level and number of conditioning arcs. Figure 3.28 summarizes the data in Figures 3.26 and 3.27 and the differences between the results of using 1.0 versus 0.25 mC is apparent. We did not investigate charge transfer values above 1 mC because significant arc damage occurs at levels higher than 1 mC as identified by Goebel[12]. It is interesting to note that the Weibull slope parameter, β_w, always had a value less than 1 for all surface condition states indicating that either (a) the grids are arcing more in a "burn-in" period at the beginning of a test or (b) the grid arcs are occurring in clusters where one arc causes a series of follow-on arcs. In addition, although extremely limited Weibull data was taken with the other materials tested, they all had slope parameters less than 1.

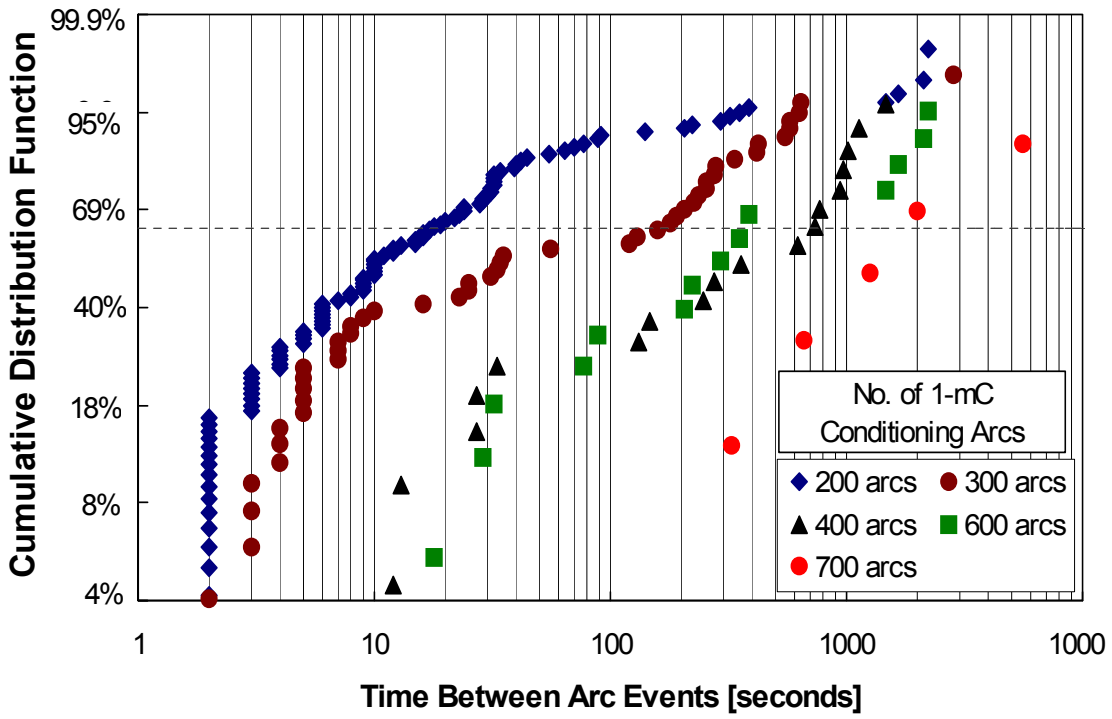

Figure 3.27 **Weibull plots showing the effect of increasing the number of ~1.0-mC conditioning arcs on the arc period at the 0.5 mm grid spacing with E = 7.41 kV/mm. Note that this electric field condition was not reached until 200 arcs had been initiated.**

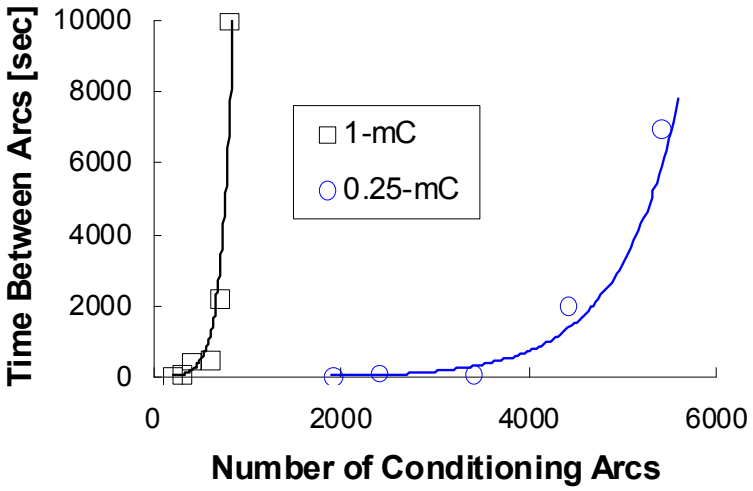

Figure 3.28 **Variation in number of conditioning arcs to reach a certain characteristic life for charge transfer values of 0.25 and 1.0-mC. Note: each data point corresponds to a 3-hr run at E=7.41 kV/mm.**

As discussed earlier, one set of CC gridlets (grid set #1) was exposed in the accelerated wear test facility, and a second set of CC gridlets (grid set #2) was subjected to the direct impingement erosion technique. Both sets were conditioned using small controlled arcs at a level of 1-mC per arc. At various intervals in the conditioning process, 3-hr runs with beamlet extraction were conducted at an electric field of 7.81 kV/mm with a grid gap of 0.5 mm. These timed runs were used to generate Weibull plots identical to the ones shown above to determine the characteristic life (or mean time between arc events). This procedure was performed for the BOL grid surface and after each exposure was conducted. The variation in the characteristic life gives an indication of how well the surface is being conditioned along with providing a comparison of the surface quality of one grid set to the other. A plot of the measured characteristic life for each surface condition is presented in Fig. 3.29. Grid set #1 at BOL was noticeably different from grid set #2. It is believed that some of the differences are due to processing discussed earlier.

The effect of vacuum chamber pressure also affects the frequency of breakdown. Both Kaufman[23] and Kerslake[72] have reported that pressures below ~10^{-6} Torr give a mean interval between breakdowns in ground tests of mercury thrusters that matches the rates found in space tested thrusters. For mercury thrusters, pressures above this range increase the arc frequency (or equivalently decrease the arc period). As noted earlier, the chamber pressure in this study was 1.2×10^{-5} Torr.

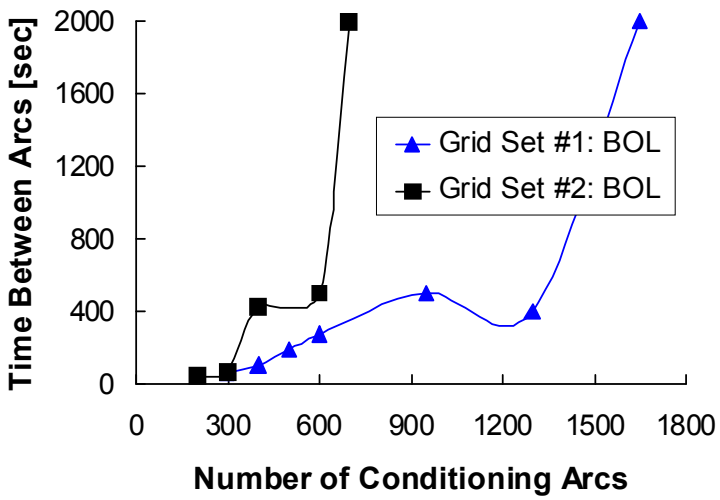

Figure 3.29 Arc period variation with number of conditioning arcs for two similar gridlets that were at the BOL condition. Note that each data point was taken over a 3-hr run.

3.2 Pyrolytic Graphite

An alternate means of fabricating carbon-based ion thruster optics is through the use of pyrolytic graphite (PG). This material is relatively isotropic in the planeular direction, with no directional fibers as in carbon composite materials. The elastic modulus of pyrolytic graphite is an order of magnitude lower than that of carbon-carbon composites. Structural vibration modes will thus be at lower frequencies, and larger displacements will occur. Pyrolytic graphite has a slightly negative coefficient of thermal expansion (CTE) through about 300°C. Because there is usually a radial temperature distribution in ion optics assemblies, the PG grid material will be in tension. It is argued that the tensile forces result in a very stable geometry in which the surface is pulled taught, and grid gap variation due to thermal loading should be much less compared to conventional grid designs using metals with high positive CTE.

Pyrolytic graphite is formed through a pyrolysis reaction, which involves the chemical vapor deposition (CVD) of carbon at very high temperature. The PG used in

this study was manufactured by Minteq International of Easton, Pennsylvania. The grade of this pyrolytic graphite was a hybrid of their "Continuously Nucleated" and their "Substrate Nucleated." The hybrid provides more desirable properties for ion thruster grids than either material by itself. The PG material is configured with the carbon crystal planes normal to the surface. Flat 7.5 x 7.5 cm gridlets were cut from a larger piece made in this manner and the holes were drilled to the NEXIS geometry. Small surface bumps and depressions can be seen in Figure 3.30, which were residual features left over from the growth process. Previous work by Goebel[15] has shown that the side with the outward facing bumps performs at the highest electric fields. The side with concave depressions showed higher field emission, probably from the edges of the depressions. Therefore, the side with the bumps was chosen to face the screen grid in all tests performed in this study. It should be noted that Goebel sandblasted his PG material, which resulted in a slight improvement in the voltage standoff capability. This was not done for the PG material tested in this study.

Figure 3.31 shows field emission measurements as a function of applied arcs for the PG material at BOL with a grid gap of 0.5 mm. The first one hundred arcs at the 1-mC level cause a significant decrease in the measured field emission while a few hundred more result in a nearly fully conditioned surface in contrast to the CC material which required several hundred more arcs to reach the fully conditioned state.

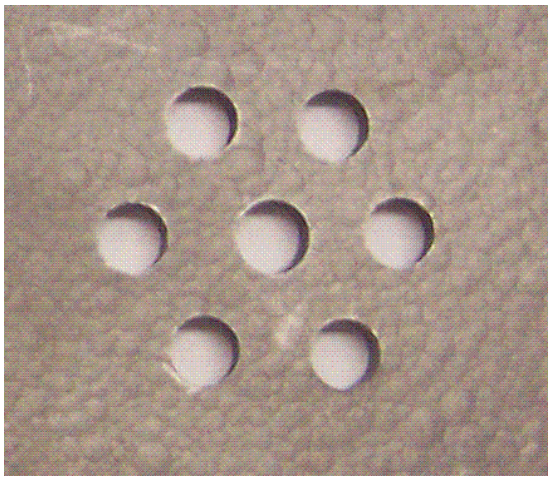

Figure 3.30 NEXIS-style PG screen gridlet prior to testing

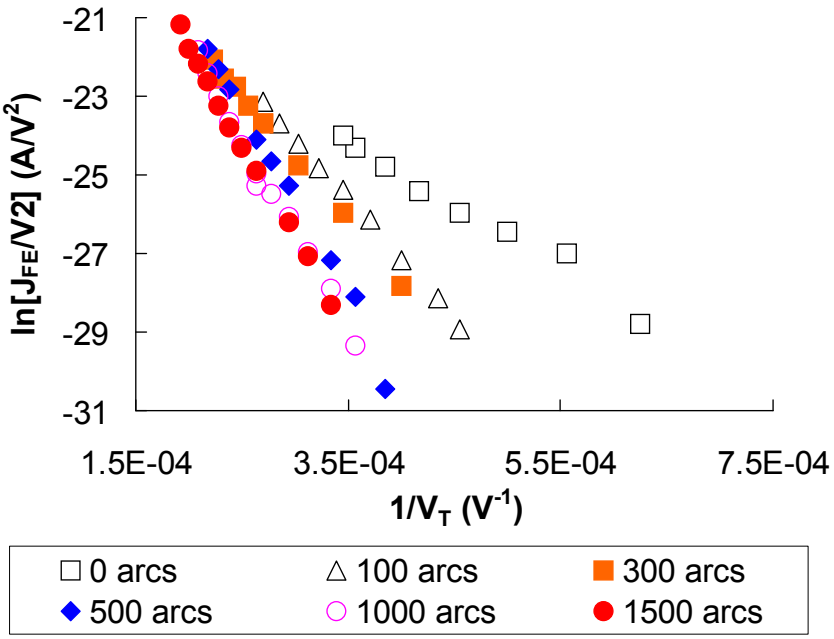

Figure 3.31 Fowler-Nordheim plots for BOL PG gridlets. The shift to the left and to higher slope magnitudes correspond to decreasing field enhancement factors and decreasing effective emission area causes by the application of the 1-mc conditioning arcs.

Figure 3.32 gives the variation of the localized electric field enhancement factor with the number of conditioning arcs at the 0.5 mm grid spacing. The plot in Figure 3.33 summarizes the effect that the number of 1-mC conditioning arcs has on the applied

electric field breakdown strength for PG. The PG gridlets leveled off at an enhancement factor of approximately 300 while the CC gridlets leveled off at 400. In contrast to the enhancement factor comparison, the CC and PG gridlets achieved similar maximum applied electric field values of ~11 kV/mm. Goebel[15] has shown that PG with similar surface preparation and aperture features to have a maximum electric field of ~3.5 kV/mm at a grid gap of 0.5 mm prior to the application of any conditioning arcs. After the application of ten arcs at 1-mC/each, using a ball-and-plate experimental setup, the maximum electric field increased to ~5 kV/mm. After the application of ten arcs at 10-mC/each the maximum electric field increased to ~7 kV/mm. However, Goebel attributes this final increase to coating of the PG surface with carbon from the anode ball, which may have raised the threshold voltage. As mentioned earlier, all gridlet experiments conducted for this thesis were performed with the screen and accelerator gridlets made from the same material. The other difference between data reported herein and Goebel's data can be attributed to differences in breakdown field. Goebel defines the breakdown field as the field where the first arc occurs while in this thesis it is defined as the electric field where continuous arcing occurs.

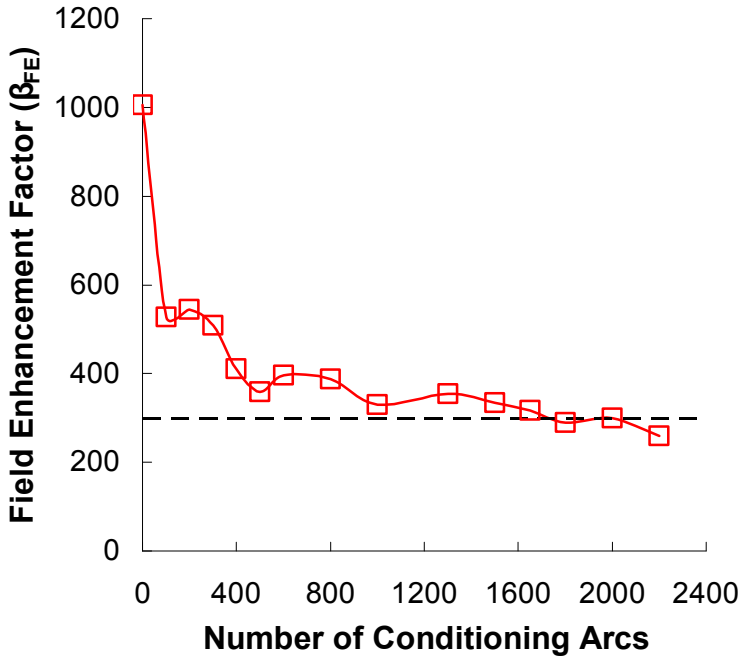

Figure 3.32 **Electric field enhancement factor variation with number of 1-mC conditioning arcs. Dotted line corresponds to an enhancement factor of 300.**

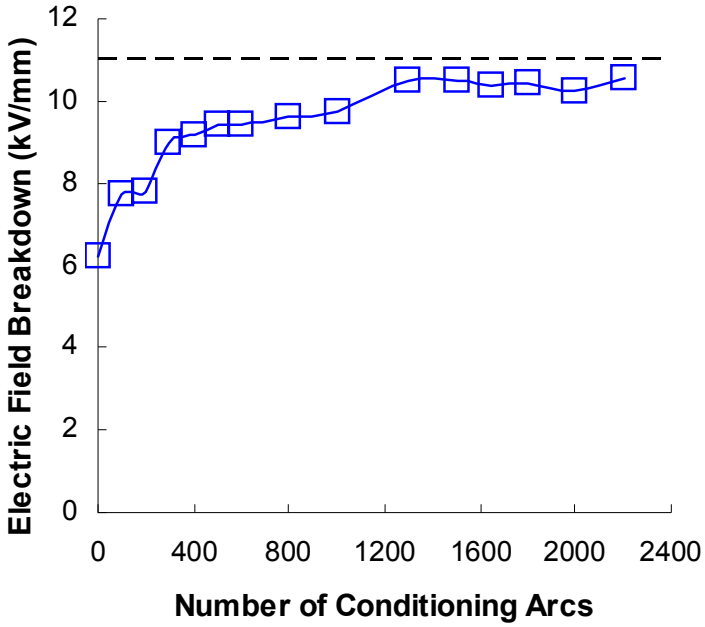

Figure 3.33 **Electric field breakdown field variation with number of 1-mC conditioning arcs. Dotted line corresponds to a field of 11 kV/mm.**

An interesting characteristic of PG was its ability to withstand very high field emission levels prior to the onset of continuous arcing (as shown in Figure 3.34). Although the field emission current of the unconditioned PG is very similar to the CC material, the current for the fully conditioned PG material is nearly 9x larger then the CC material at an applied electric field of 10 kV/mm. An interesting physical property of PG is its high in-plane thermal conductivity that exceeds all of the other materials tested in this study. The high in-plane conductivity on the screen electrode may help spread the heat deposited (by field emitters) from the accelerator grid and reduce the amount of vaporized or adsorbed material evolved from the screen electrode. The lower outgassing rate may explain the ability of PG to withstand higher field emission current without arcing.

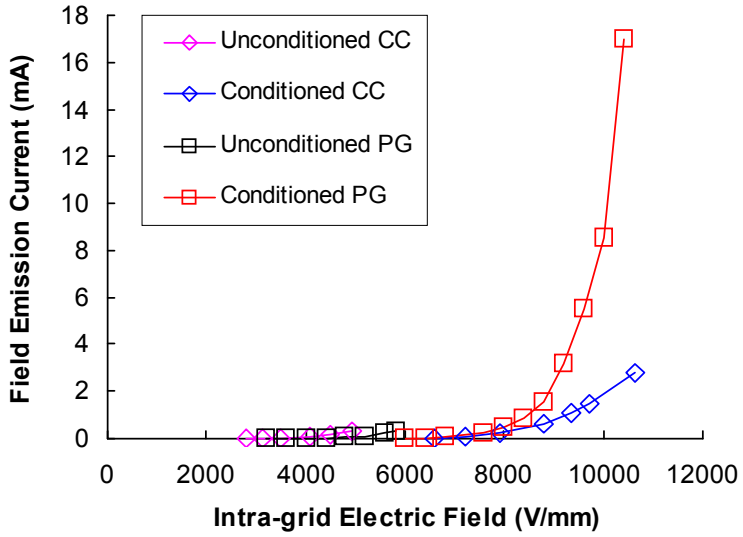

Figure 3.34 Field emission current versus applied electric field for CC and PG.

Figure 3.35 shows photographs of the PG screen and accelerator grids after the application of over 2,200 arcs with a charge transfer of 1-mc/arc. Note the significant damage on the screen electrode caused by the deposition of arc energy. Figure 3.36 shows a strong correlation between field emission and breakdown for PG. Upon reaching

a certain critical field emission value, an arc would occur causing the field emission to drop but over time (~30 seconds) the field emission would again begin to rise and another arc would occur at the critical value. Note that the test data shown in Fig. 3.36 were obtained with the charge transfer level per arc set at only 0.01 mC.

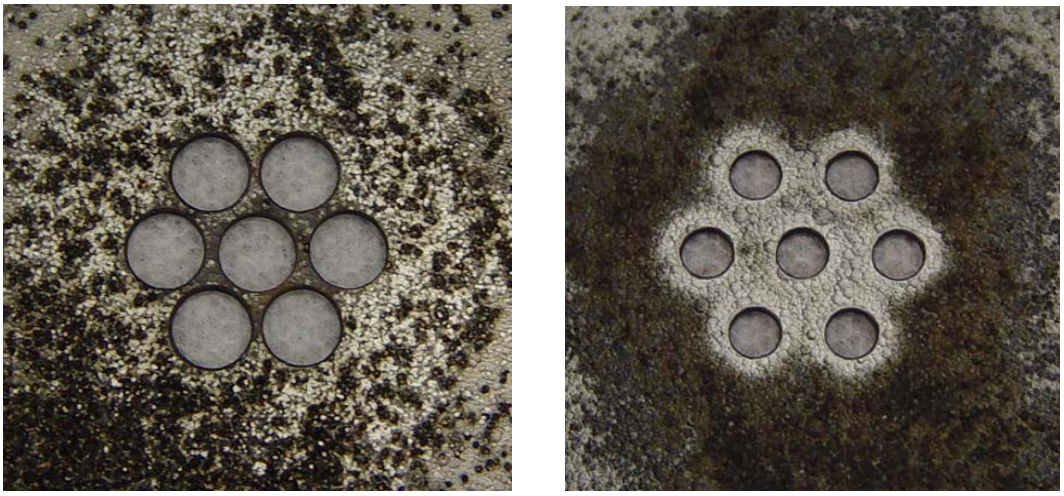

a) Downstream side of screen gridlet b) Upstream side of accelerator gridlet

Figure 3.35 NEXIS-style PG screen gridlet after undergoing over 2200 1-mc arcs.

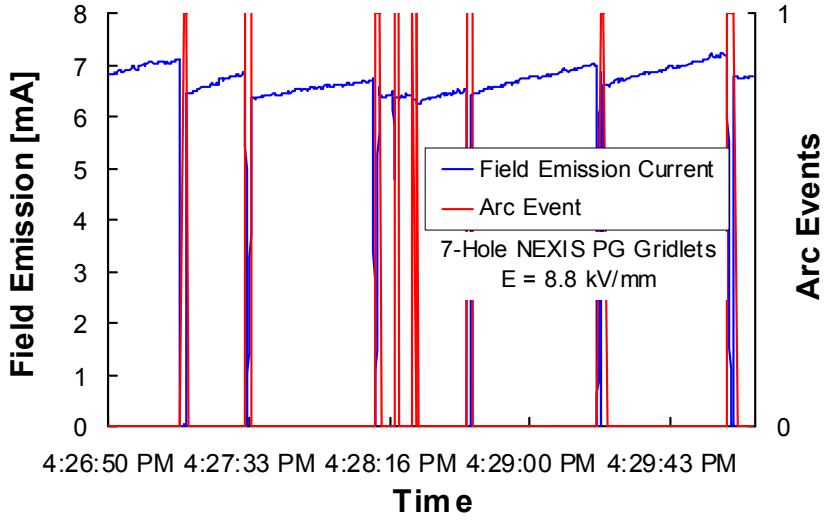

Figure 3.36 Variable field emission behavior commonly observed with PG material at electric fields below the value that causes continuous arcing (i.e., 9.4 kV/mm). Data shown were collected after 600, 1-mC conditioning arcs had been applied.

3.3 Molybdenum

The third material chosen for testing was molybdenum. Molybdenum has been the standard material used in ion thrusters for many years and is commonly used in electron guns and other pulsed power devices that are operated at high voltage. To examine the typical material surface used in ion thrusters, a molybdenum sample (with a purity of 99.9%) was first machined to the NEXIS accelerator grid geometry, followed by the edges and corners being rounded to provide a smooth profile so that high electric fields would not be produced. Next the surface was grit blasted and then cleaned using acetone. The resulting surface texture was to similar actual ion thruster grids that are chemically etched prior to use. Due to lack of available material selection, the molybdenum sample had a thickness of 0.56 mm, which was thinner than the NEXIS screen and accelerator grid thicknesses. Because of the thickness and difficulty in drilling holes, the molybdenum tests were conducted with both grids (i.e. the negatively and positively biased grids) having the same accelerator hole geometry. Figure 3.37 shows the molybdenum material just prior to testing.

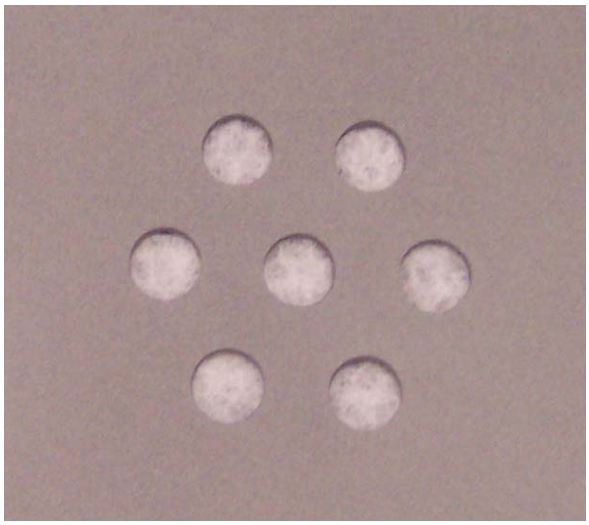

Figure 3.37 NEXIS-style molybdenum screen gridlet prior to testing.

Figure 3.38 shows the strong correlation between arcing (10 μC/arc) and the rise in field emission for the molybdenum material during the initial run time of the ion source. The different levels of field emission that trigger an arc to occur could be due to either the sharpening of a protrusion tip after an arc (as opposed to blunting) or to the formation of a new protrusion in a different region of the material that is allowed to emit electrons to a higher degree before initiating an arc.

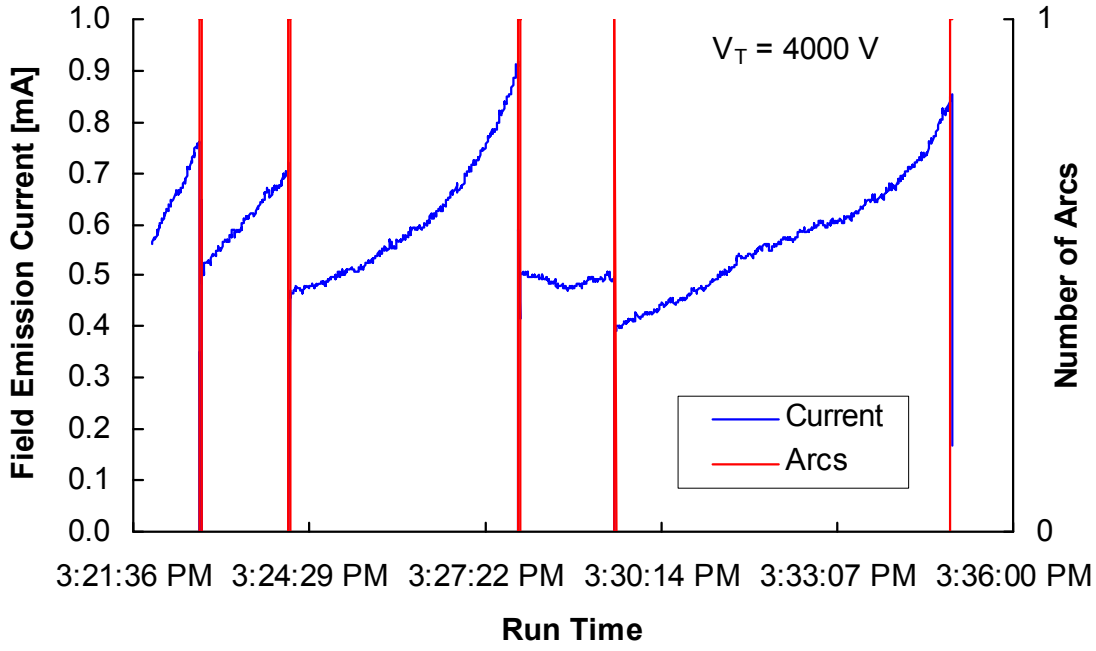

Figure 3.38 Snap shot of field emission strength versus arcing behavior during initial testing of the molybdenum material (i.e. prior to conditioning). The charge transfer per arc is ~10 μC.

Measurements of field emission were made between arc conditioning sequences and F-N plots at BOL are shown in Figure 3.39. As can be seen, the first one hundred arcs at the 1-mC level cause a significant decrease in the measured field emission. While the CC material required the application of over 1500 arcs to fully reach the minimum

field emission levels, molybdenum only requires about 500 arcs. Beyond these initial 500 arcs, little change in field emission is measured.

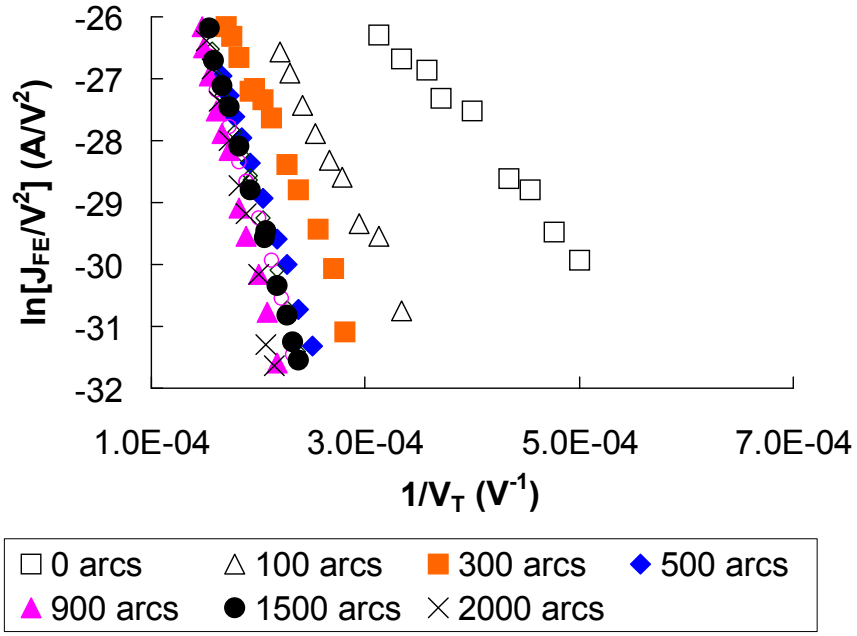

Figure 3.39 Fowler-Nordheim plots for BOL molybdenum gridlets. The shift to the left and to higher slope magnitudes correspond to decreasing field enhancement factors and decreasing effective emission area causes by the application of the 1-mc conditioning arcs.

Figure 3.40 gives the variation of the localized electric field enhancement factor with the number of conditioning arcs at the 0.5 mm grid spacing. The field enhancement factor β_{FE} is calculated from the slope of the linear section of the F-N plot using Equation 2.11 with a value of $\Phi = 4.6$ eV for the work function. Numerous experiments have been conducted using molybdenum with varying amounts of surface conditioning and preparation prior to testing. Typical measured enhancement factors range from 20 to 35 for highly polished electrodes[73], 80-100 for handpolished, lapped, and electropolished, and 250 for unpolished electrodes[67]. Although the final enhancement factors shown in

Figure 3.40 are similar to the ones from reference 67, it should be noted that the molybdenum sample tested in that work was not grit blasted.

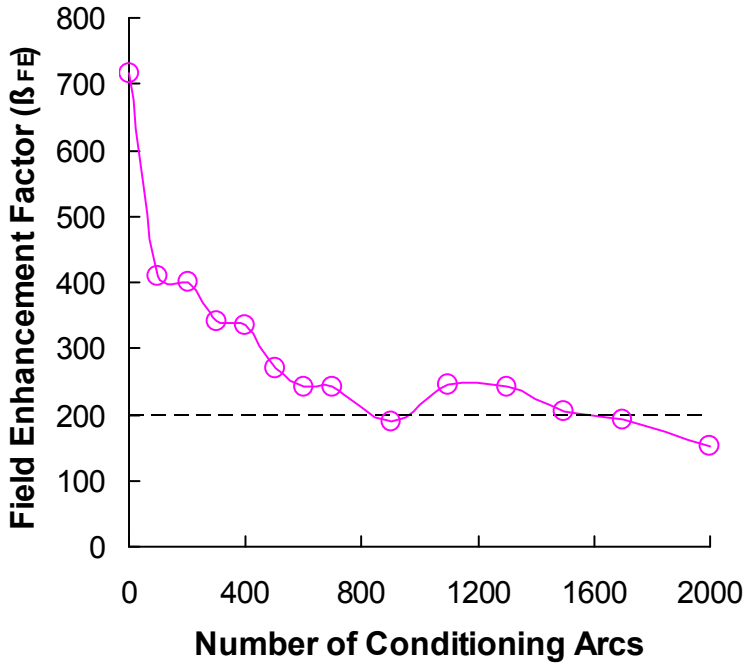

Figure 3.40 F-N plots for BOL molybdenum gridlets. Electric field enhancement factor variation with number of 1-mC conditioning arcs.

The plot in Figure 3.41 summarizes the effect that the number of conditioning arcs has on the applied electric field breakdown strength for molybdenum. As shown, grit blasted molybdenum with drilled apertures has a maximum threshold electric field of approximately 15 kV/mm with the application of 2000 1-mC arcs. The application of an additional ~100 arcs with a charge transfer of 13-mC per arc did not increase this maximum applied electric field. Goebel[15] has shown molybdenum with similar surface preparation and apertures to have a maximum electric field of ~12.5 kV/mm at a grid gap of 0.5 mm prior to any conditioning arcs. After the application of conditioning arcs, the maximum electric field increased to ~16 kV/mm. It is worth noting that Goebel drilled

holes into his molybdenum material and his resulting peak threshold electric field value is remarkably close to the peak breakdown field shown in Figure 3.41.

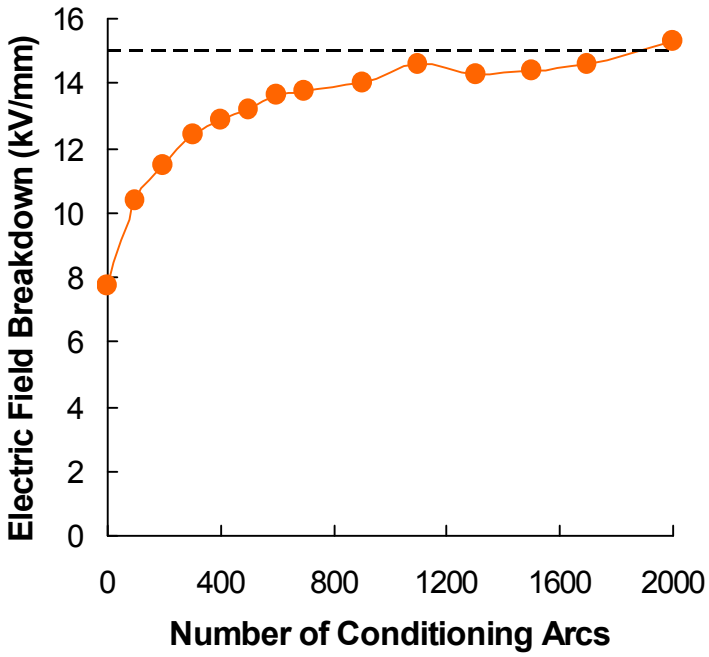

Figure 3.41 F-N plots for BOL molybdenum gridlets. Electric field breakdown field variation with number of 1-mC conditioning arcs. Dotted line is at 15 kV/mm.

Kaufman[23] presented data on a 30-cm ion thruster with molybdenum ion optics that showed a maximum electric field of approximately 5 kV/mm at a grid gap of 0.5 mm with ion beam extraction. Kaufman defines the maximum electric field as the field sufficient to trip the overload protection of the high voltage power supply (i.e. defined as the electric field causing the first arc). Figure 3.41 shows an unconditioned grid set achieving a maximum breakdown field of 7.7 kV/mm. For the molybdenum grids used to generate Figure 3.40, the very first initial arc actually occurs at an electric field of 6.8 kV/mm (only slightly higher than Kaufman's 5 kV/mm measurement). The remaining difference is likely due to the fact that Kaufman's grids had thousands of apertures while

the molybdenum gridlets used in this thesis have only seven. Another difference is that Kaufman used data taken with mercury as opposed to xenon gas. An interesting trait of molybdenum is that the presence of xenon gas suppressed the rise of field emission so that higher breakdown fields are achieved when xenon gas is flowing versus without. Further testing is needed to quantify accurately the impact of different gases on molybdenum's electric field breakdown characteristics when ion beamlets are extracted.

Figure 3.42 compares the level of field emission produced by the molybdenum and carbon-carbon materials. As can be seen, beyond a certain applied electric field, molybdenum produces only a small fraction of the field emission that is produced by the carbon-based material.

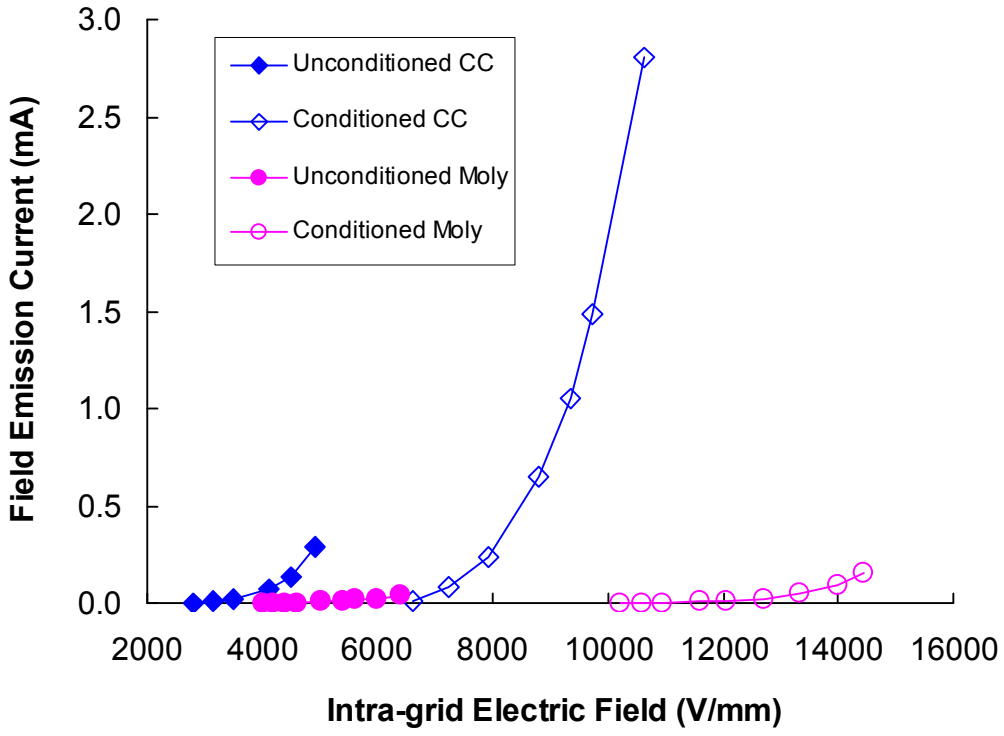

Figure 3.42 Field emission current versus applied electric field for CC and molybdenum grids.

Figure 3.43 shows photographs of the molybdenum grids after the application of several hundred arcs with a charge transfer level of 1-mc/arc (i.e. the required number of arcs to partially condition the molybdenum gridlets). As expected, the application of these 1-mC arcs has only a minor impact on the grid surface when compared to the PG and CC grid surfaces after arcing has occurred. In fact, one can hardly tell that the grit blasted accelerator grid has any arc marks at all. In addition, only a few arc termination sites are present on the screen grid, which are mostly located around aperture edges. Figure 3.44 shows the grid surface after increasing the arc charge transfer level to 13 mC. The higher charge transfer level has resulted in the arcs clearly covering the surface of both grids. Despite the increase in charge transfer level, inspection of the surface showed much less damage than what was seen with the carbon-based materials.

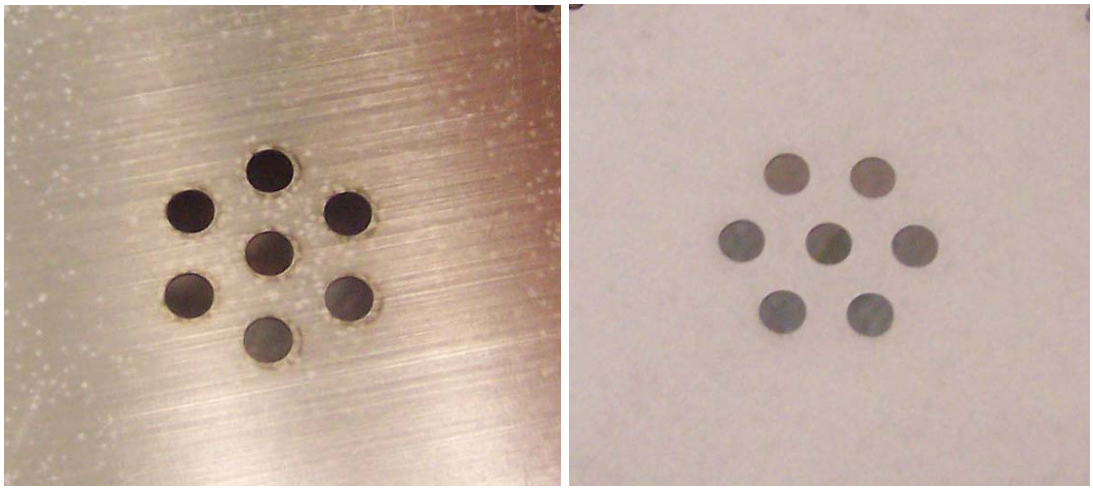

a) Downstream side of screen gridlet b) Upstream side of accelerator gridlet

Figure 3.43 NEXIS-style molybdenum gridlets after undergoing several hundred 1-mc arcs. Note: screen grid is not grit blasted.

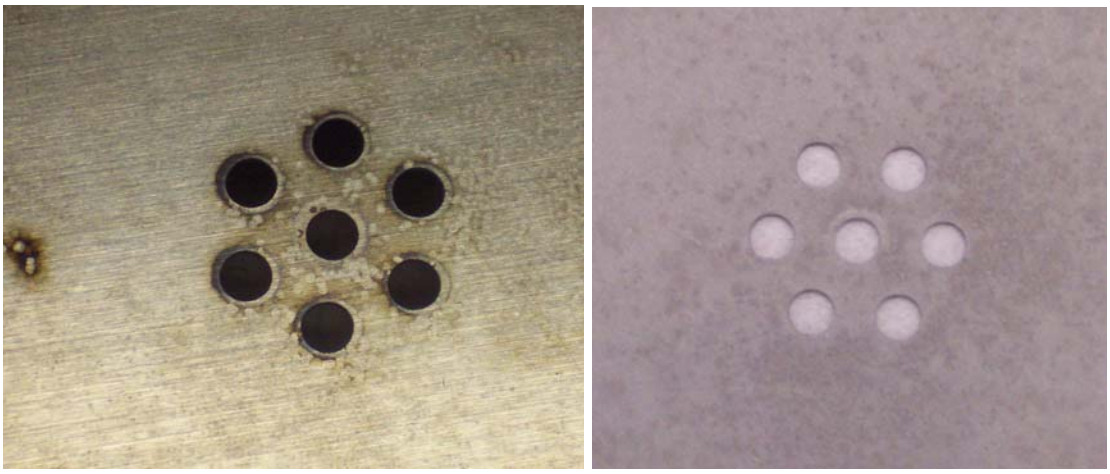

a) Downstream side of screen gridlet b) Upstream side of accelerator gridlet

Figure 3.44 NEXIS-style molybdenum gridlets after undergoing over an additional 1000 arcs at 1-mC/per plus 100 13-mc arcs. Note: screen grid is not grit blasted.

3.4 Poco Graphite

The final material tested was Poco graphite. Photographs of the gridlets prior to testing are shown in Figure 3.45. Measurements of field emission were made between arc conditioning sequences and F-N plots are shown in Figure 3.46. As can be seen, the first one hundred arcs at the 1-mC level cause a significant decrease in the measured field emission while a few hundred effectively condition the surface as was the case for the PG material.

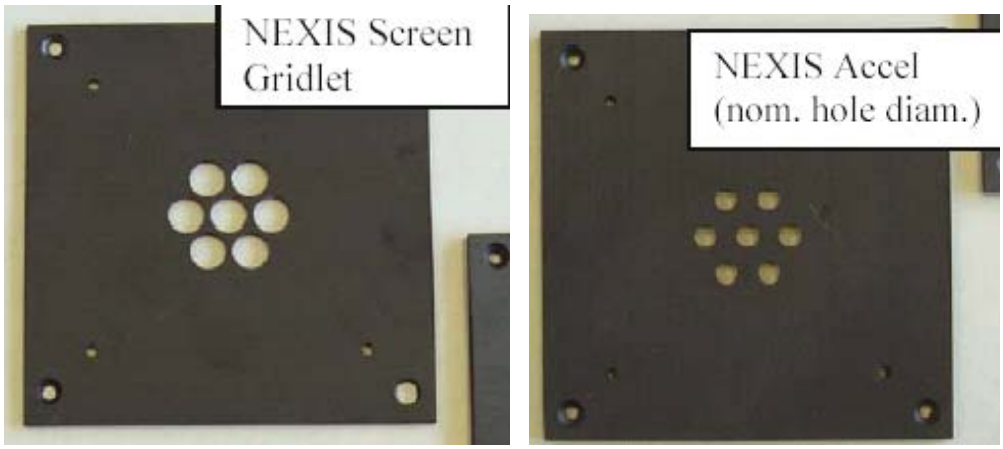

Figure 3.45 Photographs of NEXIS gridlets fabricated from Poco graphite.

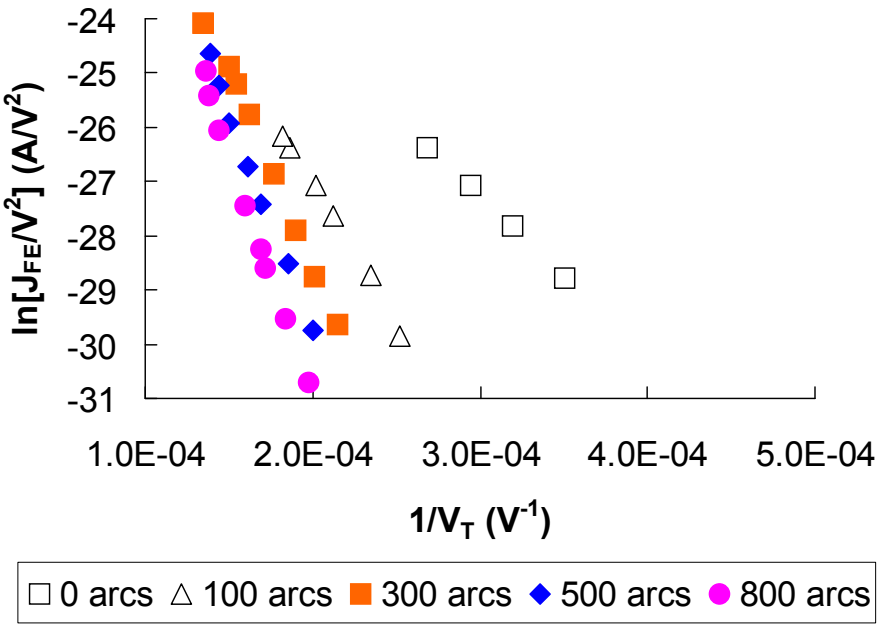

Figure 3.46 F-N plots for BOL Poco gridlets. The shift to the left and to higher slope magnitudes correspond to decreasing field enhancement factors and decreasing effective emission area causes by the application of the 1-mc conditioning arcs.

Figure 3.47 gives the variation of the localized electric field enhancement factor with the number of conditioning arcs at the 0.5 mm grid spacing, and the plot in Figure 3.48 summarizes the effect that the number of 1-mC conditioning arcs has on the applied electric field breakdown strength. Poco gridlets leveled off at an enhancement factor

which was half the factor achieved by the CC gridlets (200 vs. 400) and this translated into an increase in the maximum electric field of 35% (11 to 14.8 kV/mm).

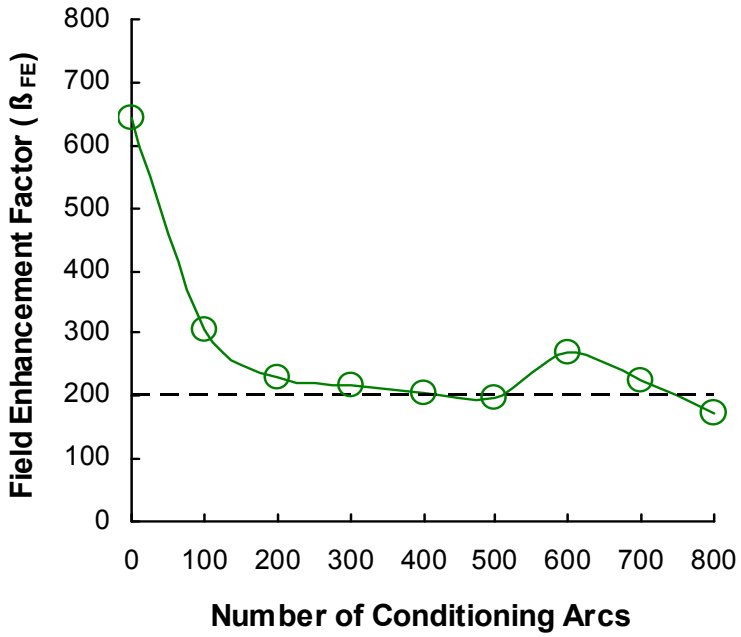

Figure 3.47 **F-N plots for BOL Poco gridlets. Electric field enhancement factor variation with number of 1-mC conditioning arcs.**

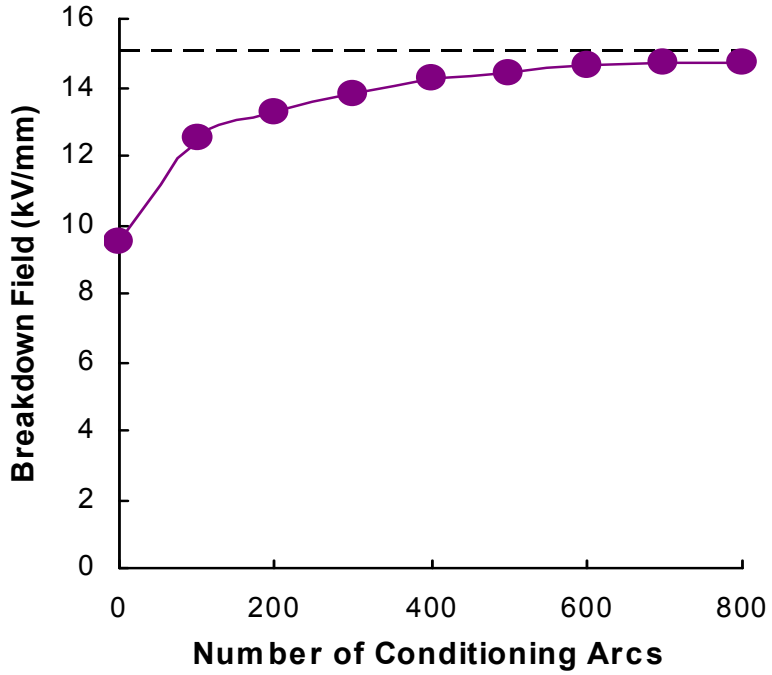

Figure 3.48 **F-N plots for BOL Poco gridlets. Electric field breakdown variation with number of 1-mC conditioning arcs. Dotted line is at 15 kV/mm.**

Figure 3.49 compares the level of field emission for a given applied electric field for Poco graphite and CC gridlets. As expected, CC gridlets show significantly more field emission due to the carbon fibers that make up the material structure. It is interesting to note that the unconditioned CC surface can only achieve a maximum electric field of 4.9 kV/mm, which is significantly below the minimum electric field needed to start recording any level of field emission for the Poco graphite material (5.7 kV/mm). Similar behavior was observed with the fully conditioned surfaces of each material.

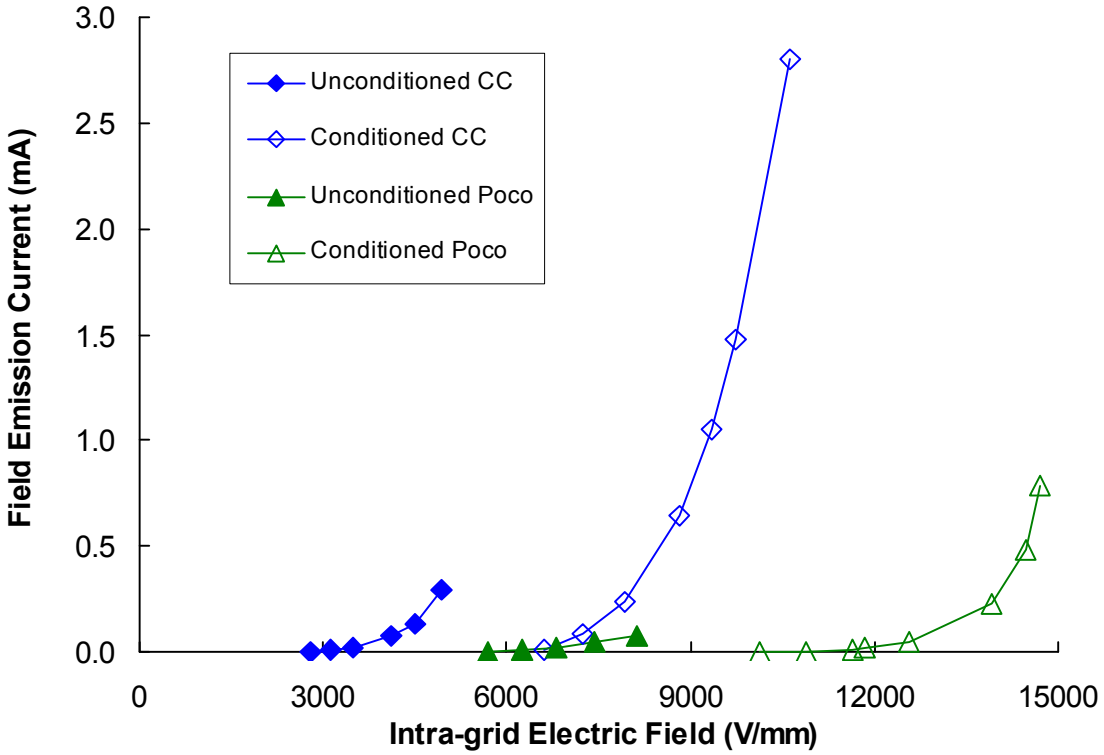

Figure 3.49 Field emission current versus applied electric field for CC and Poco grids.

3.5 Summary of Experimental Results

Figure 3.50 gives the variation of the localized electric field enhancement factor with the number of conditioning arcs at the 0.5 mm grid spacing for all of the materials tested. The data are for the BOL grid surface for each material. As can be seen from Fig.

3.50, CVD coated carbon-carbon composite material had an enhancement factor for its conditioned state that was similar to pyrolytic graphite after initiating 1200, 1-mC arcs between the grids. The large initial enhancement factors for the carbon composite material could be due to loose fibers left over from the laser drilling processes. The grit blasted molybdenum consistently had the lowest enhancement factors.

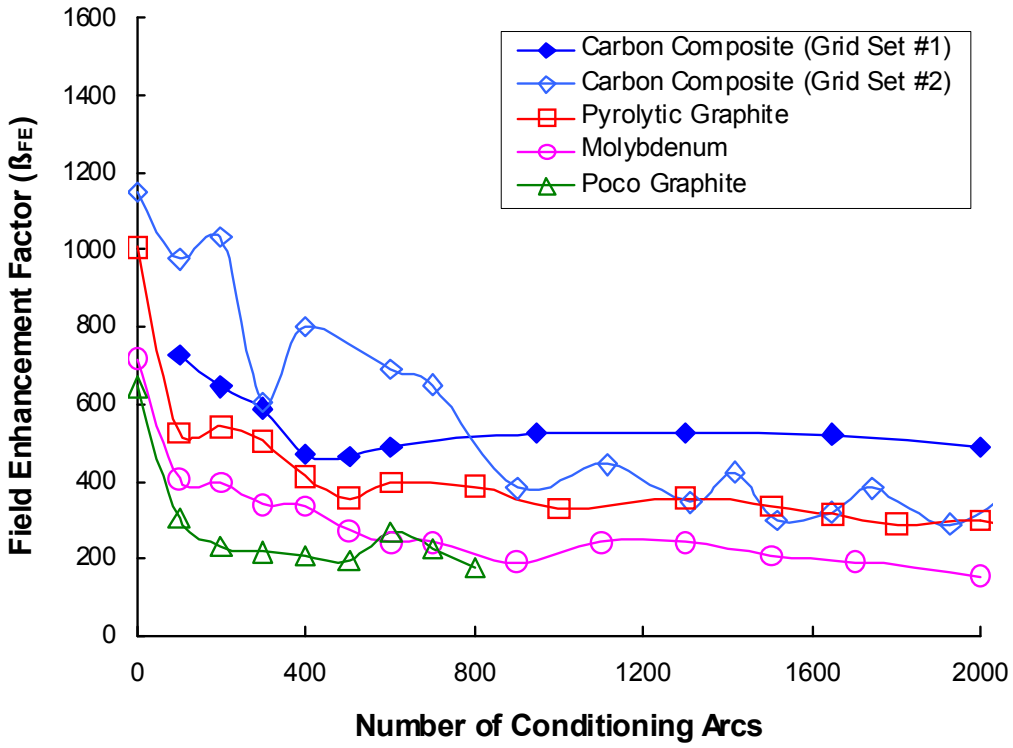

Figure 3.50 Electric field enhancement factor variation with number of 1-mC conditioning arcs. Grid spacing = 0.5 mm.

A summary of the breakdown field as a function of applied conditioning arcs (at 1-mC/arc) for all the materials is shown in Fig. 3.51. Poco graphite and molybdenum were found to sustain the highest electric fields while carbon-carbon composite and pyrolytic graphite displayed the lowest electric field values at breakdown. It should be noted that an additional 200 arcs at the 10 mC level were applied to both the pyrolytic

graphite and molybdenum samples beyond the 2000 1-mC arc study and no further increase in the breakdown field was observed.

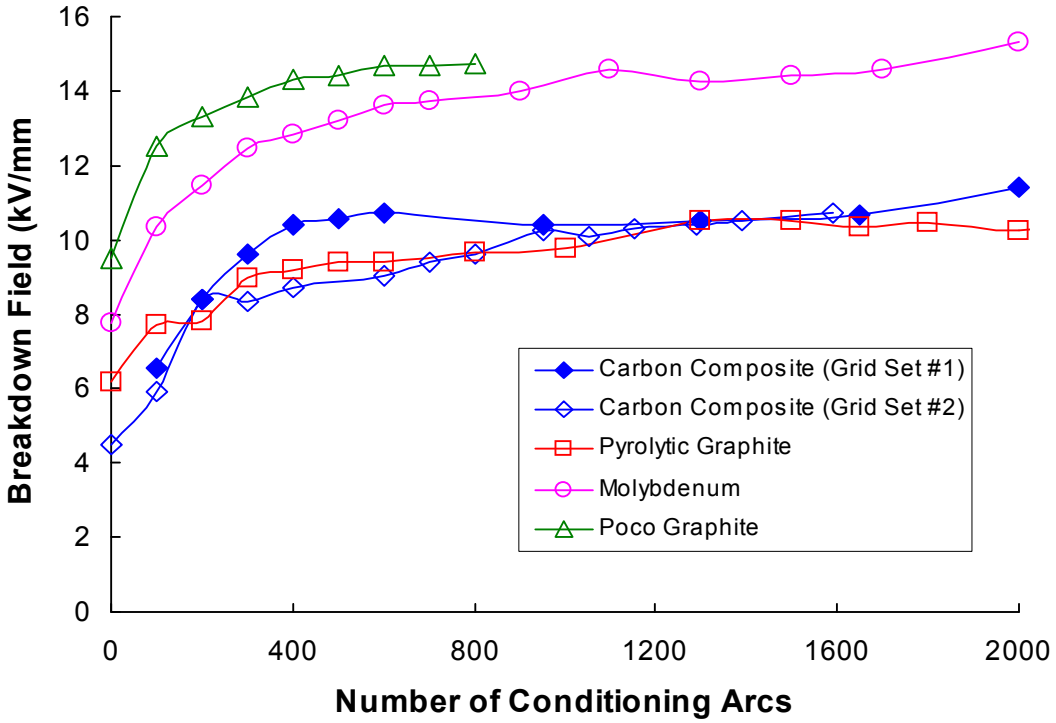

Figure 3.51 Breakdown field dependency on the number of 1-mC conditioning arcs. Grid spacing = 0.5 mm.

As indicated earlier, the enhanced (or microscopic) breakdown field for carbon-carbon composite, after displaying some initial fluctuations for the unconditioned state, was found to be 5,400 kV/mm independent of grid gap. Unfortunately, only one grid gap was tested for the pyrolytic graphite, Poco graphite, and molybdenum (in contrast to the gaps of 0.5 mm to 2.7 mm tested for CC). Therefore, a high level of uncertainty exists in the enhanced breakdown field data for these materials (i.e. $\pm$1000 kV/mm). With this uncertainty in mind, the reader is referred to a summary of the measured enhanced electric field breakdown values for the conditioned materials contained in Fig. 3.52. Poco graphite and CC were found to be similar at ~5000 kV/mm, while pyrolytic

graphite and molybdenum were found to be lower at ~3000 kV/mm. It is noted, however, that the enhanced breakdown field for PG was observed to increase to ~4200 kV/mm in the presence of xenon and when ions are extracted.

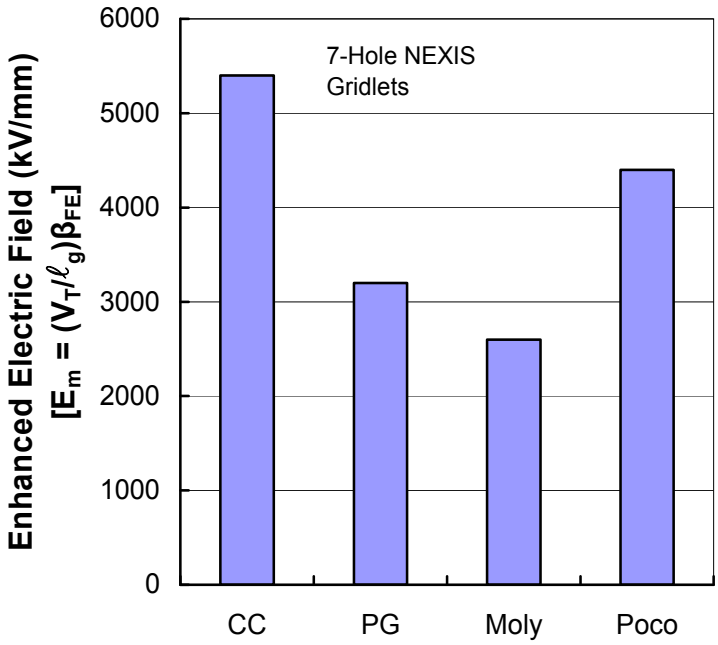

Figure 3.52 Comparison of enhanced electric field breakdown data for carbon-carbon (CC), pyrolytic graphite (PG), Molybdenum, and Poco graphite.

Published data on the enhanced breakdown field for molybdenum is typically 5000 kV/mm (+/- 1000 kV/mm).[67,70,57,74] The molybdenum material used in our study, however, was grit blasted to match the surface texture of the heavily etched molybdenum material used in typical ion thrusters, and the sand blasting process could have lowered the enhanced breakdown field compared to published experimental data. In addition, studies have found that high voltage breakdown experiments are affected when molybdenum electrodes are exposed to the evaporation products of heated dispenser cathodes and thoria-coated tungsten filaments. These evaporated films tend to reduce the enhanced breakdown field down to 1000 kV/mm in the case of the 4:1:1 barium oxide

dispenser cathode and down to 3700 kV/mm in the case of a tungsten filament.[74] In addition, it has been found that field emission levels continuously increased with longer exposure to evaporated products of 4:1:1 cathodes. This is interesting as 4:1:1 dispenser cathodes are typically used in ion thrusters. It is noted in this regard that 2% thoriated-tungsten filaments were used for both the discharge and neutralizer filaments in the ion source used for the research discussed in this thesis. These observations from literature sources could also explain the trend displayed in Figure 3.17 when the enhancement factor peaked with the filaments 'on' but dropped soon after they were turned 'off'.

Figure 3.53 summarizes the overall findings of this study. As expected, unconditioned electrodes were found to display lower field emission onset and breakdown electric fields. Both onset and breakdown improvements of ~2x were observed after small controlled arcs were applied. Carbon-carbon was observed to be similar to or slightly better than PG after the conditioning process was completed. Both molybdenum and Poco graphite were found to be 1.5x to 2x higher in onset and breakdown electric fields both before and after conditioning compared to CC and PG. Data obtained by Goebel[15] are also plotted in Fig. 3.53 with the same criteria for the threshold for field emission (1 μA). As noted above, the materials used in Goebel's study had slightly different surface conditions. Specifically, the carbon-carbon composite material used in this study did not receive the final CVD coating after the laser beam drilling process. This missing process step is the likely cause of the lower CSU threshold values shown in Fig. 3.53. The pyrolytic graphite used by Goebel was lightly sand blasted to smooth any edges in addition to having the holes laser drilled. Neither procedure was conducted for the pyrolytic graphite gridlets used in this study, but the

threshold values are still relatively similar. The largest differences occurred for the molybdenum and Poco materials. Likely reasons for differences include (1) the use of a ball and plate setup in Goebel's work that eliminates edge effects, (2) the use of laser-drilled apertures in Goebel's molybdenum work that result in surface features that are dissimilar to apertures drilled using a CNC machine in the present work and (3) Goebel's lack of apertures into the Poco graphite material he tested. Recall that the molybdenum material used was 0.56 mm thick (i.e. thinner than the thickness of the screen grids for the other materials). It is noted, however, that the final breakdown fields for molybdenum and Poco were similar to Goebel's conditioned threshold results, which were ~1000 V/mm lower than his field breakdown values.

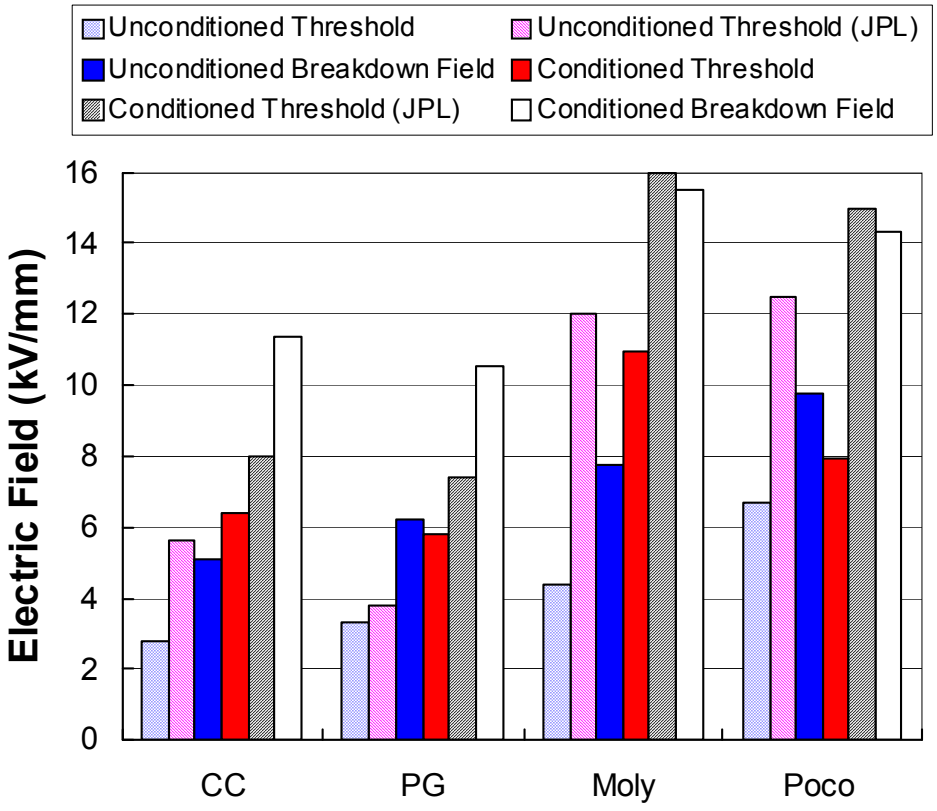

Figure 3.53 Bar graph comparing threshold electric field for field emission and electric field breakdown data for carbon-carbon (CC), pyrolytic graphite (PG), Molybdenum, and Poco graphite. Onset field emission = 0.001 mA.

Figure 3.54 contains F-N plots for all the materials tested in this study at their fully conditioned state. Both pyrolytic graphite and carbon-carbon had significantly higher levels of field emission compared to molybdenum. The large range in field emission for pyrolytic graphite (PG) is typical at all states of its surface condition. It is not known at this time why Pyrolytic graphite has such a large range in field emission output. The cause for the large variation between carbon-carbon (CC) grid sets #1 and #2 is also identified as an unknown. In this regard, it is noted that grid set #2 took many more conditioning arcs before it was able to achieve the same breakdown field as grid set #1, and this level of arc conditioning may have improved the surface of grid set #2.

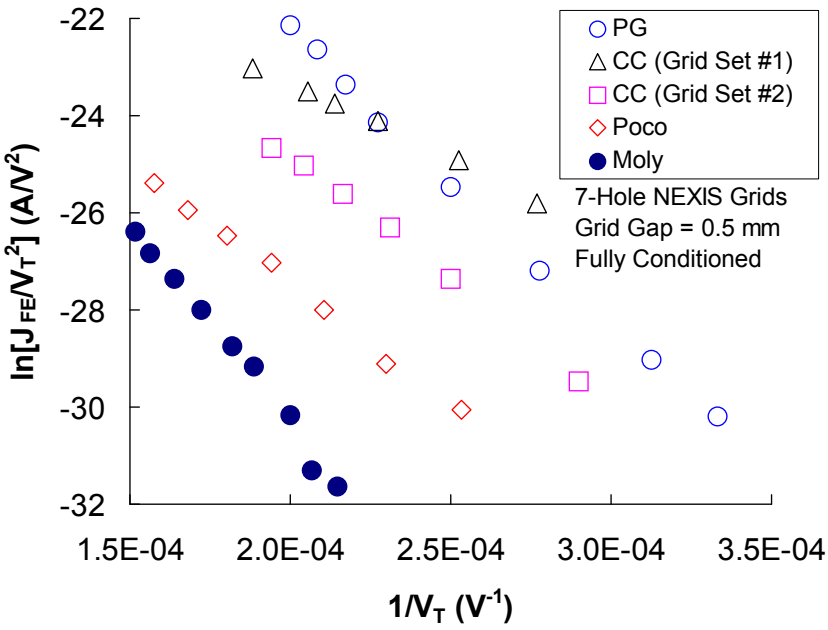

Figure 3.54 F-N plots for all the materials tested in this study at their fully conditioned state.

3.6 Area Effect

As the surface area of the electrodes is increased there is a higher likelihood that a large microprotrusion will exist. This higher probability also increases the probability of a breakdown event occurring, implying that as the surface area is increased, the voltage hold-off strength is decreased. All testing to this point has presented results for 7-hole gridlets. After proper conditioning, sustainable electric fields were observed in this study that are factors above those that seem to be limits for operating ion engines. The work presented on emission current with and without ion beamlet extraction eliminates many possible explanations for the differences in sustainable fields. Key to the extrapolation of results to full size engines is the issue of area. The gridlets used in this study have a surface area of 4.65 cm^2 (including only the area encompassing the 7 holes). For carbon-carbon optics material, a few hundred 1-mC arcs effectively condition the surface while approximately 1200 are required to condition the grids fully. If one were to scale by surface area to a full-scale NEXIS accelerator grid (2645 cm^2), one would require ~200,000 1-mC arcs to condition the NEXIS grids for operation at 10 kV/mm (an electric field value that is much higher than needed for any mission under consideration). Manually initiating 600 arcs took one hour and this arc rate is too low to consider for conditioning a large grid set in a reasonable amount of time. An automatic arc initiation system could be operated at 10 arcs per second in a conservative manner and 200,000 arcs would take 6 hr. With a slight increase in the charge transfer level, the number of conditioning arcs could be reduced significantly, however, Snyder[75] has shown that 2.5-mC charge transfer levels cause the field emission threshold to degrade on large scale thrusters.

In order to evaluate the possible application of the results to larger grids with many more holes, a preliminary investigation was conducted to determine the effect that active grid area has on the breakdown field. This test was conducted using two sets of Poco graphite 7.5 cm by 7.5 cm gridlets that were spaced at 0.5 mm. One set had 7 holes and the other had 19 holes. Measurements of field emission were made between arc conditioning sequences and F-N plots of these data are shown in Figures 3.46 and Figure 3.55. Approximately 1000 arcs are needed to condition the 19-hole grids fully (a factor of ~1.4 greater than that required for the 7-hole grids).

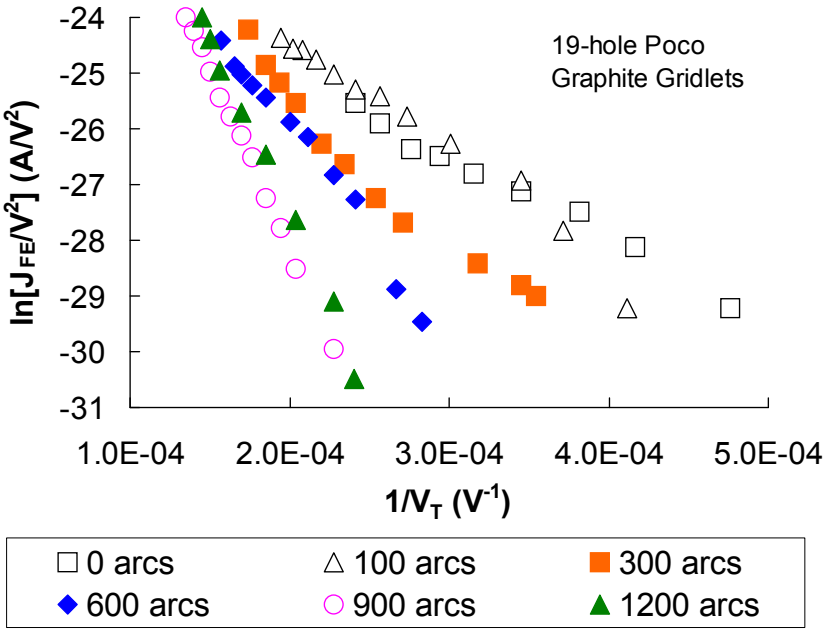

Figure 3.55 F-N plot for 19-hole Poco graphite gridlets.

Figure 3.56 summaries the effect that the number of 1-mC conditioning arcs has on the applied electric field breakdown strength for both the 7- and 19-hole gridlets. Although the 19-hole gridlets initially had a breakdown field lower than the 7-hole grid set, upon application of additional conditioning arcs, the 19-hole grid set was able to achieve the same breakdown field as the 7-hole grid set. Based on the number of arcs

required to condition the 7-hole grids (~400) and the 19-hole grids (~800), approximately 43 arcs per hole are required to condition a given grid set. Extrapolating to the NEXIS ion thruster, which has 4300 holes, approximately 200,000 1-mC arcs would be required to condition the full-scale grids (similar to the estimate provided above where an automated arc initiation system would require ~6 hr to condition the grids to a breakdown field of 10 kV/mm).

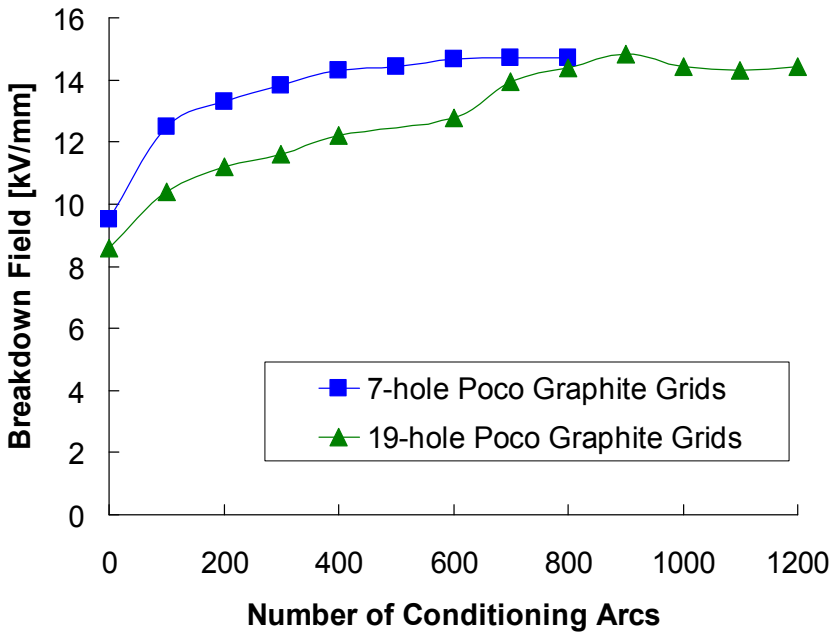

Figure 3.56 Hole effect on breakdown field strength.

Figure 3.57 gives the variation of the localized electric field enhancement factor with the number of conditioning arcs at the 0.5 mm grid spacing. An interesting feature of Figure 3.57 is that the 19-hole gridlet data are much more oscillatory and do not saturate as quickly as the 7-hole gridlet data. Although less smooth, the data in Fig. 3.56 indicates that additional arcs would bring the enhancement factor for the 19-hole gridlets closer to the 7-hole data.

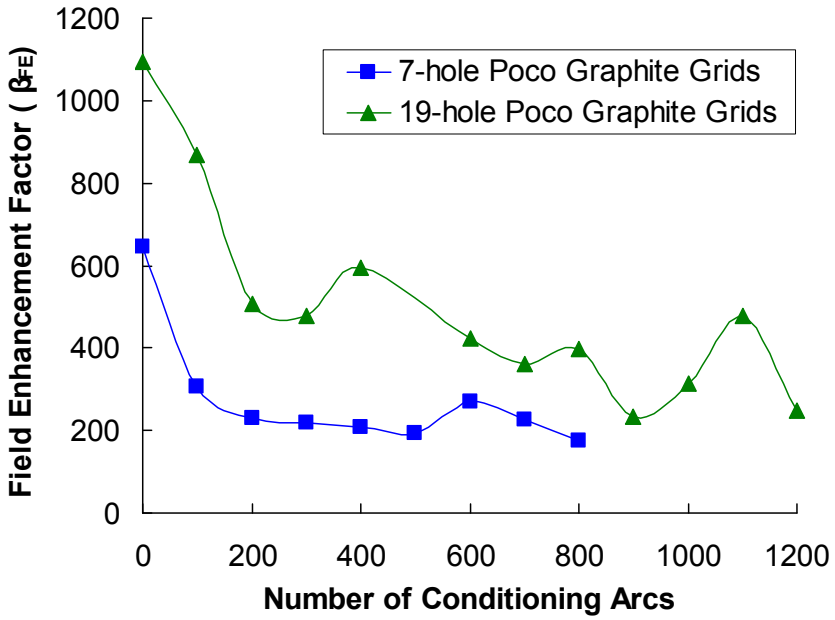

Figure 3.57 Hole effect on electric field enhancement factor.

The lower breakdown field and higher field enhancement factors for a given number of conditioning arcs (prior to reaching 700) could be attributed to an increase in the number of field emitting protrusions caused by the presence of more drilled holes. Byers[4] conducted tests with stainless steel electrodes with different numbers of holes and also found that the voltage breakdown level decreased with the number of holes drilled in the grids. However, this difference was always less than 20% for grids with 1 to 37 holes (this so happens to be the difference between the data points in Figure 3.56 prior to applying the 700th arc). As can be seen, further conditioning eventually allows the 19-hole grid set to reach the same maximum breakdown field as the 7-hole grid. It should be noted that the enhancement factor for the 7-hole grid set leveled off at a value that was 75% of the average value for the CC grid sets. Lower enhancement factors reduce the local enhanced field at any applied electric field condition, and consequently result in higher breakdown fields. The enhancement factor measured for the Poco 7-hole grid set

prior to initiating any arcs was approximately 5-10% lower than the steady state factor achieved by the CC grid sets. Based on the 0.5 mm grid gap data taken with the Poco grids, the estimated enhanced electric field at breakdown should be in the range of 5500-7200 kV/mm using the data for both the 7-hole and 19-hole grid sets.

Figure 3.58 shows a summary of the threshold and breakdown fields for the 7-hole and 19-hole Poco grids. The threshold field was defined as the point where the field emission current rose above 1.0 μA. As can be seen, the 19-hole grids have lower threshold electric fields for both the conditioned and unconditioned states but the final breakdown fields are approximately equal. To establish a better relationship between the number of conditioning arcs and number of grid apertures, it is suggested that the same overall gridlet area (7.5 cm x 7.5 cm) be tested with different numbers of holes, including 1 and 37 (and even with no holes).

Also shown in Figure 3.58 are data taken on the 7-hole Poco graphite grids after undergoing the direct impingement erosion process. As was demonstrated with the CC gridlets, the eroded surface leads to a reduced initial threshold and breakdown field but upon the application of conditioning arcs, the eroded Poco surface is able to achieve the same maximum breakdown field as the BOL Poco gridlets.

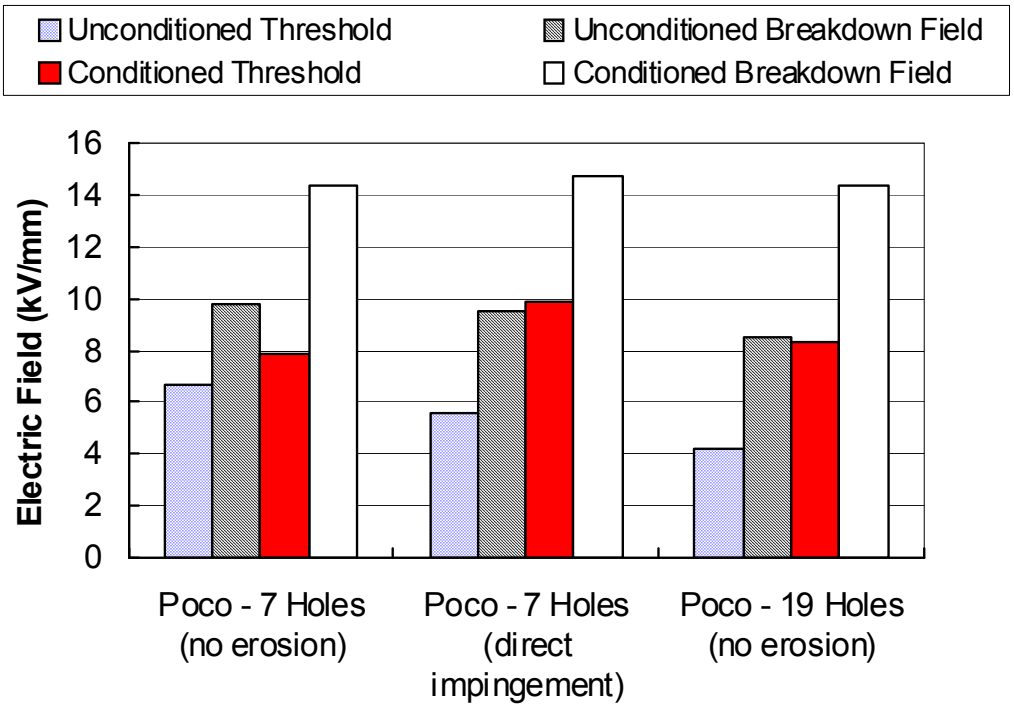

Figure 3.58 Threshold field comparison for field emission and continuous arcing for 7 and 19 hole Poco grids. Onset field emission = 0.001 mA.

4. CONCLUSION

A fundamental limit to increased perveance in ion thrusters is the maximum intra-grid electric field. This study has presented an investigation of the electric field breakdown characteristics of carbon-based and molybdenum ion optics in the total voltage range of 1 to 8 kV. The results show that with proper conditioning using small, controlled arcs, operation at electric fields up to 11 kV/mm for carbon-carbon, 9.5 kV/mm for pyrolytic graphite, 13.5 kV/mm for Poco graphite, and 15 kV/mm for molybdenum (all at a grid gap of 0.5 mm) can be achieved. Intra-grid arc conditioning at charge transfer values per arc of 0.25 and 1.0 mC allowed for larger voltage standoff capability presumably due to the removal of microscopic, field-emitting protrusions from the surface of the accelerator grid.

The act of extracting ions through apertures in the electrodes was not found to significantly affect the electric field breakdown behavior. Furthermore, in some tests when ions were extracted, the field enhancement factor measured from F-N plots decreased ~15% from a value measured without beam extraction. An interesting observation in all tests with carbon-based materials was field emission data would initially be very similar with and without beam extraction (within 5% if taken within 10 minutes of ion beam termination), however, the field emission would steadily drop as the xenon gas was pumped from the chamber (sometimes to values that are only 5% of the beam extraction field emission levels). A corresponding increase in the breakdown field of ~15% and a decrease in the field enhancement factor of ~30% were regularly recorded for pyrolytic graphite after the ion beam and xenon neutral flow had been off for several hours. This result indicated that the neutral xenon gas has an effect on field emission that

is not eliminated until the gas has completely been pumped out of the system and desorbed from the accelerator electrode surface. In contrast to the carbon-based materials, molybdenum showed the opposite effect (i.e., field emission decreased with the presence of xenon gas). In either the molybdenum and carbon-material cases, it is likely that xenon suppresses/enhances field emission by modifying the effective work function of the surfaces to higher/lower values.

The period between electrical breakdowns is random and Weibull statistical analysis was used to show that with an increasing amount of conditioning arcs, the mean time between arc events greatly increased at a given electric field condition. The Weibull shape parameter was found to be 0.7 - 0.8 for all of the carbon based materials and 0.9 for molybdenum, which suggested that burn-in and follow-on arcing processes are important for these materials.

A study of the effects of sputter erosion was also conducted to determine how the field emission and electric breakdown characteristics would change throughout life. Two grid sets were tested and eroded using two different accelerated-wear techniques. Each erosion process was conducted after full characterization tests were completed and after conditioning the grid surface with 1-mC conditioning arcs. The eroded surfaces returned to pre-conditioned performance levels, but could be re-conditioned relatively easily, where the breakdown field, field emission, and arc rate characteristics returned to their original pre-worn values. The electric field enhancement factor was observed to reach a steady state value after conditioning arcs were applied, and it is concluded that the saturation of the enhancement factor caused the electric field breakdown point to saturate. Although not confirmed during our short term tests, prolonged operation will probably

result in degradation of the electric field breakdown strength due to the upstream accelerator grid surface being sputtered and texturized by energetic ion bombardment. However, proper reconditioning of the grid surface can maintain a high operational level of electric field between the ion optics.

A method to predict the maximum applied breakdown field for a conditioned grid geometry and material was described and validated that uses estimates of the localized electric field at breakdown (gap independent) and the field enhancement factor (gap dependent). Calculations of the maximum applied electric field using this method were found to be 10-15% of measured values. Properly conditioned NEXIS gridlets fabricated from carbon-carbon materials are estimated to be capable of operation at fields up to 4.5 kV/mm at the NEXIS nominal spacing of 2.36 mm. By simply extrapolating breakdown field data (taken for grid gaps of 0.5 mm to 1.78 mm), a maximum electric field of 5 kV/mm is expected at the a spacing of 2.36 mm, which compares well with the calculated value. Finally, although spikes and anomalous excursions in the accelerator current were observed after aging the upstream side of the carbon-carbon grid, this behavior was eliminated upon initiating a few conditioning arcs.

5. SUGGESTIONS FOR FUTURE WORK

This thesis has developed an approach to suppress the growth of field emission between the grids of an ion thruster leading to significantly higher operational electric field capability for ion optics. However, there are several aspects of ion thruster operation that offer the opportunity to provide further insight into the implementation of this arc conditioning technique to full-scale thrusters. The phenomena of field emission should be further characterized for future implementation to larger-sized carbon-based grids. It is recommended that each of these topics be investigated as the development of ion thruster technology proceeds. These topics are:

1. Validation and utilization of the accelerated-wear testing technique presented in this study should be investigated further. This technique can be used as an alternative to long-term ground testing ion thrusters to investigate certain lifetime issues. This is especially important for high specific impulse thrusters like the NEXIS engine because backsputtering of facility material from the beam target can mask the wear of the ion optics system that would actually occur during a mission. One way of validating the accelerated erosion technique would be to conduct a relatively brief life test with gridlets. This could possibly entail operating the gridlets in a larger vacuum chamber for approximately 10,000 hours and comparing the erosion rates to the same induced erosion rates obtained from the accelerated wear testing facility.

2. Further characterization of pyrolytic graphite and molybdenum grid material is necessary and should be conducted. Although a preliminary evaluation of the electric

field breakdown characteristics of pyrolytic graphite and molybdenum was conducted for this thesis, time constraints did not allow these gridlets to be investigated as thoroughly as the carbon-carbon ion optics material. Considering that pyrolytic graphite is being considered for ambitious future ion propulsion missions and that molybdenum is already being used for state of the art ion thrusters, further testing of these materials (such as a study of their ability to re-condition after erosion of the surface) could reveal important new data.

3. Additional tests using the same methods discussed in this thesis on carbon-based gridlets with the same total area, but different numbers of holes should be performed. Although this was done for the Poco graphite material, the trends for carbon-based ion optics material should be investigated. Testing the field emission characteristics of carbon-based materials at BOL and after significant erosion of the surface for gridlets with different number of apertures could help develop a better understanding of how the electric field breakdown characteristics vary with the number of apertures.

4. It is suggested that an electric field breakdown characterization study be conducted on a full-scale ion thruster equipped with carbon-based ion optics. Using a state of the art ion thruster out-fitted with carbon-based ion optics of similar geometry as the gridlets tested in this thesis would provide conclusive evidence of how well the grid conditioning method used to achieve a significant increase in operating electric fields with gridlets could be translated to a full-scale thruster.

5. Evaluation of smaller screen grid holes is recommended. Due to the importance of operating at higher electric fields, and, in order to take full advantage of the increased current densities obtainable with smaller screen grid holes, a more detailed investigation of the electrical breakdown phenomenon is recommended where grid geometry is varied.

6. REFERENCES

[1] Jahn, R. G., *Physics of Electric Propulsion*, 1st ed., New York, McGraw-Hill, 1968.

[2] Stuhlinger, E., *Ion Propulsion for Space Flight*. New York: McGraw-Hall, 1964,

[3] Curran, F.M., Sovey, J.S., and Myers, R.M., "Electric propulsion: An evolutionary technology," IAF-91-241, 42nd Congress of the International Astronautical Federation, Montreal, CA, Oct. 5-11, 1991.

[4] Byers, D.C., "An experimental investigation of a high voltage electron-bombardment ion thruster," Journal of the Electrochemical Society, Vol. 116, No. 1, pp. 9-17, 1969.

[5] Jahn, R. G. and Choueiri, E. Y., "Electric propulsion," in Encyclopedia of Physical Science and Technology, Vol. 5, 3rd ed., Academic Press, 2002, pp. 125-141.

[6] Martinez-Sanchez, M. and Pollard, J. E., "Spacecraft electric propulsion - an overview," Journal of Propulsion and Power, Vol. 14, No. 5, pp. 688-693, 1998.

[7] Pollard, J. E., Jackson, D. E., Marvin, D. C., Jenkin, A. B., et al., "Electric propulsion flight experience and technology readiness," AIAA-93-2221, 1993.

[8] Sengupta, A., Brophy, J.R., Anderson, J.R., Garner, C., Groh, K. de., Karniotis, T., Bank, D., "An Overview of the Results from the 30,000 Hr Life Test of Deep Space 1 Flight Spare Engine," AIAA 2004-3608, 40th Joint Propulsion Conference, Fort Lauderdale, FL, July, 2004.

[9] Olsen, S., "Electric Propulsion Technology Development for the Jupiter Icy Moon Orbiter Project," AIAA-2004-3449, 40th Joint Propulsion Conference, Fort Lauderdale, FL, July, 2004.

[10] Randolph, T., Polk, J.E., "An Overview of the Nuclear Electric Xenon System (NEXIS) Activity," AIAA 2004-3450, 40th Joint Propulsion Conference, Fort Lauderdale, FL, July, 2004.

[11] Elliott, F.W., Foster, J.E., and Patterson, M.J., "An Overview of the High Power Electric Propulsion (HiPEP) Project," AIAA-2004-3453, 40th Joint Propulsion Conference, Fort Lauderdale, FL, July, 2004.

[12] Anderson, J.R., Polk, J.E., Brophy, J.R, "Service Life Assessment for Ion Engines," IEPC 97-049, 25th International Electric Propulsion Conference, Cleveland, OH 1997.

[13] Hedges, D.E., Meserole, J.S., "Demonstration and Evaluation of Carbon-Carbon Ion Optics," J. of Propulsion and Power, Vol. 10, No. 2, March-April 1994, pps. 255-261.

[14] Rawal, S.P., Perry, A.R., Williams, J.D., Wilbur, P.J., Laufer, D.M., Shih, W., Polaha, J., Hoskins, W.A., "Performance Evaluation of 8-cm Diameter Ion Optics Assemblies Fabricated from Carbon-Carbon Composites," AIAA-2004-3614, 40th Joint Propulsion Conference, Fort Lauderdale, FL, July 2004.

[15] Goebel, D.M., "High Voltage Breakdown Limits of Molybdenum and Carbon-based Grids for Ion Thrusters," AIAA 2005-4237, 41st Joint Propulsion Conference, Tucson, AZ, July, 2005.

[16] Hayakawa, Y., Kitamura, S., Miyazaki, K., "Endurance Test of C/C Grids for 14-cm Xenon Ion Thrusters," AIAA-2002-3958, 38th Joint Propulsion Conference, Indianapolis, IN, July 2002.

[17] G. Drummond, Colorado Power Electronics, SBIR Phase I program results, June 2004.

[18] Farnell, C.C., "Numerical Simulations of HiPEP Ion Optics," AIAA-2004-3818, 40th Joint Propulsion Conference, Fort Lauderdale, AL, 2004.

[19] Beatty, J.S., Snyder, J.S., Shih, W., "Manufacturing of 57-cm Carbon-Carbon Composite Ion Optics for a 20-kW-Class Ion Engine," AIAA-2005-4411, 41st Joint Propulsion Conference, Tucson, AZ, 2005.

[20] Aston, G., and Wilbur, P.J., "Ion Extraction from a Plasma," NASA CR-159849, June 1980.

[21] Brophy, J., Polk, J., Pless, L., "Test-to-Failure of a Two-Grid, 30-cm-dia. Ion Accelerator System," IEPC-93-172, 23rd International Electric Propulsion Conference, , Sept. 13-17, 1993, Seattle, Washington.

[22] Wilbur, P.J., Beattie, J.R., Hyman, J., "Approach to the Parametric Design of Ion Thruster," J. Propulsion, Vol. 6, No. 5, pp. 575-583, Sept-Oct 1990.

[23] Kaufman, H.R., "Technology of Electron-Bombardment Ion Thrusters," *Advances in Electronics and Electron Physics*, Vol. 36, 1974.

[24] Williams, J.D., Goebel, D.M., and Wilbur, P.J., "Analytical Model of Electron Backstreaming in Ion Thrusters," AIAA-2003-4560, 39th Joint Propulsion Conference, Huntsville, AL, 2003.

[25] Farnell, C.C., Williams, J.D., and Wilbur, P.J., "Numerical Simulation of Ion Thruster Optics," 28th International Electric Propulsion Conference, IEPC-03-073, Toulouse, France, 2003.

[26] Martinez, R.A., Buttweiler, M.S., Williams, J.D., Drummond, G., "Evaluation of Sub-Scale NEXIS Ion Optics and Strategies for Performing Accelerated Wear Testing," AIAA-2004-3628, 40th Joint Propulsion Conference, Fort Lauderdale, AL, 2004.

[27] Williams, J.D., Johnson, M.L., and Williams, D.D., "Differential Sputtering Behavior of Pyrolytic Graphite and Carbon-Carbon Composite Under Xenon Bombardment," AIAA-2004-7788, 40th Joint Propulsion Conference, Fort Lauderdale, AL, 2004.

[28] Goebel, D.M., Jet Propulsion Laboratory, Private Communication, June 2004.

[29] Polk, J.E., Duchemin, O.B., Ho, C., Koel, B.E., "The Effect of Carbon Deposition on Accelerator Grid Wear Rates in Ion Engine Ground Testing," AIAA-2000-3662, 36th Joint Propulsion Conference, Huntsville, AL, 2000.

[30] Van Noord, J.L., Soulas, G.C., "A Facility and Ion Thruster Back Sputter Survey for Higher Power Ion Thrusters," AIAA-2005-4067, 41st Joint Propulsion Conference, Tucson, AZ, 2005.

[31] Barker, T.R., "Impingement-current-erosion characteristics of accelerator grids on two-grid ion thrusters," M.S. Thesis, Mechanical Engineering Dept., Colorado State University, Fort Collins, CO, 1996.

[32] Martynoy, E.P., Sov. Phys. – Tech. Phys. Vol. 16, pp. 1364-9, 1972.

[33] Cox, B.M., "The Nature of Field Emission Sites," J. Phys. D: Appl. Phys. Vol. 8, 1975.

[34] Loyd, O., Proc. 6th Int. Symp. On Discharges and Elect. Ins. In Vacuum, pp. 230-55, 1974.

[35] Fowler, R.H., Nordheim, L., "Electron Emission in Intense Electric Fields," Proceedings of the Royal Society (London), 119:173-181, 1928.

[36] Alpert, D., Lee., D.A., Lyman, E.M., Tomaschke, H.E., "Initiation of Electrical Breakdown in Ultrahigh Vacuum," Journal of Vacuum Science and Technology, Volume 1, pages 35-50, 1964.

[37] Latham, R.V., *High Voltage Vacuum Insulation*, Academic Press, Harcourt Brace & Company Publishers, 1995, pp. 122-127

[38] Little, R.P. and Whitney, W.T., "Electron Emission Proceeding Electrical Breakdown in Vacuum," Journal of Applied Physics, Vol. 34, No. 3, August, 1963.

[39] Boxman, R.L., *Handbook of Vacuum Arc Science and Technology*, Noyes Publications, 1995.

[40] Weibull, W., "A Statistical Theory of the Strength of Materials," Ingeniors Vetanskaps Akademien-Handlinger, no. 151, 1939.

[41] Weibull, W., "A Statistical Distribution Function of Wide Applicability," Trans. ASME, Journal of Applied Mechanics, Volume 18, no. 3, pp. 293-297, 1951.

[42] Abernethy, R.B., *The New Weibull Handbook*, Fourth Edition, North Palm Beach, FL: Robert B. Abernethy.

[43] Wadsworth, H.M., *Handbook of Statistical Methods for Engineers and Scientists*," McGraw-Hill Publishing Company, 1990.

[44] Steib, G.F., and Moll, E., "High-voltage conditioning at large gaps in industrial vacuum," J. Phys. D: Appl. Phys., 6, 243-255, 1973.

[45] Llyod, O., Gozna, C.F., and Jervis-Hunter, G., "The initiation of arcs by ion bombardment," J. Phys. D: Appl. Phys., Vol. 3, 1970.

[46] Allen, R.J., Field Emission and Breakdown Processes in Vacuum Gaps with SiOx Coated Cathodes, Ph.D. Thesis, Old Dominion University, May, 1998

[47] Gruszka, H., and Moscicka-Grzesiak, "Conditioning process of electropolished electrodes by field emission current in vacuum," 11th IN. Symp. On Discharges and Electr. Insul. In Vacuum, Berlin, GDR, Sept. 24-8, 1984 pp. 33-36.

[48] Hackman, R., and Salman, S.K., Proc. IEEE 119 (3), p. 1947 (1972).

[49] Bloomer, R.N., and Cox, B.M., "Some effects of gases upon vacuum breakdown initiated by field emission electrons," Vacuum, V. 18, No. 7, pp. 379-382, 1968.

[50] Hackman, R., and Govinda Raju, G.P., "Electrical breakdown of a point-plane gap in high vacuum and with variation of pressure in the range 10-7-10-2 Torr of air, nitrogen, helium, sulphur hexafluoride, and argon," J. Appl. Phys. 45, 4784-94 (1974)

[51] Danloy, L., and Simon, P., "High Voltage Behavior of Electrostatic Separators at CERN in the Presence of Organic Vapors," Proc. V-ISDEIV, 367-372, 1972.

[52] Cook, C.M, "Residual Pressure and It's Effect on Vacuum Insulation," Proceedings of the Second International Symposium on Insulation of High Voltages in Vacuum, Cambridge Mass, Sept. 1966, p. 181.

[53] Collazo, R., Schlesser, R., Sitar, Z., Appl. Phys. Lett. 78, 2058 (2001).

[54] Pivovar, L.I., and Gordienko, V.I., Soviet Phys.-Tech. Phys. Vol. 7, 908 (1963).

[55] Tomaschke, H.E., "A Study of the Projections on Electrodes and Their Effect on Electrical Breakdown in Vacuum," University of Illinois, Ph.D., 1964.

[56] Boersch, H., Hamisch, H., Ehrlich, W., "Surface Discharge Over Insulators Under Vacuum," Zangew Phys. 15, pp. 518-525, 1963 (Transl. NASA-TM-77936, NTIS.

[57] Johnson, R.P., "A Study of Electrical Breakdown Between Plan-Parallel Molybdenum Electrodes In High Vacuum," M.S. Thesis, North Dakota State University, May, 1980.

[58] Cox, B.M., and Williams, W.T., Proc. 7th Int. Symp. On Discharges and Electrical Insulation n vacuum, Novosibirs 1976, p.176.

[59] Little, R.P, Smith, S.T., "Electrical Breakdown in Vacuum," IEEE Transactions on Electron Devices, Vol. 12, pp. 77-83, 1965.

[60] Kohl, W.H., *Handbook of Materials and Techniques for Vacuum Devices*. New York: Reinhold, 1967.

[61] Staprans, A., "Voltage breakdown limitations of electron guns," in Proc. 2nd Int. Symp. Insul. High Voltages Vacuum, Sep. 1966, pp. 293-303.

[62] Hackam, R., Salman, S.K., "Effects of electrode curvature, distance from glass insulator, and addition of hydrogen on field-emission currents and breakdown voltage in vacuum," *Journal of Applied Physics*, Volume 45, Number 10, October 1974.

[63] Byers, D.C., "An Experimental Investigation of a High-Voltage, Electron-Bombardment Ion Thruster," *J. Electrochem. Soc.: Electrochemical Science*, Volume 16, Number 1, January 1969.

[64] Rogowski, W., Archiv fur Elektrotechnik, 12, 1-15, 1923.

[65] Snyder, J., "Review of Carbon-based Grid Development Activities for Ion Thrusters", AIAA 2003-4715, 39th Joint Propulsion Conference, Huntsville, AL, July 20-23, 2003.

[66] Bonard, J.M., et al., "Field emission from single-wall carbon nanotube films,"Applied Physics Letters, Volume 73, Number 7, pp. 918-920, August 17, 1998.

[67] Williams, D.W., Williams, W.T., "Effect of electrode surface finish on electrical breakdown in vacuum," *Applied Physics*, Volume 5, 1972.

[68] Snyder, J.S., et. al., "Results of a 2000-Hour Wear Test of the NEXIS Ion Engine," In 29th International Electric Propulsion Conference, Princeton, NJ, 2005. IEPC-2005-281,

[69] Mesyats, G.A., Proskurovsky, D.I., *Pulsed Electrical Discharge in Vacuum*, Springer-Verlag Berlin Heidelberg, pp. 25, 1989.

[70] Meek, J.M., Craggs, J.D., *Electrical Breakdown of Gases*, Oxford University Press, Amen House, London, pp. 120, 1953.

[71] Okawa, M., Shioiri, T., Okubo, H., Yanabu, S., "Area Effect on Electric Breakdown of Copper and Stainless Steel Electrodes in Vacuum," *IEEE Transactions on Electrical Insulation*, Volume 23, Number 1.

[72] Kerslake, W.R., Goldman, R.G., Nieberding, W.C., J. Spacecraft and Rockets 8, 213-224 (1971).

[73] Nakanishi, T., et al., "An Electrode with Molybdenum-Cathode and Titanium-Anode to Minimize Field Emission Dark Currents," in Proceedings of LINAC, 2004, Lubeck, Germany.

[74] T. Lin, "Prebreakdown and breakdown phenomena between molybdenum electrodes in the presence of thermionic cathodes," M.S. thesis, Dept. of Physics, North Dakota State University, Fargo, North Dakota, 1984.

[75] Snyder, J.S., Brophy, J.R., Goebel, D.M., Beatty, J.S., "Development and Testing of Carbon-based Ion Optics for 30-cm Ion Thrusters," AIAA-2003-4716, 39th Joint Propulsion Conference, Huntsville, AL 2003.

7. APPENDIX: WEIBULL ANALYSIS DATA

Introduction

Weibull analysis is a method for obtaining probability distributions of a stochastic process or measurement. It is often used in studies aimed at determination of the statistics of product or component failure times because it provides the most accurate estimate of most physical phenomenon with a minimum number of measurements. Weibull analysis can be used to make predictions about a product's life, compare the reliability of competing product designs, statistically establish warranty policies, or proactively manage spare parts inventories. In academia, Weibull analysis has been used to model such diverse phenomena as the length of labor strikes, AIDS mortality, and earthquake probabilities. Although most Weibull analysis is aimed at determining the statistical distribution of events in time, it can also be used for characterizing the uncertainty of any measurable quantity. The application of Weibull analysis only requires that the data contain values greater than zero.

In the case of ion propulsion, Weibull analysis can be used to determine the mean period between arcs that occur in ion optics systems as a function of operating condition, electrode surface condition, and geometrical configuration. More important to providing statistically correct estimations of the mean arc period, Weibull analysis can also be used to determine parameters that describe the probability distribution function of arc period, which is useful for system analysts and power system designers. Finally, Weibull plots are very useful for graphically demonstrating if one grid surface is better than another in terms of mean arc period or if a grid surface is degrading due to sputter or arc erosion processes.

Sample Case

An example of a typical arcing data set will be used to illustrate Weibull analysis techniques using routines available in Microsoft Excel. Column A in Table A1 shows the time that arcs have occurred since the start of a test (e.g., cell A3 indicates that an arc occurred 2534 seconds after the ion source was turned on, which was 141 seconds after the first arc was observed at 2393 seconds).

Table A1: Sample arcing data for NEXIS CC gridlets at 0.5 mm spacing and 7.8 kV/mm.

	A	B	C	D	E		G	H
1	Raw Data (s)	Delta Time	Ascending Order	Rank	Median Rank		ln(ln(1/(1-Median Rank))) y-axis	ln(Time Btw Arcs) x-axis
2	2393	-	-	-	-		-	-
3	2534	141	141	1	0.1296		-1.974	4.949
4	5385	2851	470	2	0.3148		-0.9727	6.153
5	5855	470	1135	3	0.5000		-0.3665	7.034
6	8540	2685	2685	4	0.6852		0.1448	7.895
7	9675	1135	2851	5	0.8704		0.7145	7.955

Data Preparation

Modeling the arc period data using Weibull analysis requires some preparation in order to apply regression analysis techniques. The following procedure can be used to prepare the data:

a. Determine the time between successive arcs and place in Column B. Then place the times between arcs in ascending order in Column C.

b. Place sequential numbers in Column D starting with 1 and going until all arc events have been numbered (N = total number of arcs, which is 5 for the data contained in Table A1, and i = a particular arc event of interest).

c. Calculate the median rank of the arc events and place in Column E (median rank $\approx$ (i - 0.3)/(N + 0.4)).

d. Calculate ln(ln[1/(1-median rank)]) and place in Column G.

e. Calculate the ln(time between arcs) and place in Column H.

Fitting a line to the data

By performing a simple linear regression, one can obtain parameter estimates that will enable the statistical characterization of the arc period. First, be sure that the Analysis ToolPak Add-In is loaded into Excel. From the menu bar, select Tools … Add-Ins. Click on the checkbox for Analysis ToolPak, and then click OK.

To perform a linear regression:

a. Set the active worksheet to one with the y-axis and x-axis data organized like the example shown in Table A1. Go to the menu bar, select Tools and Data Analysis. Scroll down and highlight "Regression" and click OK. A data-entry window will pop up.

b. Under "Input Y Range," type: $G$2:$G$7 (for the data shown in Table A1).

c. For "Input X Range," type: $H$2:$H$7.

d. Click to add a checkmark for "Labels."

e. For "Output Options," select "New Worksheet Ply."

f. Click to add a checkmark for "Line Fit Plots."

g. Click OK and Excel will perform the regression analysis and place the output in a new worksheet.

Reformatting the output

On the new Excel sheet just created, the columns do not automatically adjust to their optimal widths. To do this, within the worksheet, click on column heading "A" and

drag to column heading "I." Now double-click on the boundary to the right of any column heading. The table should look similar to Table A2.

Table A2: Results of linear regression routine.

	A	B	C	D	E	F	G
1	**SUMMARY OUTPUT**						
2							
3	*Regression Statistics*						
4	Multiple R	0.98336594					
5	R Square	0.96700857					
6	Adjusted R Square	0.95601143					
7	Standard Error	0.21759617					
8	Observations	5					
9							
10	ANOVA						
11		*df*	*SS*	*MS*	*F*	*Significance F*	
12	Regression	1	4.163447032	4.1634470	87.9327254	0.002568884	
13	Residual	3	0.142044285	0.0473480			
14	Total	4	4.305491317				
15							
16		*Coefficients*	*Standard Error*	*t Stat*	*P-value*	*Lower 95%*	*Upper 95%*
17	Intercept	-5.9580274	0.591087397	-10.079774	0.00207941	-7.839133142	-4.07692181
18	ln(Time Btw Arcs)	0.80430489	0.085771981	9.3772450	0.00256888	0.53133991	1.07726987
19	***Beta (or Shape Parameter) =***	**0.80**					
20	***Alpha (or Characteristic Life) =***	**1648.59**					

Now scroll to the right and locate the graph that was automatically generated by the regression analysis routine. Reformat the graph according to your preferences. It is best to use a solid line and no point markers for the "Predicted Line" and delete the legend to remove clutter. See the example plot shown in Fig. A1.

In cell A19, type the label: "Beta (or Shape Parameter)=." In cell B19, type the formula: "= B18." In cell A20, type the label: "Alpha (or Characteristic Life)=." In cell

B20, type the formula: "=EXP(-B17/B18)." For the arc period data contained in Table A1, $\beta = 0.80$ and $\alpha = 1649$ seconds.

Interpreting the results

In traditional use, the Weibull shape parameter, called β, indicates whether a failure rate is increasing ($\beta > 1$), constant ($\beta = 1$), or decreasing ($\beta < 1$). The scenario when $\beta < 1$ is typical of "infant mortality" and in our specific case of grid characterization might indicate that the grids are arcing more frequently during their "burn-in" period or that once an arc occurs, it is followed by a series of arcs in relatively short times (similar to after shocks in earthquake phenomenon). For $\beta = 1$, the likelihood of an event is equally probably for all time and a good example of this type of behavior in traditional Weibull analysis is radioactive decay processes. At $\beta > 1.0$, an increasing event probability occurs at a particular time. This is typical of products that are designed to wear out after a given amount of use. The β for the arcing data in Table A1 was 0.80 indicating that more of the arcing is occurring early during grid operation or in an after shock mode where one arc causes a series of follow-on arcs.

The Weibull characteristic life, called α (sometimes η is used also), is a measure of the time scale of the distribution of data. It so happens that α corresponds to the time where 63.2% of the arcs in a given population will have occurred. For the data in Table A1, the characteristic life is 1649 seconds and the average arc frequency would be 0.6 mHz. The gridlets only contain seven apertures, and, if everything were assumed to scale with active grid area, a full-scale NEXIS thruster would be expected to arc every 2.8 seconds at the spacing and high electric field conditions corresponding to the data in Table A1. A more realistic assumption might be that arcing periods will scale with total

electrode area. The total area of a 3"x3" accelerator gridlet is 58 cm^2, and, if total electrode area ratios are assumed to be most important, then one would expect that full-scale NEXIS optics would arc every 30 seconds (at the spacing and high electric field conditions corresponding to the data in Table A1).

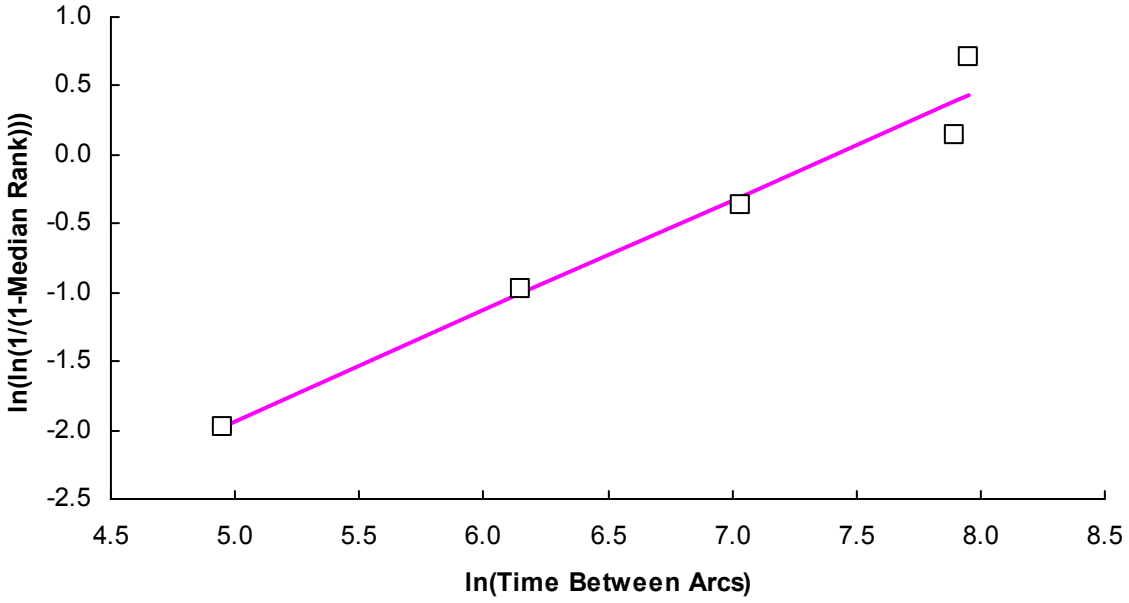

Fig. A1 Regression plot generated by Excel of Weibull data contained in Tables A1 and A2.